Imaging amyloid fibers at the nanoscale: method development and applications for hybrid materials and biomedicine

Tesis presentada por**: Patricia Bondia Raga**

para optar al título de Doctor en Física de la Materia Condensada, Nanotecnología y Biofísica

Madrid, septiembre 2019

Facultad de Ciencias

Departamento de Física de la Materia Condensada

Universidad Autónoma de Madrid

Directora de tesis: **Dra. Cristina Flors**

Tutor de tesis: **Dr. Raúl Guantes**

Publications

The publications resulted from the development of this thesis are the following ones:

1. **Bondia, P.**, Torra, J., Tone, C., Sawazai, T., del Valle, A., Sot, B., Nonell, S., Kanai, M., Sohma, Y. and Flors, C. A nanoscale view of amyloid photodynamic damage (in preparation).

2. **Bondia P.**, Casado S., Flors C. (2017) Correlative super-resolution fluorescence imaging and atomic force microscopy for the characterization of biological samples. *In: Erfle H. (eds) Super-Resolution Microscopy. Methods in Molecular Biology,* vol 1663, p 105-113. Humana Press, New York, NY.

3. **Bondia, P.**, Jurado, R., Casado, S., Domínguez-Vera, J. M., Gálvez, N., & Flors, C. (2017). Hybrid nanoscopy of hybrid nanomaterials. *Small*, *13*(17), 1603784.

4. Jurado, R., Castello, F., **Bondia, P.**, Casado, S., Flors, C., Cuesta, R., Domínguez-Vera, J.M., Orte, A. and Gálvez, N. (2016). Apoferritin fibers: a new template for 1D fluorescent hybrid nanostructures. *Nanoscale*, 8(18), pp.9648-9656.

Other publications not included in the thesis:

5. Gonzalez-Carrero, S., Bareño, L., Debroye, E., Martin, C., **Bondia, P.**, Flors, C., Galian, R. E., Hofkens, J. & Pérez-Prieto, J. (2019). Linear assembly of lead bromide-based nanoparticles inside lead (ii) polymers prepared by mixing the precursors of both the nanoparticle and the polymer. *Chemical Communications,* 55(20), 2968-2971.

6. Mertens, J., **Bondia, P.**, Allende-Ballestero, C., Carrascosa, J. L., Flors, C., & Castón, J. R. (2018). Mechanics of virus-like particles labeled with green fluorescent protein. *Biophysical Journal*, 115(8), 1561-1568.

Acknowledgements

Son muchas las personas que han contribuido de una u otra manera al desarrollo de esta tesis, no solo en lo que se muestra en este manuscrito sino también en otros proyectos paralelos que han formado parte de mi desarrollo científico, o aquellas que fuera del ámbito científico me han dado su apoyo para llevarla a cabo. Por ello, me gustaría dedicar unas líneas de agradecimiento a todas estas personas.

En primer lugar, me gustaría agradecer a mi directora la Dra. Cristina Flors, por darme la oportunidad de realizar la tesis y ayudarme a crecer personal y profesionalmente. Gracias por tu confianza y tu apoyo, por estar siempre pendiente de todo y tener planes B y C. Y también por motivarme para superarme constantemente, tanto científicamente como en cualquier otra materia, ya sea hablar en público, comunicarme en inglés o incluso apoyar mis inquietudes artísticas.

Quiero agradecer también al Ministerio de Economía y Competitividad por financiar mi trabajo con la beca FPI BES-2016-076293 dentro del proyecto MAT2015-66605-P y al Ministerio de Ciencia, Innovación y Universidades por financiar el proyecto PCI2018-093064.

Por otra parte, también quiero agradecer a mi tutor de la Universidad Autónoma, el Dr. Raúl Guantes, por su disposición en todo momento, así como su ayuda con todos los trámites implicados en la realización de la tesis.

Y a todos los que forman. A Adrián del Valle, por ser mi primer compañero y enseñarme los trucos de trabajar día a día con el AFM; y por su cariño, siempre dispuesto a ayudarme, a levantarme el ánimo o a traerme manolitos. Al Dr. Joaquim Torra por su ayuda para la interpretación de espectros de cualquier tipo, fluorescencia, absorbancia, MALDI y por enseñarme a usar el CD, pero sobre todo por aligerar los días más duros con sus historias, bromas y canciones. A la Dra. Caterina Tone por ser mi compañera durante el tramo final de la tesis, trabajando conmigo en las medidas y discusión para que los resultados del capítulo 6 cobraran sentido. Al Dr. Alberto Pulido, por su ayuda con las cápsidas y con la microscopia de expansión, por estar a mil cosas, pero siempre sacar tiempo para mí y por su alegría contagiosa. A nuestro último fichaje, Ingrid Ortega por estar siempre dispuesta a escuchar mis historias de la tesis y por su amabilidad. Al

Dr. Santiago Casado por su implicación en la obtención e interpretación de medidas de AFM de los experimentos de los capítulos 3 y 4. A la Dra. Patricia Pedraz ser mi apoyo tanto dentro como fuera de IMDEA, ya esté en Madrid, Estocolmo o Australia, y por instaurar el orden en el laboratorio.

Moreover, I would like to acknowledge Prof. Kanai, Dr. Sohma and its group (University of Tokyo, Japan) for giving me the opportunity of spending a short stay in their laboratory during my PhD and their kind attention during my period in Tokyo. I would like specially to thank Dr. Sohma for all the time he spent teaching me the secrets of the synthesis of some of the peptides used in chapter 5, its help in the interpretation of MALDI-TOF spectra and for providing us the photocatalyst used in experiments of chapter 6.

Y me gustaría expresar mi agradecimiento a la Dra. Begoña Sot por enseñarme a producir y fibrilar la sinucleína y proporcionarme los mutantes derivados de la misma que se utilizan en el capítulo 5 de la tesis. Además de por su amabilidad y su ayuda durante estos años.

También quiero agradecer al grupo de la Dra. Natividad Gálvez (Universidad de Granada), por proporcionarnos las muestras utilizadas en los capítulos 3 y 4.

Por otra parte, me gustaría agradecer al Dr. Jose Castón y su grupo (Centro Nacional de Biotecnología ((CNB), España) por acogerme en su laboratorio y formar parte de mi aprendizaje científico durante el doctorado, aunque finalmente mi tesis tuviera que cambiar de rumbo. En especial me gustaría agradecer a Carolina Allende por enseñarme a producir cápsidas virales y a usar TEM, pero sobre todo por hacerme sentir tan a gusto trabajando a su lado. Y también al Dr. Johan Mertens, por enseñarme el funcionamiento del AFM en el modo de espectroscopía de fuerzas para romper estas cápsidas y por su simpatía siempre que nos encontramos por IMDEA.

Asimismo, me gustaría agradecer al servicio de proteómica y microscopia electrónica del CNB, por realizar los espectros de MALDI-TOF y las imágenes de TEM.

Me gustaría dar las gracias a IMDEA nanociencia por darme la oportunidad de hacer mi doctorado en un centro tan interdisciplinar donde se nos da la oportunidad de entender la ciencia desde distintos puntos de vista y trabajar en un ambiente en el que

la gente disfruta con lo que hace convirtiendo esta pasión en algo contagioso. Y a todas las personas que han participado de una forma u otra del progreso de esta tesis como: la Dra. Adriana Arnáiz por enseñarme todo lo necesario para realizar cultivos celulares, la Dra. Milagros Castellanos, al Dr. Andrés Valera, Sergio de las Heras, Warren Smith, Fabiola Mogollon, Roberto o el grupo administrativo… por ser solucionadores de problemas y hacer la vida más sencilla a todos los que trabajamos en IMDEA.

Y especialmente, quiero agradecer a toda la gente que se han convertido en amigos más que en compañeros de trabajo, haciendo que las comidas y cafés sean momentos de recargar pilas a base de risas y endorfinas: Lucía (mi poeta favorita), Alejandra (mi mala influencia), Mary Tere (KPS), Víctor (sin victorado), Manu, Maite, Ivan, Andrea, Marina, Marzoa, Gudin, Miguel, Sergio (el nuevo Maite) y Sergio (barbas). Y los que siguieron su camino, aunque los tengo muy presentes: Jenny, Fer, Sara (y los Fridays Cake's), Fran, Felipe, Irene y Paula.

Y a esa gente que es mi apoyo en la distancia, Isabel por ser mi confidente, por sus consejos y simplemente por estar siempre ahí, a Cristina por acogerme desde mi primer día en Holanda y ahora ser mi promotora científico-artista y *of course Adrian for waking up my interest in biophysics and being my personal coach for science and life. Hope we 4 share lots of sunsets!*

Y por supuesto, quiero dar las gracias a David, por hacer que todo sea siempre tan fácil, por entenderme, ayudarme y sacarme siempre una sonrisa, haciendo que cada día sea especial.

Finalmente, quiero dar las gracias a las personas más importantes de mi vida, mi familia, que me han apoyado siempre en mi decisión de empezar una carrera investigadora esforzándose por entender a que me dedico. A mis padres que viven conmigo cada aventura, muchas veces literalmente, y siempre me han enseñado a buscar la felicidad. Y a mi hermana Ami, por demostrarme con su ejemplo que cada uno podemos ser y hacer lo que queramos, que no hay camino establecido. Y por supuesto a nuestras nuevas jefas, Lucia y Alegría, por llenaros los días de ilusión y enseñarnos lo que es la valentía desde el primer día que aparecieron en nuestras vidas.

GRACIAS POR TODO

Contents

List of acronyms

ACN	Acetonitrile
AFM	Atomic Force Microscopy
APP	Amyloid Precursor Protein
APTES	3-aminopropyltriethoxysilane
Aβ	β-amyloid
BLG	β-lactoglobulin
CLEM	Correlative Light and Electron Microscopy
DHAP	2',4',-Dihydroxyacetophenone
DIC	N,N'-diisopropylcarbodiimide
DMF	dimethylformamide
dSTORM	direct Stochastic Optical Reconstruction Microscopy
EDXS	Energy Dispersive X-ray Spectroscopy
eGFP	enhanced Green Fluorescence Protein
EM	Electron Microscopy
FFT	Fast Fourier Transform
Fmoc	Fluorenylmethyloxycarbonyl
FTIR	Fourier Transform Infrared
HATU	(1-[Bis(dimethylamino)methylene]-1H-1,2,3-triazolo[4,5-b]pyridinium 3-oxid hexafluorophosphate, Hexafluorophosphate Azabenzotriazole Tetramethyl Uronium)
HOAt	1-Hydroxy-7-azabenzotriazole
HOBt	1-hydroxybenzotriazole
HPLC	High Performance Liquid Chromatography
IDP	Intrinsically Disordered Proteins
MALDI-TOF	Matrix-assisted Laser Desorption/ionization Time-Of-Flight
MS	Mass Spectrometry
NA	Numerical Aperture
NMR	Nuclear Magnetic Resonance
NSOM	Near-field Scanning Optical Microscopy
PALM	Photoactivated Localization Microscopy
PBS	Phosphate-buffered saline
PEG	Polyethyleneglycol
PSF	Point Spread Function
ROS	Reactive Oxygen Species
SIM	Structured-Illumination Microscopy
SIMS	Secondary Ion Mass Spectrometry
SMLM	Single Molecule Localization Microscopy
SO	Sulfoxide
SPA	Sinapic acid
SPPS	Solid Phase Peptide Synthesis

STED	Stimulated Emission Depletion Microscopy
STORM	Stochastic Optical Reconstruction Microscopy
TERS	Tip-Enhanced Raman Spectroscopy
TFA	Trifluoroacetic acid
ThT	Thioflavin T
TrtA	Tritylcarboxamidomethyl
α-syn	α-synuclein

List of figures

Abstract

In the last decades, advanced imaging techniques have improved our ability to analyze biological systems at the nanoscale, enabling the observation of structural and molecular components. Different imaging tools are specialized in the characterization of a specific aspect of the sample and, when they are combined, complementary information is obtained providing a more comprehensive understanding of the system. This thesis focuses on the application of (super-resolution) fluorescence microscopy in combination with atomic force microscopy (AFM) for revealing specific chemical information in a high-resolution topography map. Particularly, correlative microscopy is applied to the characterization of amyloid fibers, which are misfolded protein aggregates with interest in nanomaterials research and biomedicine. This manuscript is organized in seven chapters. Chapter 1 introduces the imaging techniques used in the thesis. It also gives a general overview on amyloid fibers, their application as hybrid materials, their importance in biomedicine for being involved in different diseases, and the phototherapeutic approaches available to treat them. In Chapter 2, the general materials and methods used during the thesis are explained. Chapter 3 provides a detailed discussion about technical aspects of correlative super-resolution fluorescence microscopy and AFM such as sample preparation, data analysis and image alignment. Furthermore, the advantage of using AFM as a "ground truth" to evaluate different aspects of super-resolution techniques, such as labeling or image reconstruction, is highlighted. In Chapter 4, the methodology developed in Chapter 3 is applied to evaluate the functionalization of amyloid fibers with quantum dots or organic fluorophores. Thus, correlative microscopy is presented as a useful technique for characterizing luminescent hybrid materials at the nanoscale.

In the context of biomedicine, amyloid aggregates are important for being involved in different diseases (e.g. Alzheimer or Parkinson). Photochemical strategies to degrade amyloid structures are becoming an interesting alternative. In this thesis, a thioflavin T (ThT) derivative (ROS-ThT), which is able to target pathogenic aggregates in the presence of functional proteins, is used to study photodamage effects on amyloid fibers. In addition to fluorescence, this photocatalyst or photosensitizer produces singlet oxygen

upon blue light exposure, affecting amyloid structures through oxidation. The purpose of Chapter 5 is to select a useful amyloid model to evaluate photodamage at the nanoscale, and therefore different fibers were produced, fibrillated and characterized. In Chapter 6, the selected amyloid model is used to study photodamage induced by ROS-ThT at the single-fiber level through imaging techniques, and complemented by classical biochemical assays. These experiments highlight that the combination of fluorescence microscopy and AFM is useful to probe the heterogeneity of amyloid material and to disentangle the complex dependence between photocatalyst binding/activity and fiber morphology and/or composition. The aim of Chapter 7 is to provide coherence and perspective to the main results of the thesis, as well as an outlook on how advanced microscopy methods may impact the study of amyloids in different fields of research.

Resumen

En las últimas décadas, las técnicas de imagen avanzada han mejorado nuestra capacidad de analizar sistemas biológicos a la nanoescala permitiéndonos observar sus componentes estructurales y moleculares. Estas técnicas están especializadas en la caracterización de un aspecto específico de la muestra y, cuando se combinan, se obtiene información complementaria, lo que proporciona una comprensión más completa del sistema. Esta tesis se centra en la aplicación de la microscopía de fluorescencia de súper resolución en combinación con la microscopía de fuerza atómica (AFM) para mostrar información química específica de la muestra sobre su mapa topográfico de alta resolución. En particular, la microscopía correlativa se aplica a la caracterización de las fibras amiloides, que son agregados de proteínas con interés en la investigación de nanomateriales y biomedicina. Este manuscrito está organizado en siete capítulos. El Capítulo 1 presenta las técnicas de imagen utilizadas en la tesis. También ofrece una visión general de las fibras amiloides, su aplicación como materiales híbridos, su importancia en la biomedicina por estar asociadas a diferentes enfermedades y las estrategias fototerapéuticas disponibles para tratarlas. En el Capítulo 2, se explican los materiales y métodos generales utilizados durante la tesis. El Capítulo 3 proporciona una discusión detallada sobre los aspectos técnicos de la microscopía correlativa de AFM y de fluorescencia de súper resolución, como la preparación de muestras, análisis de datos y alineación de imágenes. Además, se destaca la ventaja de utilizar las imágenes de AFM como referencia para analizar diferentes aspectos de las técnicas de súper-resolución, como el marcaje o la reconstrucción de imágenes. En el Capítulo 4, la metodología desarrollada en el Capítulo 3 se aplica para evaluar la funcionalización de las fibras amiloides con puntos cuánticos o fluoróforos orgánicos. De esta manera, se presenta la microscopía correlativa como una técnica de gran utilidad para caracterizar materiales híbridos luminiscentes a la nanoescala.

En el contexto de la biomedicina, los agregados amiloides son importantes por estar implicados en el desarrollo de diferentes enfermedades (por ejemplo, Alzheimer o Parkinson). La utilización de estrategias fotoquímicas para degradar las estructuras

amiloides se están convirtiendo en una alternativa prometedora. Para esta tesis, se usó un derivado de tioflavina T (ThT) denominado ROS-ThT, que es capaz de degradar los agregados tóxicos en presencia de proteínas funcionales, para estudiar los efectos del daño fotoquímico producido en las fibras amiloides. Además de la fluorescencia, este fotocatalizador o fotosensibilizador produce oxígeno singlete tras la exposición a la luz azul, lo que provoca la oxidación de las estructuras amiloides. El propósito del capítulo 5 es seleccionar un modelo amiloide útil para evaluar el daño fotoquímico producido por el fotocatalizador a la nanoescala. Para ello, se produjeron, fibrilaron y caracterizaron diferentes fibras. En el capítulo 6, el modelo amiloide seleccionado se usa para estudiar el daño fotoquímico inducido por ROS-ThT a través de su caracterización a nivel de fibra individual con técnicas de imagen, y es complementado por ensayos bioquímicos clásicos. En estos experimentos, la combinación de AFM y microscopía de fluorescencia es útil para analizar la heterogeneidad del material amiloide y estudiar la dependencia de la unión / actividad del fotocatalizador y la morfología y / o composición de la fibra. El objetivo del capítulo 7 es proporcionar coherencia y perspectiva a los principales resultados de la tesis, así como una reflexión sobre cómo los métodos de microscopía avanzada pueden contribuir al estudio de los agregados amiloides en diferentes campos de investigación.

Preface

A significant part of our brain is dedicated to visual processing. Our eyes are detectors that have been evolving during millions of years to sense the world that surrounds us, and our brain has been perfectioned to process and interpret the arriving images in order to understand it [1, 2]. Our eye's resolution limit is ~40 microns (around the diameter of a hair) and was the limit of visual exploration during a long period of time. It was not until 17th century that Robert Hook and Anton van Leeuwenhoek discovered through their microscopes a microscale living world of cells and bacteria, extending the limits of human understanding.[3, 4] In the late 19th century, the improvement of optical microscopes reached its limit in resolution of ~250 nm due to the diffraction of light.[4] Along the 20th century different techniques with non-optical principles were developed, making accessible the visualization of the biological world at the nanoscale and bringing structural knowledge of biological particles. For example, in 1938 the first virus was observed using electron microscopy (EM).[5] In 1952, the famous *photo 51* was obtained through X-ray crystallography, which revealed a diffraction pattern of the helical nature of the DNA double helix.[6] This technique, together with Nuclear Magnetic Resonance (NMR) some years later, opened the door to the discovery of protein structures, becoming essential in structural biology.[7] In 1986, AFM was invented,[8] and although it does not compete in resolution with EM, it allows nanoscale imaging in near to physiological conditions, nanomanipulation of biological structures and additionally provides valuable information about their mechanical properties.[9] After decades of diffraction limited optical microscopy, this barrier was finally overcome firstly by the scanning near-field optical microscope (SNOM)[10] in the 80s and later, in the 2000s, through far-field microscopy by super-resolution fluorescence microscopy methods,[11, 12] bringing optical microscopy into the nanoscale. **Figure 1** shows different scale objects and the techniques required to resolve them.

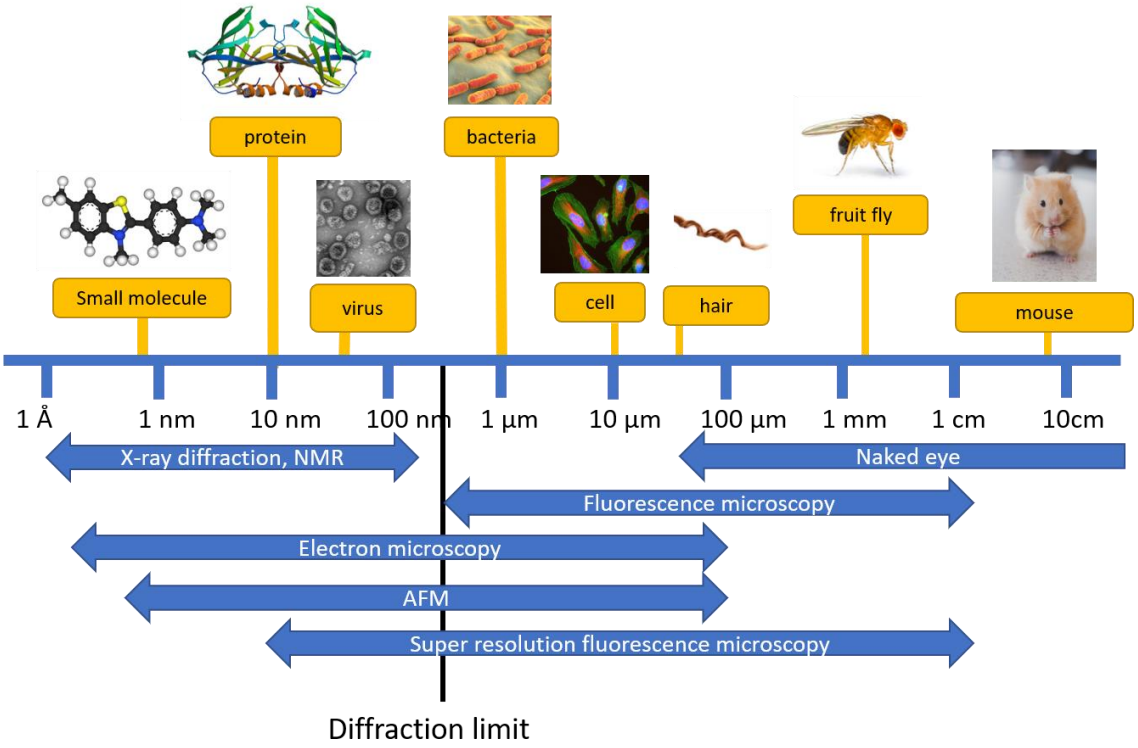

Figure 1. Scale comparison of different size objects and the required imaging techniques to resolve them.

Fundamental biological processes occur in the range of nano- to micrometers, such as protein folding, and errors at this level could result in macroscale effects, such as disease. For example, this is the case of amyloids, a type of misfolded protein aggregates, known for producing toxic effects in different neurodegenerative diseases (i.e. Parkinson's and Alzheimer's disease). On the other hand, these protein structures have exceptional features, like mechanical resistance and functionalization versatility, and are being exploited for a variety of purposes such as the development of new biomaterials.[13, 14] Thus, a deeper understanding of these protein structures has potential applications in several research areas.

This thesis is focused on the development of advanced imaging techniques that combine fluorescence and AFM to provide complementary information at the micro-nanoscale range. Moreover, the thesis explores the application of these methods to study different aspects of amyloid structures that are relevant in the development of novel materials as well as in biomedicine.

Chapter 1

Introduction

1. Introduction

1.1. Nanoscopy

Optical microscopes are systems of lenses that provide a magnified image of an object. However, their resolution is limited by diffraction, which is produced by the interaction of the optical system with light. This causes a loss of information in the localization of a point source, which is detected as an intensity distribution known as point spread function (PSF). When the PSF is projected onto a two-dimensional surface, it shows a circular pattern known as Airy disk (**figure 1.1.a**). As a result, an infinitely small emitting point is observed as a ~250 nm diameter spot, and our ability to differentiate two close points depends on the distance between their Airy pattern (**figure 1.1.b**). Thus, the resolution of an optical microscope is defined by the minimum distance required to distinguish two emitting points. As described by Abbe's equation (**figure 1.1.c**), the resolution depends on the wavelength (λ) and the numerical aperture (NA), which is defined by the refractive index (n) and the angle of light collection (Θ), with a limit of about 200-300 nm.[15, 16] To improve the resolution of the microscope, NA should increase or λ decrease. As a result, some microscopes were developed to use smaller wavelengths than visible light, like the electron beam used for EM.[17] An example of this effect is shown in **figure 1.1.d** and **e,** in which a fluorescence image (**d**) of mitochondria in a COS-7 cell section that expresses a fluorescent protein-tagged cytochrome-C, is compared with an EM image (**e**).[12] In the EM image, structural details that are hidden in the fluorescence image, are revealed. While EM allows better resolution, it is not compatible with living cell conditions since imaging is usually performed under vacuum.[17]

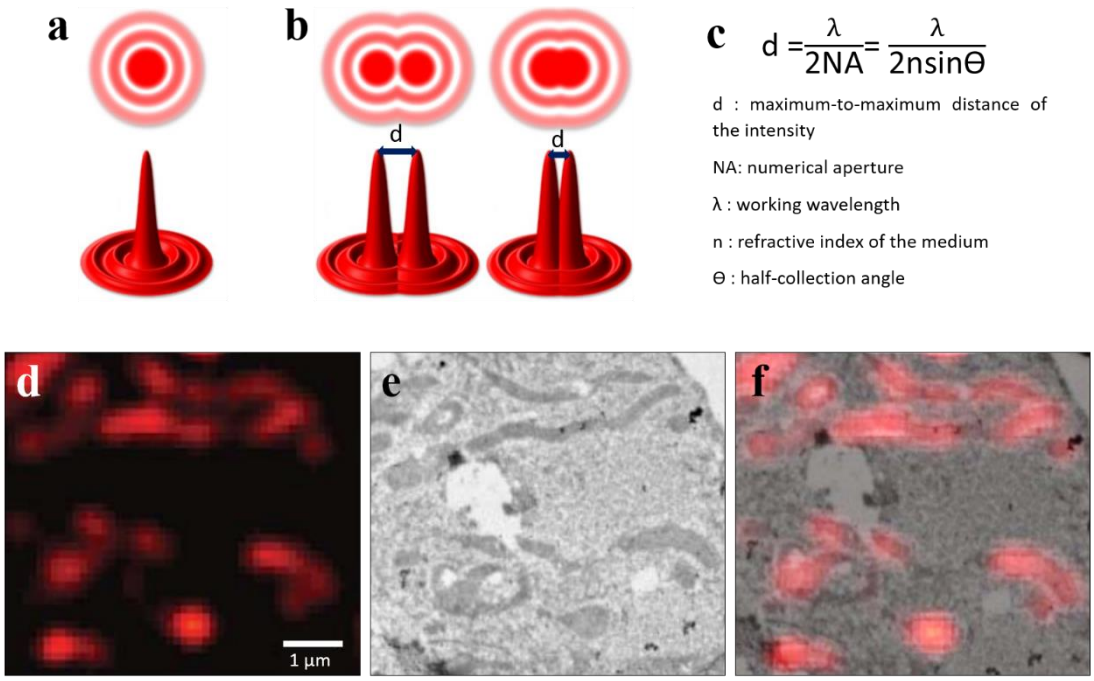

Figure 1.1. Airy pattern and the diffraction limit for optical imaging. a) Airy pattern of an emitting object. b) Two objects can be resolvable if there is enough distance between them to differentiate each Airy pattern. c) Abbe's equation. d) and e) correspond, respectively, to fluorescence and EM images of a COS-7 cell section that expresses a fluorescent protein in the cytochrome-C of mitochondria. f) shows an overlay of both images. Images a-c were adapted from[18] and d-f from.[12]

In the last years, different approaches in optical microscopy have overcome the diffraction limit enabling nanoscale imaging and non-invasiveness. In 2014 the Nobel Prize in Chemistry[19] was awarded to Eric Betzig,[12, 20] William Moerner[21, 22] and Stefan Hell[11, 23] by the development of super-resolution microscopy techniques. As explained below, these methods rely on the use of specific photophysical properties of fluorophores as a fundamental component of the imaging strategy.

The imaging methods that overcome the optical limit of diffraction are named as "nanoscopy". In the context of this thesis, we include AFM in this group of techniques, since it also provides nanoscale information. These methods can be combined for obtaining complementary information of complex systems at the nanoscale, as shown in the following chapters (**figure 1.2**).

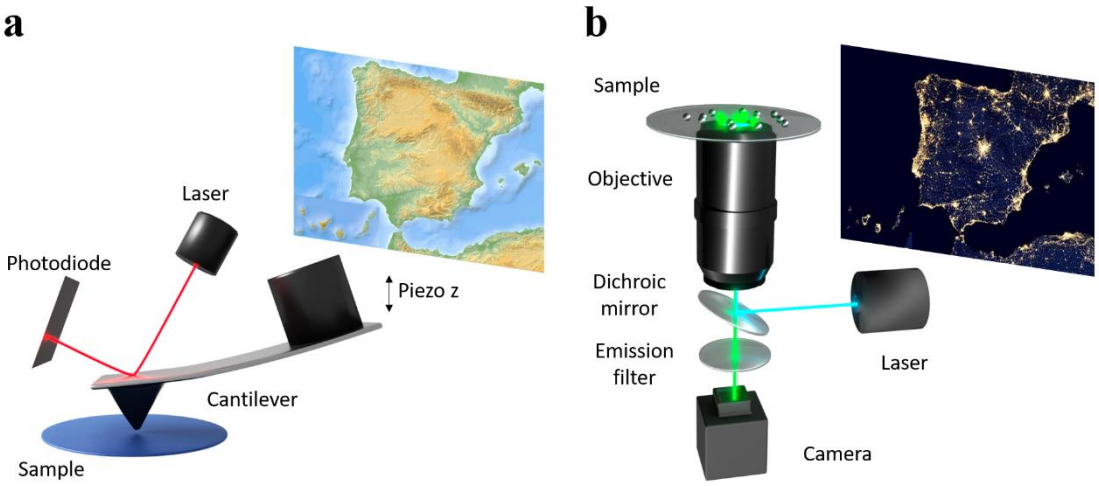

Figure 1.2. AFM and fluorescence microscopy systems. a) AFM provides a topographical map of the sample and fluorescence microscopy (b) produces an image of specifically labelled molecules.

1.1.1. Super-resolution fluorescence microscopy

Fluorescence microscopy is widely used in biology because it is a non-invasive technique that can be used in physiological conditions. It is based on the detection of fluorescent molecules (fluorophores) attached to a molecule or structure of interest within the sample. The fluorophore acts as a reporter that provides contrast in the image. It is able to absorb light energy and, as a consequence, emit light with lower energy (longer wavelength). Thus, in a standard fluorescence microscope a light beam (e.g. a laser) is used to excite the fluorophores and the objective lens focuses the emitted fluorescence from the sample to a detector (e.g. a camera) (**figure 1.2.b**). Although it is extensively used in biology, its images are limited in resolution by the diffraction limit, as mentioned above.

The strategies for optically imaging below the diffraction limit are based in near-field or far-field strategies. In NSOM, the illumination and the sample are at subwavelength distance. The fluorophores are excited with an evanescent wave, which decays very sharply as function of the distance limiting the observation to the sample surface.[24] In contrast, in far-field techniques the distance between the light source and the sample is greater than the wavelength and different approaches can be used to achieve super-

resolution. One strategy focuses on reducing the size of the PSF, for example in stimulated emission depletion (STED) microscopy[25] or structured-illumination microscopy (SIM)[26] among others. Another approach is based on single-molecule localization microscopy (SMLM), which relies on locating single molecules that stochastically switch between "off" and "on" fluorescence states, for instance (direct) stochastic optical reconstruction microscopy ((d)STORM, STORM)[27, 28] or photoactivated localization microscopy (PALM).[12] This thesis deals with SMLM, which stands out for the simplicity of the hardware in comparison with other methods. It allows a relatively easy, wide-field implementation that increases one order of magnitude the resolution of standard fluorescent microscopy.[29]

Sub-diffraction resolution in SMLM is obtained using special fluorophores and specific computational algorithms. During acquisition, the fluorescence signal of the fluorophores in the sample is temporary separated by switching OFF most of the fluorophores and switching ON just a few of them. If the density of emitting fluorophores is sufficiently low, the spacing between them would be higher than the diffraction limit allowing a precise localization of each activated molecule. Thus, a sparse subset of fluorophores is activated at different times and hundreds to thousands of frames are recorded. The registered PSFs in every frame are fitted to a Gaussian function in order to identify the center of the signal and its precise location through computational algorithms. The final image is reconstructed by stacking the localized single molecules in each individual frame (**figure 1.3**). Essential requirements for proper SMLM imaging are: enough signal-to-noise ratio from the emission of an individual fluorophore (and thus high localization precision to determine its position) and higher labelling density than in standard fluorescence, since the average spacing of the labels must be shorter than half of the desired resolution (Nyquist-Shannon criterion for sampling). Acquisition times for SMLM imaging are generally 1 to 5 minutes, therefore it is best suited for imaging static structures.[29, 30]

A key parameter is the choice of the fluorophore employed for SMLM. There is a wide variety, from fluorescent proteins to small molecule fluorescent dyes. Proteins are genetically encoded and can be expressed fused to a protein of interest, thus they do

not suffer from nonspecific binding. On the other hand, fluorescent small molecules typically possess higher brightness, photostability, and photon yields.[31]

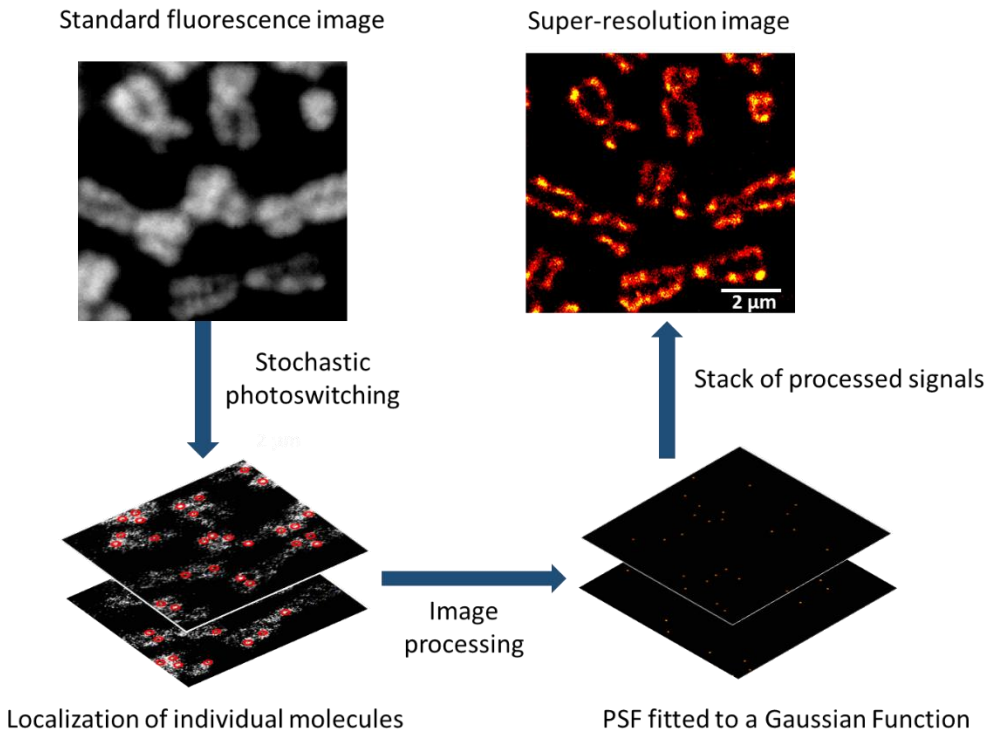

Figure 1.3. SMLM image reconstruction workflow. This figure shows HeLa cell chromosomes labelled with an organic fluorophore (Yo-Pro-1) and imaged in switching buffer (see *3.2.2. SMLM imaging*). Thousands of frames are recorded, and the average image of them is used as standard fluorescence reference. For obtaining the sub-diffraction image, stochastic photoswitching is induced and individual fluorophores are localized. The PSF of each fluorescence signals is fitted to a Gaussian Function and the localized single molecules are stacked, resulting in the super-resolution image.

1.1.2. AFM

AFM is based on the principles of scanning tunneling microscopy and was invented by Binning, Quote and Gerber,[8] who were awarded the Nobel Prize in Physics in 1986. This technique is based on the use of a sharp stylus as a probe to scan the surface of the sample, producing a topographical map. This probe is known as the AFM tip and it bends upon the contact with the sample surface. A laser is reflected from the tip to a photodiode and acts as a detector of the tip bending. A piezoelectric tube is used to control the movement of the tip over the sample, adjusting its movement in Z to the

topography of the sample through a feedback loop from the photodiode signal (**figure 1.2.a**).[32] The key of the success of this technique applied to biology is that it is able to image the sample surface at the nanoscale in physiological conditions.

In addition, AFM is a very versatile tool that can be used for measuring different physical properties. For instance, AFM is able to measure mechanical properties using the tip to apply forces to the sample. The tip is approached and retracted from the sample while applying a force upon contact, which produces as a result a force–distance curve. From these measurements it is possible to quantify height, surface forces, mechanical deformation, elasticity or adhesion forces. Some imaging modes allow acquiring mechanical information while imaging the sample.[33, 34] Remarkably, AFM can be applied to study force spectroscopy at the single-molecule level. This technique relies on using the AFM tip to pull a single molecule until its stability is surpassed.[35] These studies provide information on protein folding and unfolding mechanisms[36] or molecular recognition events.[37, 38] Other properties, such as distribution of electric charge on a surface (electrostatic force microscopy) or magnetic forces (magnetic force microscopy), can be also measured with a tip covered with the appropriate material.[39] AFM can also be used to manipulate or dissect biological structures such us cells[40] or chromosomes,[41] nanoindenting virus[42, 43] or picking up proteins from the membrane.[44]

1.1.3. Correlative nanoscopy

Correlative microscopy is the integration of one or more microscopy techniques for gaining complementary information of the same sample area. Each technique provides information about a specific aspect of the sample, and when they are combined, a more comprehensive understanding of the system can be achieved.

Light microscopy is the main technique used in correlative approaches due to its widespread availability, the possibility to image large sample areas using aqueous environments or the high specificity detecting fluorescently labelled molecules.[45] It has been successfully combined with EM, referred as correlative light and electron microscopy (CLEM) as shown in the example of **figure 1.1.d, e** and **f**.[12, 46-49] It allows to specifically localize a molecule of interest in a high resolution structural image provided

by EM. Other powerful correlative approach is the combination of light microscopy with AFM, which works well in air or in liquid without special sample treatment and allows acquiring nanometer scale images of biological systems.[50] Thus, their combination allows a specific localization of a fluorescent molecule of interest in the topography map. This strategy has been used for example to monitor vesicle exocytosis with fluorescence in combination with AFM to detect membrane changes on the surface of epithelial cells.[51] Another example is imaging by AFM the effect of antimicrobial peptides on a bacterial membrane simultaneously with a live/death fluorescent indicator.[52] Additionally to topographic images, AFM can be exploited for its nanomanipulation capabilities in combination with fluorescence, for example to study virus mechanical properties and monitor the DNA release with fluorescence[53] or to inject fluorescent particles in single cells using AFM and monitoring them by fluorescence microscopy.[54]

The development of super-resolution techniques has now extended optical imaging to a range of about tens of nm, approaching the resolution of EM and AFM, and providing a more meaningful correlation with a much higher degree of structural detail.[12, 55-57] This type of experiment could help to understand complex biological processes, such as virus budding, monitoring cell membrane changes by AFM and fluorescently detecting the proteins of the cell recruited by the virus.[58] Labelling of structures like the cytoskeleton in live cells and monitoring cell surfaces by AFM are helping to understand the interplay between cell structure and migration processes.[55, 59, 60] Furthermore, nanomanipulation can be used for cell nano-surgery[61, 62] and monitored with super-resolution microscopy. An alternative application of correlative AFM and super-resolution microscopy is the identification of artefacts in the latter due to poor labelling, photobleaching, or image reconstruction issues. Thus, the AFM image can be used as "ground truth" to validate and improve novel super-resolution methods.[57, 63, 64] On the other hand, another layer of information has been achieved by combining super-resolution fluorescence for precisely localize the cell organelle of interest, EM for obtaining high resolution structural information and AFM for measuring its mechanical properties.[65]

However, correlative microscopy is challenging, and specific protocols need to be developed before using it to its full potential, as discussed in *Chapter 3*.

1. 2. Amyloid aggregates

Every function in a living cell depends on the proper folding of its proteins. The DNA code determines the amino acid sequence and, as a result of the interaction between amino acids, the protein acquires its secondary structure. Different types of secondary structures are classified as ordered, like α-helix and β-stands, or low ordered like random coils. Their spatial organization constitutes the tertiary structure of the protein and determines its function. In some cases, multiple polypeptide chains or subunits associate to form a macromolecular protein, which constitutes its quaternary structure.[66] Erratic folding of the proteins is associated with diseased conditions as for example the formation of amyloid fibers, which is involved in the development of diabetes type 2 or neurodegenerative conditions.

Amyloid fibers are protein structures predominantly formed by cross-β-stands, which are β-sheet motifs where the hydrogen bonding among β-strands runs parallel to the long fibril axis. Amyloid formation is triggered by a change of the native structure of a protein. It applies to both, globular proteins and intrinsically disordered proteins (IDP), which differ in their native structure. IDPs are typically unstructured and have different folding state depending on their environmental conditions. These are prone to form amyloid fibers without major conformational changes.[67] In contrast, globular proteins are formed by stable native structures and generally require a previous step of unfolding, and in some cases also protein truncation or fragmentation, which can be triggered by diverse conditions, such as low pH, high temperature or denaturing agents.[68] In the fiber formation process, a lag phase can be observed when an unfolded, partially unfolded protein or broken peptide from the original protein, starts to change its structure and forms aggregation-prone species called oligomers. This is followed by the elongation phase, in which the oligomers form and promote the growth of β-sheet stacks through hydrogen bonding interactions, producing protofibrils. These structures interact forming mature fibers and arriving to a *plateau* indicating that the concentration of fibers is stabilized.[69] Additionally, protofibrils and fibers can break and turn into a seed for new fiber formation (**figure 1.4**).[68, 70]

In addition to their biomedical relevance, which will be discussed in more detail in *section 1.2.2*, amyloid structures are exceptional for their mechanical strength, stability and functionalization possibilities.[71] These features lead to a growing interest in amyloid fibers for their potential applications as non-conventional materials,[72] as elaborated below.

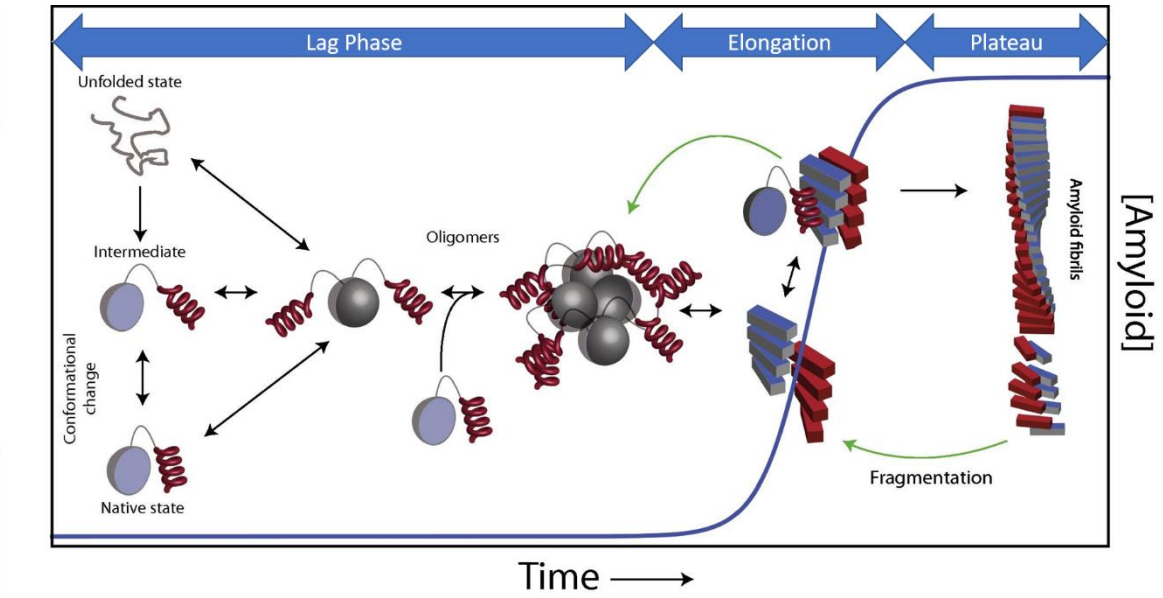

Figure 1.4. Amyloid formation process. Unfolded or partially unfolded peptides suffer a structural change becoming an oligomer and promoting the formation of β-sheet structures (lag phase). β-sheet stacks begin fiber formation (elongation phase) until it arrives to a *plateau*. Formed fibers can break and promote fiber formation. Image modified from the literature.[70]

1.2.1. Amyloid fibers as hybrid materials

Amyloid aggregates were initially associated to disease (see below), but actually they are versatile structures that fulfil a wide range of roles in nature.[13, 14] For example, some bacteria, such as *Pseudomonas aeruginosa* or *Escherichia coli,* use amyloid aggregates as a functional coating for biofilm formation.[73, 74] In fungus, amyloid structures are used to transmit hereditary information[75-78] allowing fast environmental adaptation, such as regulating the nitrogen catabolism depending on the availability of nutrients.[76] Another example is the arrangement of peptide hormones into amyloid structures to regulate their release in humans.[79]

Amyloid fibers typically consist on linear nanostructures with unique mechanical strength and stability, which raise the interest of amyloid fibers as a new biomaterial for different technological applications. Diverse fields are benefiting from their application ranging from biomedicine, as scaffold for cell growth[80, 81] or hybrid composites for bone-mimetic materials,[82] to solar energy conversion,[83] biosensors[71, 84] or materials with strong underwater adhesion.[85] **Figure 1.5** summarizes some of the functions of amyloid as natural and artificial materials.

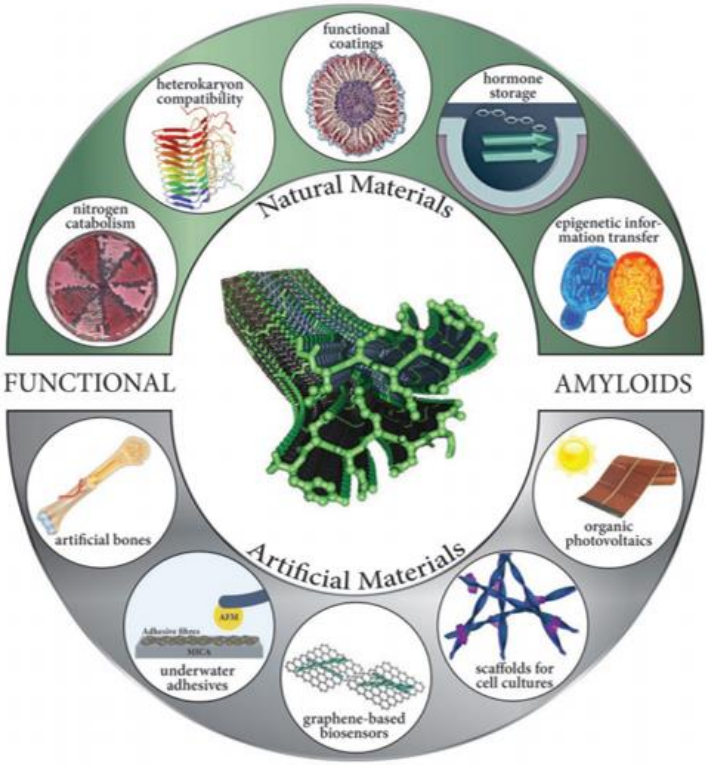

Figure 1.5. Roadmap of different amyloid functions as natural and artificial materials. Image reproduced from.[13]

Research in the field of new nanomaterials has focused its attention on amyloid fibers as nanoscale templates to fabricate 1D inorganic structures.[86] The protein amino acid sequence can be used as anchoring point to functionalize amyloid fibers.[87, 88] This is a huge advantage over other similar structures, such as carbon nanotubes, where the functionality of the surface remains a challenge.[71] An interesting application is the combination of amyloid fibers with nanoparticles forming hybrid nanomaterials with

extraordinary properties such as conductivity, magnetism, or complex optical responses.[13, 89-92] For example, amyloid fibrils interfaced with metal nanoparticles and quantum dots (QDs) have been used to create an environmentally responsive biofilm-based electrical switch [93] and a glucose biosensor platform.[71] Hybrid nanomaterials are therefore increasingly finding applications in different fields such as biomedicine, electronics, biosensing, and imaging.[71, 94, 95]

Hybrid nanomaterials is an emerging field and a deeper understanding of their structure and composition is required in order to create more complex functional materials.[68] An important challenge in the development of hybrid nanomaterials is achieving a reliable control over their functionalization.[71] Due to the hybrid nature of these structures, correlative approaches are particularly well suited as characterization tools for helping to develop these promising nanomaterials.[57, 86]

1.2.2. Amyloid related diseases

Amyloid deposits have been found to be involved in near to 50 pathologies to date.[96] In most of the systems, they are excreted from cells and accumulated in deposits in the extracellular space.[97] The precursor proteins are very heterogenous in terms of sequence or native structure. Some examples of amyloid proteins related to diseases are α-synuclein (α-syn) in Parkinson's or amyloid-β (Aβ) peptides in Alzheimer's. In physiological conditions these proteins are IDPs that play different roles, adapting to the changing cell environment and becoming folded only under specific circumstances.[98] The causes of the disease's onset remain unclear, but they are related to mutations in the precursor,[99, 100] increases in peptide processing to aggregation-prone species[101] or protein accumulation.[102] Furthermore, the protein aggregation rate can be favored by the presence of metals[103] or small molecules, such as cholesterol[104, 105] or polysaccharides[106] in the environment, or by cell dysfunction, like chaperones failing to regulate cell proteostasis.[107, 108] It is under debate which is the main toxic component of the amyloid diseases: oligomers or mature fibers. Generally, fibers have shown limited toxicity compared to the oligomeric intermediates.[109] However, the role of fiber aggregates should not be underestimated since it may be important in the progression and propagation of the disease. These amyloid aggregates are able to interact with the

cell membrane and sequestrate important molecules for cell homeostasis, but additionally, they may act as reservoir of oligomers since fiber breakage fragments could act as seed for new fiber formation.[96]

Recently, cryo-EM and NMR studies have been able to solve some amyloid fiber structures such as α-syn[110, 111] or the most frequent Aβ peptides.[112-114] Solved molecular structures reveal polymorphic organization, thus one precursor can give rise to different molecular organization[113, 114] resulting in diverse fiber morphologies.[115, 116] This polymorphism may explain the different phenotypes and levels of toxicity observed in amyloid diseases.[115-119]

1.2.2.1. Phototherapeutic strategies for amyloid-related diseases

Amyloid-related diseases are associated with high level of mortality worldwide, being Alzheimer's and Parkinson's the main causes of dementia. However, at this moment only symptomatic treatment is being applied, becoming a priority to develop new strategies and discover other targets to find an effective treatment.[120, 121] Fibers and oligomers are the main targets of drug candidates, which directly promote their elimination,[122, 123] inhibit aggregation[124, 125] or reduce precursor protein accumulation.[126] Another strategy is to recover the membrane cholesterol homeostasis,[127, 128] disturb the amyloid-membrane interaction[129, 130] or target the ion channels on lipid membranes caused by amyloid fibers accumulation.[131, 132] A new approach is to design activators or inhibitors of specific chaperones since they have been found to confer neuroprotection in various neurodegenerative diseases[122, 133] or to use engineered chaperones with the ability to dissolve fibers.[134, 135] For these targets, small molecules, peptides, and antibodies have been designed but without clinical success to the date.[120, 136]

Recently, photochemical tools for blocking amyloid aggregation have been explored as another therapeutic alternative. These strategies rely on organic dyes, inorganic complexes or nanostructures as photo-oxygenation catalysts (hereafter photocatalysts), i.e. compounds that are able to photosensitize reactive oxygen species (ROS), typically singlet oxygen. Similar strategies, based on photodynamic therapy, have proven to be

successful for cancer treatment targeting malignant cells.[137] In the case of amyloid related diseases, a range of photocatalysts or photosensitizers such as porphyrins, flavins, rose Bengal, methylene blue, etc[138-141] have shown to produce amyloid aggregate disruption. However, the main limitation of this approach is the lack of selectivity of the produced photodamage: pathogenic aggregates as well as functional forms are all susceptible to photo-oxygenation. To address this issue, switchable photocatalysts have been developed, i.e. compounds that preferentially associate to higher order amyloid aggregates (cross-β-sheet structures) and only produce singlet oxygen in this case, dramatically reducing the damage on functional forms.[142-144] **Figure 1.6** shows the typical mechanism of a switchable photocatalysts, in which it binds specifically the oligomers or fibers but not to the native protein. Upon irradiation, the photocatalyst is only activated if bound to its target producing amyloid structure solubilization.

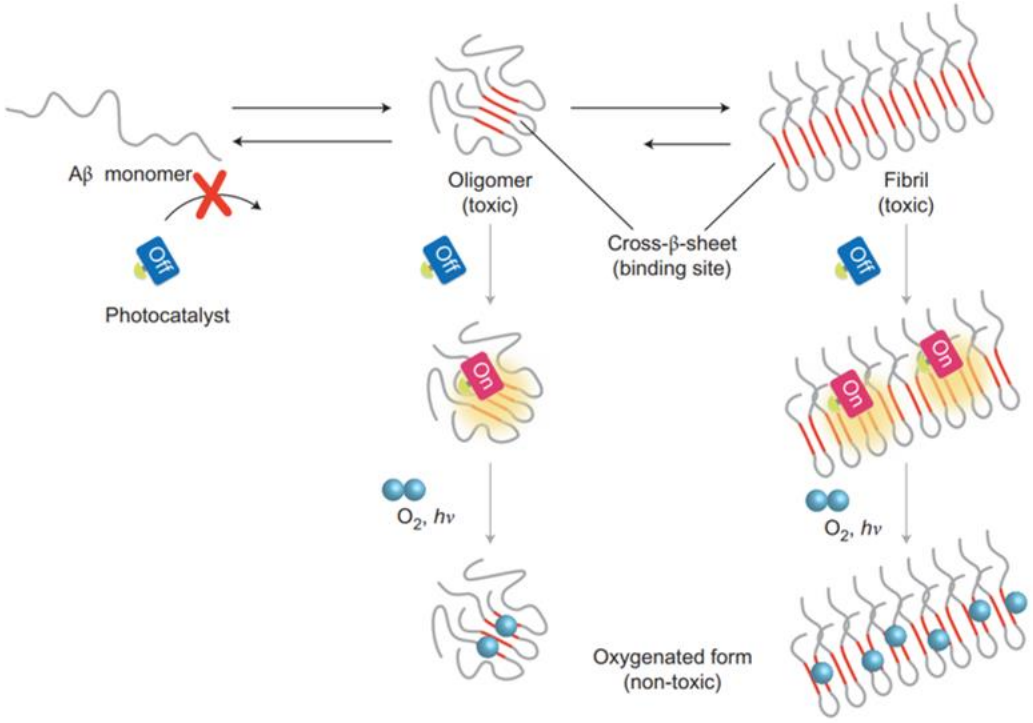

Figure 1.6. Oxygenation mechanism of switchable photocatalysts. The photocatalyst targets the cross-β-sheet structure of amyloid aggregates, both oligomers and fibers. Upon light irradiation it becomes fluorescent and produces ROS oxygenating susceptible amino acids and solubilizing the amyloid aggregates. This image is reproduced from.[143]

1.3. Thesis motivation

Amyloid fibers are widely studied in biomedicine for being involved in different pathological processes but, additionally, their particular features such as mechanical resistance or functionalization possibilities make them interesting in other fields like materials science. In spite of the extensive research, little is known about their structure, formation mechanism or interaction with other molecules. These structures have been widely studied using bulk techniques, but these methods are not able to address the complexity and heterogeneity of amyloid aggregates. A more advanced approach is to apply nanoscale microscopy techniques that are able to provide information at the single-fiber level. This thesis focuses on the characterization of amyloid fibers through a combination of AFM and (super-resolution) fluorescence microscopy to unravel novel information that would have remained masked using traditional techniques.

The combination of these two techniques, which are based on very different principles, is not straightforward. For this reason, this thesis has an important component of technical development and optimization of sample preparation procedures. It is necessary to find a compromise between the requirements and limitations of each technique. These technical challenges have been overcome in this thesis, allowing the study of functionalized amyloid fibers as hybrid biomaterials, as well as the mechanistic understanding of amyloid fiber disassembly in the context of novel phototherapeutic strategies.

1.4. Objectives

The aim of the thesis is the application of AFM and (super-resolution) fluorescence microscopy for the characterization of amyloid fibers in the context of different fields, from new material research to biomedicine. To increase the power of these single-molecule techniques correlative approaches were applied.

The objectives of this thesis are:

1) Development of protocols for applying correlative AFM and (super-resolution) fluorescence microscopy to amyloid fibers labelled with different fluorophores.

2) To obtain relations between topography and dye location/activity in amyloid fibers.

3) Select an appropriate amyloid fibrillar model to study photodamage by AFM.

4) Understand the nanoscale effect of amyloid phototherapeutic strategies using a combination of biochemical techniques and nanoscale imaging.

Chapter 2

General materials and methods

2. General materials and methods

2.1. Correlative AFM and fluorescence microscopy system

Experiments were performed using an adaptation of a commercially available platform that integrates an AFM (Nanowizard II, JPK Instruments) mounted on top of an inverted optical microscope (Nikon Eclipse Ti-U) (**figure 2.1**). This system is placed on an active vibration isolation table (Thorlabs). It has been adapted for SMLM measurements by adding an electron-multiplying charge-coupled device (EMCCD) camera (iXon Ultra 897, Andor Technology). Additionally, light excitation source of the commercial setup was replaced by different lasers.[64]

AFM and fluorescence microscopy/SMLM imaging and analyses was performed independently, and later Fiji[145] software was used for image alignment as discussed in detail in *Chapter 3.*

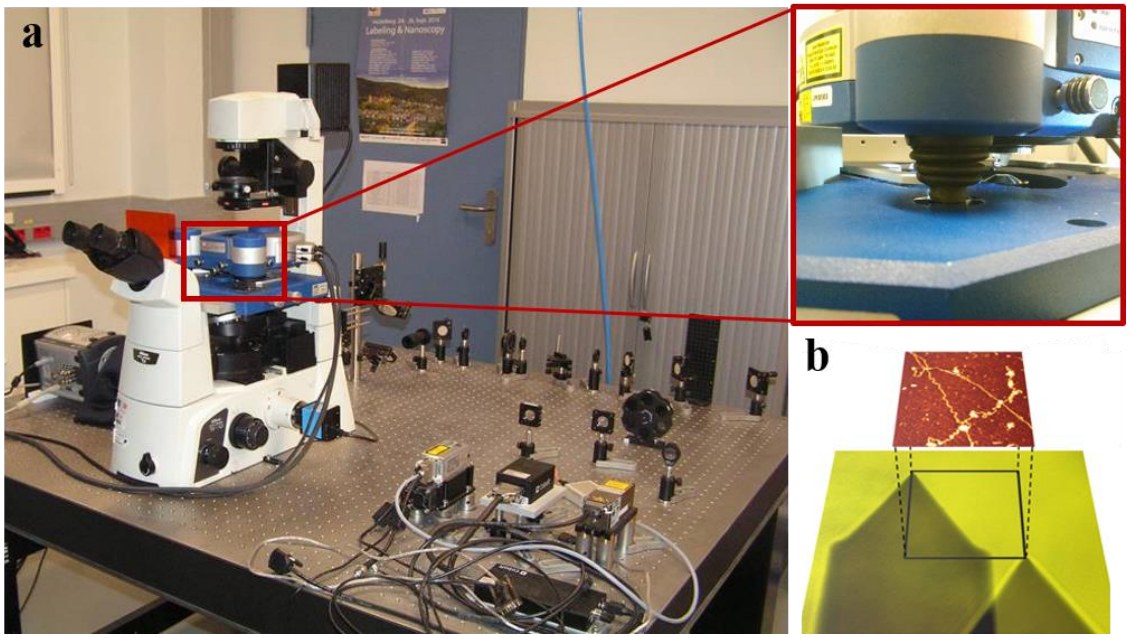

Figure 2.1. Correlative AFM/SMLM in *situ*. a) correlative AFM/SMLM setup. b) alignment of the images is achieved by optically imaging the AFM cantilever. Image is adapted from.[50]

AFM measurements were performed in dynamic mode using HQ:NSC35/Cr-AuBS cantilevers (MikroMasch) of 5-40 N m^{-1} force constant and 150-325 KHz resonance

frequency under dry conditions. It was performed on cleaved mica or in glass if it was used for correlative microscopy. Generally, for AFM measurements, a large image (~ 35x35 μm^2) was taken for selecting a region of interest and later some smaller areas from 10x10 μm^2 to 500x500 nm^2 were imaged. Typically, images of 5x5–10x10 μm^2 with 512x512 pixels were used for image comparison during photodamage experiments (*Chapter 6*). Image processing was performed using Gwyddion.[146] Basic treatment was applied to every image data: plane subtraction, flatten base and rows alignment.

For fluorescence microscopy, a 488 nm laser (Luxx, Omicron) was used as excitation light source. It was expanded, collimated, and focused onto the back focal plane of the objective (TIRF, 60x, 1.49 NA, oil immersion, Nikon). Emission light was selected through a dichroic mirror (z488rdc, Chroma Technology) and different filters that were adapted depending on the fluorophore requirements: HQ500 LP (Chroma Technology), 660/52 (Semrock), 525/50 filter (Semrock). Additional lenses provide a final magnification of 219x, equivalent to a pixel size of 72 nm. In some experiments, SMLM blinking was induced by adding switching buffer (see *3.2.2. SMLM imaging*) containing phosphate-buffered saline (PBS) (pH 7.4, Sigma) with an oxygen scavenger [0.5 mg mL^{-1} glucose oxidase (Sigma), 40 µg mL^{-1} catalase (Sigma), and 10 % w/v glucose (Fischer Scientific)]. Image processing was performed using Localizer[147] software for particle identification and localization, and image reconstruction of the localized coordinates.

2.2. Electron microscopy

EM imaging was performed by the Electron Microscopy Facility of the National Center for Biotechnology (CNB-CSIC) (Madrid, Spain) in a Jeol JEM 1011 transmission electron microscope at 100 kV with a Gatan Erlangshen ES1000w camera. Samples were adsorbed on carbon coated grids and negatively stained with 2% uranyl acetate.

2.3. UV-VIS Absorption Spectroscopy

Absorption spectra were recorded on a Cary 50 UV-vis spectrophotometer in a 1 cm pathlength quartz cuvette.

2.4. Fluorescence Spectroscopy

Fluorescence spectra were acquired using a Fluoromax4 spectrofluorometer (Horiba) in a 1 cm pathlength quartz cuvette.

2.5. Circular Dichroism

Circular Dichroism (CD) spectroscopy was performed on a JASCO J-815 spectropolarimeter using a quartz cuvette with a pathlength of 1 mm.

2.6. MALDI-TOF

Matrix-assisted laser desorption/ionization time-of-flight mass spectrometry (MALDI-TOF) experiments were performed at the Proteomics Facility of the CNB-CSIC in an ABI 4800 MALDI TOF/TOF mass spectrometer (Applied Biosystems). Sinapic acid (SPA) or DHAP (2',4',-Dihydroxyacetophenone) was used as matrix and it is specified in each case.

2.7. Sample preparation

Samples used in *Chapter 3* and *4* were kindly provided by our collaborators in the group of Dr. Natividad Galvez from the University of Granada. Amyloid fiber preparation used for *Chapter 5* and *6* are explained in section *5.3.*

2.7.1. Sample deposition for imaging experiments

For AFM experiments samples were incubated on cleaved mica during 5 min, washed with MQ water (x3) and dried with nitrogen. The same deposition conditions were applied for fluorescence and correlative imaging but using a glass coverslip surface and incubating for 10 min. Previously, glass coverslips were cleaned by 15 min of sonication in different solutions: spectroscopic grade acetone, alkaline detergent (Hellmanex), and ultrapure water. Finally, they were dried with nitrogen.

For improving samples adhesion, functionalization of the surface (mica or glass) with polylysine (PLL) was performed when required. Thus, 100 µl of 0.1% w/v of PLL (Sigma-

Aldrich) were deposited on the surface during 10 min, washed with MQ water and dried with nitrogen. After that, samples were incubated for 10 min, washed and dried as explained.

2.7.2. Fiber purification for bulk experiments

For MALDI-TOF and CD experiments, it is important to avoid signal contribution from free peptides not forming fibers. Thus, the sample was filtered through Amicon ultra-0.5 mL centrifugal filters (Merk, UFC5100) of 100 kDa cutoff in a microcentrifuge. Filters were equilibrated with sample solvent by centrifugation for 15 min at 1000 g. After that, 500 µl of a solution of 1:2 of fiber stock diluted in the solvent of interest were added to the filter and centrifuged for 30 min at 1000 g and 4^{o}C two times. Soft centrifugation was required to avoid fiber breakage. Protein concentration of the filtrate and retentate was measured using a NanoDrop Lite Spectrophotometer (VWR). After a second filtration, the absorbance in the filtrate was near to 0, suggesting that free peptides were removed.

Chapter 3

Methodology development

for correlative SMLM and AFM

3. Methodology development for correlative SMLM and AFM

Adapted from:

Bondia P., Casado S. and Flors C. (2017) Correlative Super-Resolution Fluorescence Imaging and Atomic Force Microscopy for the Characterization of Biological Samples. *In: Erfle H. (eds) Super-Resolution Microscopy. Methods in Molecular Biology,* vol 1663, p 105-113. Humana Press, New York, NY.

Bondia, P., Jurado, R., Casado, S., Domínguez-Vera, J. M., Gálvez, N., and Flors, C. (2017). Hybrid nanoscopy of hybrid nanomaterials. *Small*, *13*(17), 1603784.

3.1. Introduction

Recent advances in imaging tools have greatly improved our ability to analyze the structure and molecular components of a wide range of biological systems at the nanoscale. High resolution imaging can be performed with a handful of techniques, each of them revealing particular features of the sample. A more comprehensive picture of a biological system can be achieved by combining the information provided by complementary imaging methods. However, it is challenging to combine two different techniques since sample protocols preparation are sometimes incompatible or sample can be damage during handling or measurements. These issues become especially important when the resolution of the combined techniques is at the nanoscale. In addition, protocols for image alignment need to be developed for obtaining precision at this resolution range.[45]

The purpose of this chapter is to describe a detailed protocol to combine super-resolution fluorescence microscopy based on SMLM coupled *in situ* with AFM. Specific requirements for the optimal combination of both techniques in terms of sample and substrate preparation, instrumentation, vibration isolation, and image alignment are discussed. Generally, correlative AFM and SMLM experiments are performed sequentially, rather than simultaneously, which simplifies the procedure and is adequate for most applications. To illustrate this, a correlative imaging experiment, in which BLG fibers are labelled with the organic fluorophore Alexa488 or QD655 is

described. These examples are used in this chapter to explain and compare the different experimental strategies in detail, but the scientific significance of the results will be discussed in *Chapter 4* in the context of new hybrid nanomaterials research. Alternative procedures for other types of samples are also explained in this chapter.

3.2. Experimental considerations

Several issues need to be considered before applying correlative microscopy to our sample.

3.2.1. Surface

Choosing a surface for correlative microscopy can be challenging since AFM requires a flat and smooth substrate and SMLM good optical properties for efficient photon detection and precise localization of the fluorophores. Glass or quartz are usually preferred for super-resolution microscopy; however, they have a higher average roughness than mica (0.5 nm for glass[148] or quartz[149] vs 0.05 nm for mica[148]). For small objects such as stretched DNA, which has a height of 2 nm, glass is not flat enough for AFM imaging, and therefore the use mica is recommended. Although mica has poor optical properties (light absorption and birefringence) their impact can be minimized if a very thin layer is used, providing a good compromise for correlative microscopy.[64, 148] For larger structures such as the protein fibers discussed here and in references[57, 150] or cells[55, 60], glass is suitable for AFM. The use of thicker glass coverslips (#2 instead of the more common #1.5 used in SMLM) reduces fluctuations on the sample induced by the tip scanning. A common problem for AFM imaging in liquid environment is that the sample is easily detached from the surface. Functionalization of the surface can improve adsorption, typically by electrostatic interaction and a wide variety of options can be found in the literature. A common method is to coat the surface with PLL, whose positive charge is advantageous for adhesion of negatively charged structures such as bare DNA or cells,[55, 64] which are able to grow on the PLL functionalized glass.[151] Another possibility is to functionalize with cross-linking groups such as 3-aminopropyltriethoxysilane (APTES) which protonates at neutral pH.[55] However, surface functionalization could

affect the native structure of the molecules of interest, and it may decrease the flatness and optical properties of the surface.

3.2.2. SMLM imaging

A critical factor for obtaining a proper SMLM image is the fluorophore choice. A wide variety of switching fluorophores are commercially available but they may have different photoswitching requirements. Organic fluorophores typically need a "switching buffer", in which an oxygen scavenger system formed by glucose oxidase and catalase consumes the glucose added to the solution in the presence of oxygen. This reaction creates a situation of hypoxia which increases the triplet lifetime of the fluorophore by preventing oxygen-based reactions and maximixing the chance of photoinduced (redox) reactions with the final component of the switching buffer, a primary thiol compound such as β-mercaptoetanol or cysteamine (typically ~ 50 mM).[27] For this reason, BLG-Alexa488 experiments were performed in the presence of an oxygen scavenger system. However, the switching buffer did not contain a thiol compound since thiols were observed to induce breakage of BLG fibers[57] and blinking of Alexa488 has been reported not to improve by the thiol addion.[152]

Other labels, such as QDs, intrinsically produce emission fluctuations upon irradiation. These fluorescence fluctuations allow separating in time the emission of each QD and to use various super-resolution imaging schemes to reconstruct QDs distribution with a spatial resolution below the diffraction limit of light.[153-158] However the fact that their blinking properties are heterogeneous within a population and occur in a wide range of time scales typically deteriorates the quality of the super-resolution images.[156]

It is worth considering that if the AFM instrument uses a red detection laser, the fluorophore should be carefully selected since it could bleach during AFM imaging. This problem has been described for example for Alexa647.[55] A possible solution to avoid undesired fluorophore excitation is using an AFM instrument equipped with infrared laser, for example the system used in this thesis uses an 859 nm laser. As an alternative,

SMLM could be performed before AFM, although it could be detrimental to AFM imaging (see *3.2.5. Order of measurement*).

3.2.3. AFM imaging

Different AFM measuring modes are available. Briefly, contact mode is based on measuring changes in topography while the tip of the cantilever remains in contact with the sample.[8] In this mode, the sample experiences high lateral forces that could produce damage. For biological samples, softer methods such as dynamic or jumping mode should be applied. For imaging BLG-Alexa488 and BLG-QD655 dynamic mode was used, in which the cantilever tip oscillates near its resonance frequency (generally about 200–400 kHz) lightly tapping the surface.[159] Jumping mode, which achieves a careful control of the forces applied to the sample by bringing the tip in and out of contact, would also be suitable.[160] It is critical to select a proper cantilever that should be adapted for each measurement depending on the sample, measuring medium and imaging mode. In general terms, softer cantilevers are usually used in contact mode, with spring constants usually lower than 0.5 N/m. In dynamic mode, stiffer cantilevers with a spring constant near 10 N/m are more stable for measuring in air. For jumping mode, soft cantilevers would be recommended to avoid damage of the sample during acquisition.[161]

AFM can be performed in dry conditions or in liquid environment. Measurement in air is more convenient since the sample has better adhesion to the surface and the cantilever tuning is simpler. However, to address biological questions, measurements near to physiological environment provide more relevant conclusions since drying of biological samples could modify their structure.[162] For both examples discussed here, BLG-Alexa488 and BLG-QD655, it was not required to measure AFM in liquid, therefore it was performed in air for simplicity. See *section 3.2.5. Order of measurement* for more details.

3.2.4. Vibration problems

Vibration could be a critical problem as it blurs the AFM image. In addition to an active vibration isolation table, other issues need to be considered when the AFM and the

optical microscope are integrated on the same system. For example, it is helpful to slightly retract the objective during AFM scanning to reduce coupled vibration. The EMCCD camera should be off to avoid fan vibration, or if simultaneous measurement is required, a water-cooling system is recommended. The lasers used for SMLM should have a heat sink instead of a fan (or the fan should be turned off during AFM imaging). Acoustic noise, air flow (like air conditioning), and large variations in room temperature should be avoided. Vibrations could be minimized by placing the instrument inside an acoustic isolation box, and additional isolation of the AFM by holding it on a mechanical support without contacting the microscope body could be helpful.[55]

3.2.5. Order of measurement

The order of imaging can be modified and must be carefully evaluated for each correlative experiment. Generally, it is advisable to perform AFM before SMLM imaging since the switching buffer components (especially enzymes) could interact with the AFM tip and be adsorbed on the sample surface. Additionally, some structures like actin become damaged by laser exposure during SMLM image acquisition, and therefore AFM must be performed in advance, although with low peak forces to avoid mechanical damage of the sample.[55] If for some reason SMLM has to be performed first, exhaustive washing should be done before AFM. However, this very probably leads to sample disturbance.[55, 150, 163]

Before correlative measurement, it is advisable to select a region of interest using standard fluorescence microscopy. It should be performed using minimum laser intensity to avoid photobleaching.

For correlative microscopy characterization of BLG-Alexa488 and BLG-QD655, imaging was performed as follows:

In both cases, the region of interest was previously selected by standard fluorescence microscopy in air at low laser power. For BLG-Alexa488, AFM imaging was performed in air, followed by the addition of the switching buffer (with great care not to move the sample) and SMLM acquisition at high laser power. On the other hand, BLG-QD655 does not require the addition of buffer to induce blinking and therefore the order of

measurement is less critical. In the BLG-QD655 experiments reported here, it was advantageous to perform a preliminary evaluation of the QD blinking in the selected area, since on/off distribution is difficult to predict, as previously explained. If the blinking dynamics were satisfactory, a SMLM dataset was acquired. Afterwards, the objective was slightly retracted and AFM imaging was performed.[57]

3.3. Data analysis

3.3.1. SMLM and AFM

Raw images from both techniques should be processed and analyzed following the same procedures as with the individual techniques. A wide range of software tools are available either open-source or commercially. For the examples reported here, Localizer[147] and Gwyddion[146] and were chosen to perform standard analyses of SMLM and AFM images, respectively.

For SMLM analysis, PSF width and threshold sensitivity values should be adjusted for each experiment for optimal image segmentation, determining which signal is considered as a fluorescent emitter. Lower threshold sensitivity results in higher recall rates, increasing the localization density but maybe blurring some structural details due to the larger localization uncertainty. In contrast, restrictive conditions allow more precise particle localization but may hide part of the fluorophores.[64] Comparison of the SMLM with the AFM image helps finding the best analysis parameters to obtain a balance between spatial resolution and localization density.[64] For example, lower fluorescent intensity was detected for BLG-Alexa488 than for BLG-QD, requiring less restrictive conditions for image segmentation. In contrast, more restrictive values were used for QD image reconstruction but carefully selected in an iterative process explained below (**figure 3.1** and section *3.3.3. Correlative image inspection*).

In correlative approaches, vibration problems discussed previously may introduce noise in the AFM images, which could be reduced by removing noise frequencies through Fast Fourier Transform (FFT) filter.[164]

3.3.2. Image alignment

A critical step for correlative microscopy is image alignment or registration. In our integrated system, AFM and SMLM images are localized in the same region of interest since they are performed *in situ* (**figure 2.1**). For imaging the same region, the AFM tip is located through observation in the optical image. Then, both images can be aligned by using recognizable features of the samples, which was the procedure applied for BLG-Alexa488 imaging and to preliminary align BLG-QD655 images (see below). For a more accurate alignment, software such as DirectOverlay™ (JPK) can be used. This software uses a set of 25 known positions of the cantilever to calibrate the optical image at each point in relation to the AFM lateral piezo coordinates. This allows automatic image registration and distortion correction.[56] However, other methods are necessary if higher precision is required. Fiduciary markers, such as nano-patterned slides with gold fiduciary features fabricated by electron beam lithography, give contrast in topographic and optical images and can be used as references to obtain an accurate overlay.[150, 163, 165] Similarly, fluorescent nanoparticles facilitate the identification of the same region by both techniques and can be used to determine image overlay.[57, 148, 166, 167] This strategy was followed for fine alignment of BLG-QD655 correlative images, in which the detached QDs on the surface were used as fiduciary markers since they are fluorescent particles with ~ 8 nm in height. Using Fiji software,[145] corresponding QDs were located in both images and used as a reference to calculate a correction matrix achieving image overlay at the nanoscale (**figure 3.1**).

3.3.3. Correlative image inspection

One possible application of correlative imaging is the comparison of different image reconstruction parameters in SMLM, using the AFM image as "ground truth".[64] As it was previously explained, although QD emits high fluorescence signal, blinking heterogeneity decreases the localization precision of the signal. For that reason, analysis parameters in Localizer were tuned using AFM image as a reference, increasing the accuracy of QD signal localization and avoiding the introduction of artefacts (**figure 3.1**).

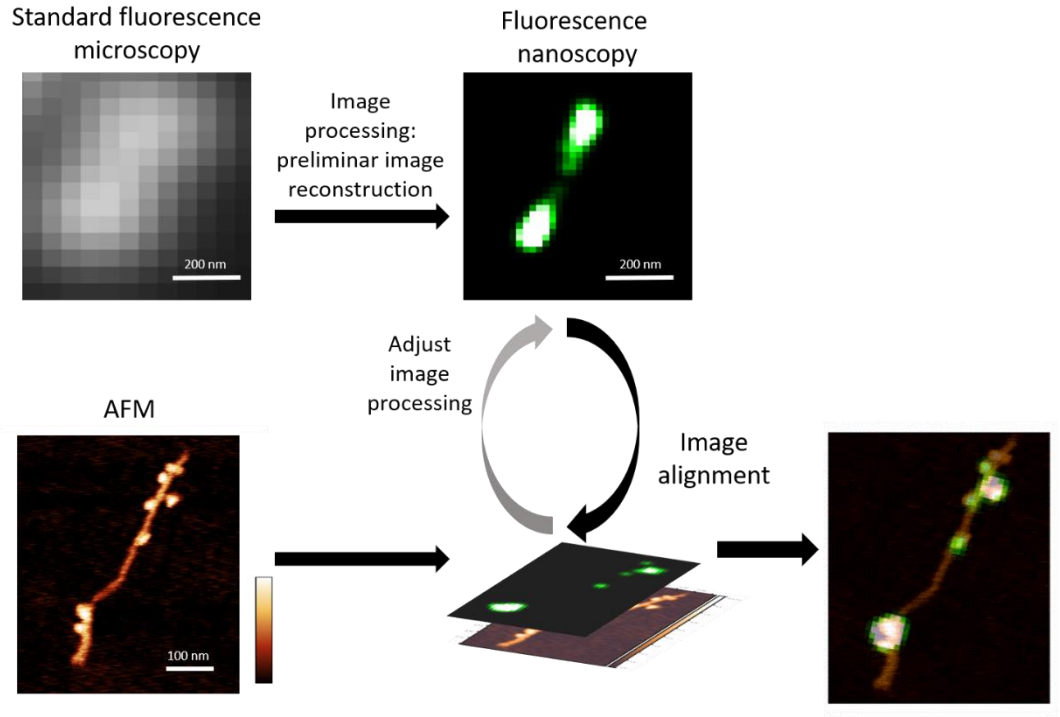

Figure 3.1. High precision image alignment workflow. A data set of ~800 frames was processed to obtain a preliminary super-resolution image. Then, it was aligned with the AFM image using detached QDs on the surface as fiduciary markers (not shown in the image). SMLM analysis parameters were tuned using the AFM image as a reference to obtain an optimal reconstructed super-resolution image.

3.4. Conclusion

This chapter explains in detail the experimental considerations to plan a correlative SMLM and AFM experiment. The challenge of using two different techniques *in situ* and the need of compromises that accommodate the requirements of each of them are discussed. Careful analysis of several aspects of sample preparation, setup and image analysis are key for acquiring high quality data to evaluate the functionalization of BLG with different fluorescent molecules. These experiments provide valuable information in the context of hybrid material development as described in *Chapter 4*. Moreover, it establishes the basis to perform future correlative SMLM and AFM microscopy experiments of amyloid fibers and other biological samples.

Chapter 4

Application of correlative microscopy for hybrid materials

4. Application of correlative microscopy for hybrid materials

Adapted from:

Bondia, P., Jurado, R., Casado, S., Domínguez-Vera, J. M., Gálvez, N., and Flors, C. (2017). Hybrid nanoscopy of hybrid nanomaterials. *Small*, *13*(17), 1603784.

Jurado, R., Castello, F., Bondia, P., Casado, S., Flors, C., Cuesta, R., Domínguez-Vera, J.M., Orte, A. and Gálvez, N. (2016). Apoferritin fibers: a new template for 1D fluorescent hybrid nanostructures. *Nanoscale*, 8(18), pp.9648-9656.

4.1. Introduction

The use of proteins and peptides to drive the assembly of novel bioinorganic structures is a strategy that has been harnessed by nanotechnology in order to confer these assemblies with new physical properties.[94, 168] Proteins are versatile building blocks that provide a simple route to control the template of 0D–3D structures. Amyloid-like fibers, either natural or synthetic, and self-assembling peptides have shown excellent properties as templates for the production of 1D inorganic nanostructures and are emerging as an important class of functional materials.[13, 72, 169, 170]

As a result of the hybrid nature of these materials, the combination of complementary techniques for their characterization at the nanoscale is valuable to gain a comprehensive picture of their structure and function, with the aim of optimizing their design. Here we show that correlative AFM and SMLM is a useful tool to obtain complementary information about protein fibrils functionalized with organic fluorophores and quantum dots, the latter as an example of 1D nanoparticle arrays. For this chapter, we applied correlative microscopy for the characterization of hybrid materials formed by BLG functionalized with Alexa488 and QDs (QD655 and/or QD525) using Lys amino acid as anchor point.[57, 86]

BLG fibers show interesting structural features such as helical twisting with characteristic periodic fluctuations in their height that can be quantitatively studied by AFM.[171] On the other hand, SMLM can provide information about the spatial distribution of the fluorescent labels attached to the fibrils. Our study shows that this hybrid

nanoscopy technique is particularly well suited to study the structure and labelling of these fibers at the nanoscale, which is key in their development as building blocks for functional materials.[13] Moreover, we achieve correlative AFM and two-color super-resolution fluorescence imaging of these hybrid materials. This is the first time that the latter study has been performed and represents an important step forward in the characterization of multifunctionalized hybrid materials.

4.2. Results and discussion

4.2.1. Characterization of BLG functionalized with Alexa488

Functionalized BLG samples described in this chapter were provided by our collaborators in the group of Dr. Natividad Galvez from the University of Granada. BLG was functionalized with Alexa488, which is an intensely fluorescent dye able to produce photoblinking.[152] The dye is a succinimidyl ester derivative able to form amide bonds with the amine group of the proteins and generating conjugates with high photostability.[86]

Standard fluorescence microscopy in correlation with AFM was applied to confirm proper functionalization of the fibers. Correlative microscopy shows that BLG can be readily functionalized with Alexa488 after amyloid-like fiber formation to yield fluorescent fibers that appear homogeneously fluorescent at the spatial resolution provided by standard fluorescence microscopy (**figure 4.1**).[86]

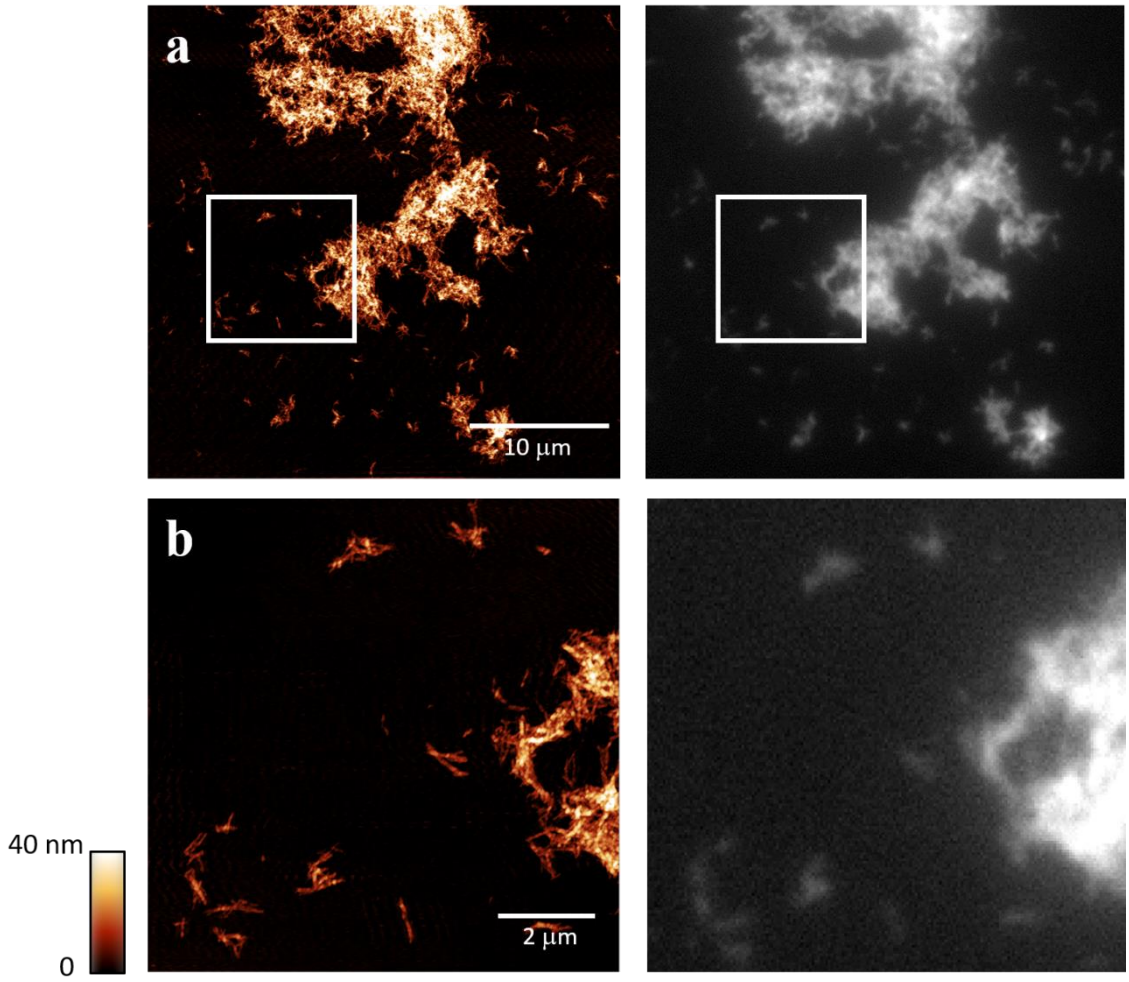

Figure 4.1. Correlative AFM and standard fluorescence imaging of BLG-Alexa488. a) Topographic image (left) is compared with fluorescence image (right) confirming fluorophore attachment to the fiber. b) is the zoom of the squared area in a). Image adapted from.[86]

However, to gain information about the labelling quality at the nanoscale higher spatial resolution in optical microscopy was required, and correlative AFM and SMLM was applied. **Figure 4.2** shows standard fluorescence images, super-resolution images, and AFM images of the same area of BLG-Alexa488 fibers deposited on glass. At the zoom level of the images, standard fluorescence microscopy hardly gives any information. In contrast, the super-resolution image shows clear features, which correspond very well to those of AFM. The correlative nature of these experiments allows to discriminate between "real" localizations in the super-resolution image and spurious ones that are related, e.g., to nonspecific binding, as seen in **figure 4.2**. Importantly, the super-resolution image reveals labelling heterogeneity at the

nanoscale, which can be gauged from the comparison with the corresponding AFM image.

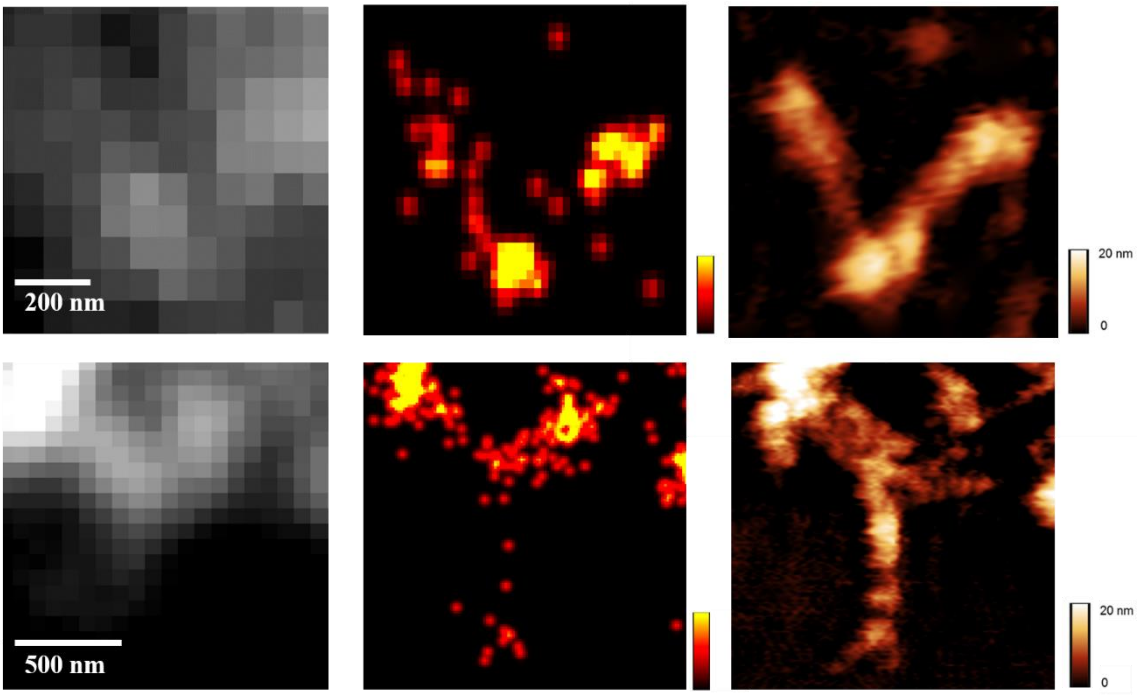

Figure 4.2. Correlative standard fluorescence imaging, SMLM and AFM of fibers BLG-Alexa488. Standard fluorescence imaging (left), super-resolution imaging (center), and AFM (right) of BLG fibers showing heterogeneous labelling with Alexa488 at the nanoscale. For SMLM imaging 4000 frames of 100 ms were collected using a 488 nm laser with an intensity of ~0.5 kW cm^{-2}. The false color scale in the central panel indicates relative fluorophore localization density.

4.2.2. Characterization of BLG functionalized with QD

In addition, BLG fibers functionalized with carboxyl-coated CdSe QD (QD655) by crosslinking, were imaged with the hybrid setup. **Figure 4.3** shows an AFM image in which the QDs are clearly observed attached to the fiber. The labelling density is not homogeneous along the fiber, with some sections where the QDs seem to overlap, while others are not functionalized. The height of the QDs is about 8 nm and that of the fiber is slightly above 3 nm. The latter value is consistent with a single BLG fibril as opposed to a twisted multistranded fibril.[171]

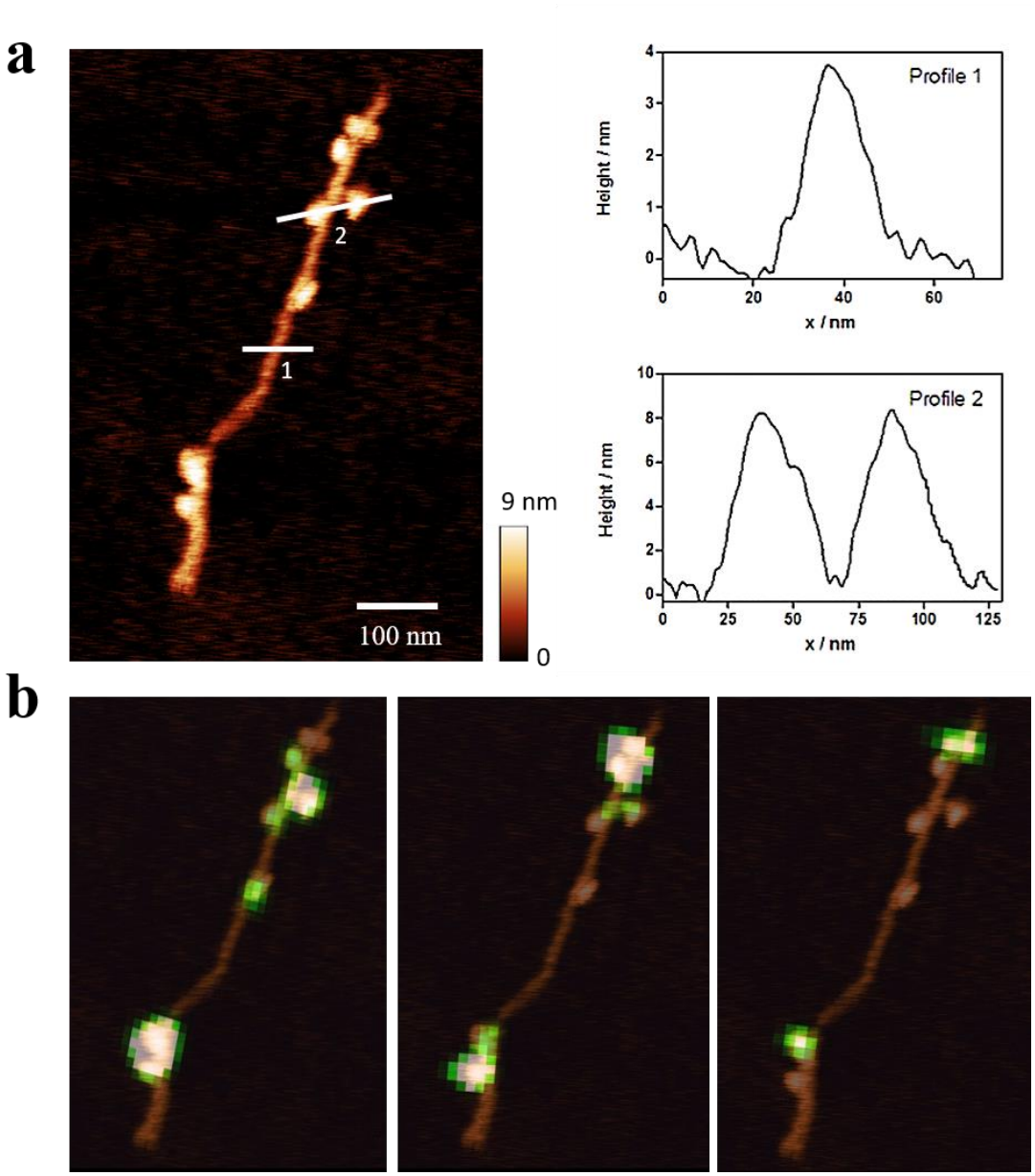

Figure 4.3. Correlative AFM and SMLM of BLG-QD655. a) AFM image (left) and topography profile (right) of a BLG fiber functionalized with QD655. b) Overlay of AFM image and super-resolution images reconstructed from three different data sets of the same fiber in (a). Each data set is built up from about 800 frames of 100 ms per frame using a 488 nm laser with an intensity of ~0.8 kW cm^{-2}.[57]

This data show QDs separated by subdiffraction distances, and that most, if not all, of the QDs in this particular sample emit at some point during the acquisition time. While data in **figure 4.3.b** alone do not allow to extract reliable statistics, previous work has estimated a significant dark fraction of QDs.[172, 173] However, more recent measurements in which the observation times for individual QDs were much longer (in the order of

minutes, similar to the total integration time of our three data sets) showed only a small nonemitting fraction (about 15%).[174] We have indeed observed a small fraction of dark QDs in other samples (**figure 4.5**).

In addition to the super-resolution reconstructed image and topography, information about blinking dynamics on a fast timescale (100 ms in this case) can be overlaid by color coding the appearance of localization events (**figure 4.4**),[147] showing QD heterogeneous blinking at different time scales.[156]

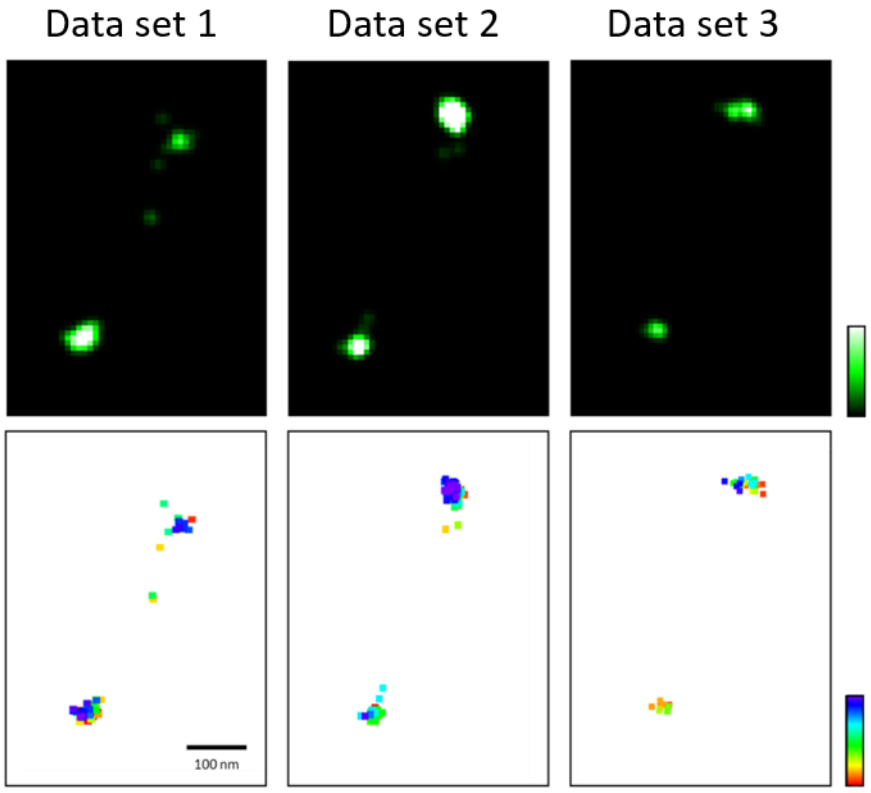

Figure 4.4. Relative localization density and raw localization data of BLG-QD655. Super-resolution images (top) and raw localization data (bottom) obtained from three different data sets of a BLG fiber functionalized with QD655 (same as **Figure 4.3**). The false color scale in the super-resolution image indicates relative localization density and in the raw localization data the color code indicates frame number.

4.2.3. Multicolor correlative microscopy

In order to challenge the capabilities of our hybrid setup, a more complex sample in which BLG was functionalized with both QD655 and QD525 was studied.

The multicolor fluorescent sample was then imaged with the correlative SMLM/AFM. First, the topography image reveals relevant structural information about the protein fibers (**figure 4.5.a**). The height of BLG fibers can be directly related to the number of twisted filaments that compose the fiber,[171] i.e., heights of about 4, 6, and 8 nm correspond to two, three, and four filaments, respectively, per fiber. Filament twisting induces periodic fluctuations in height along the fiber,[171] which are also observed in one section with a period of 40 nm, consistent with a fiber composed by two filaments. To obtain information about the properties of the attached QDs, a super-resolution reconstructed image in two colors can be overlaid with the AFM image and clearly allows the identification of QDs emitting in their respective colors as well as those nonemitting, which would not be possible with the individual techniques. This is the first time that correlated topography and multicolor super-resolution imaging is achieved. This hybrid nanoscopy technique has great potential to study multifunctional hybrid materials,[71, 89, 175] especially since nanocrystals are characterized by the presence of a significant dark fraction population. In addition, features such as fibril twisting are extremely challenging to study by super-resolution fluorescence imaging and relatively simpler with AFM.

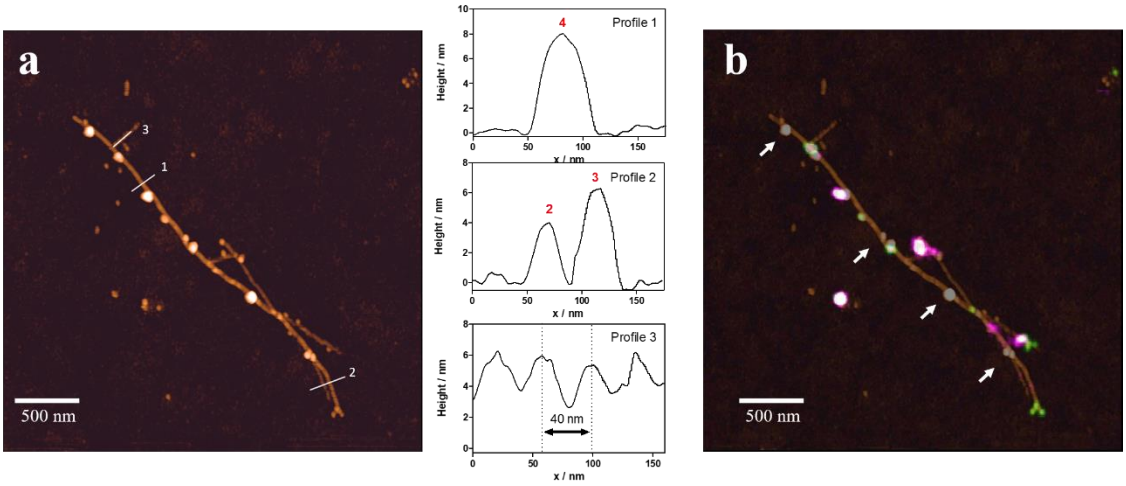

Figure 4.5. Correlative AFM and two-color SMLM of BLG fibers labelled with QD525 and QD655. a) AFM image and topographic profiles of the functionalized fibers. The red numbers in Profiles 1 and 2 correspond to the number of filaments that compose the fiber as expected from the height values.[171] The periodicity observed in Profile 3 is consistent with a fiber composed by two filaments. b) Correlative AFM and two-color super-resolution image. SMLM was built up from one data set for each QD of ~ 1000 frames of 100 ms per frame using a 488 nm laser with an intensity of ~ 0.8 kW cm^{-2}. The arrows highlight examples of nonemitting QDs.

4.3. Conclusion

Hybrid nanoscopy combining AFM and super-resolution imaging provides valuable complementary information about the structure and properties of luminescent hybrid nanomaterials. This is exemplified in this work with amyloid-like fibers functionalized with organic fluorophores, as well as with 1D arrays of QDs templated by these fibers. While the topography image allowed determining the number of filaments that composed the fiber, the super-resolution image (in one or two colors) allowed the identification of emissive and nonemissive QDs. This combined insight would not be possible with the individual techniques.

Other nanomaterials such as luminescent nanoparticle arrays or chains would also benefit from this correlative technique,[175, 176] especially multicolor fluorescent nanosystems where different nanoparticles emit in different colors or are combined with organic fluorophores.[89, 175] Moreover, super-resolution imaging in combination with the nanomanipulation capabilities of AFM[61, 177] offers great promise to understand potential relations between optical and mechanical properties at the nanoscale in hybrid nanomaterials. The novel insight gained with these techniques can drive the design of improved luminescent nanomaterials for bioimaging, biosensing, and many other different applications.

Chapter 5

Fibrillar amyloids as models for photodamage experiments

Part of these experiments were performed in department of Medicinal Chemistry at the University of Tokyo in the laboratory of Prof. Motomu Kanai and Dr. Youhei Sohma

5. Fibrillar amyloids as models for photodamage experiments

5.1. Introduction

Although amyloid fibers share common core features (i.e. cross-β sheet pattern), there are significant differences in their molecular conformations, resulting in highly polymorphic structures.[115, 116] As groundwork for *Chapter 6*, which deals with photochemical strategies to damage amyloid aggregates, the aim of this chapter is to explore different morphologies of amyloid fibers in order to select the most convenient models to study fiber photodamage (i.e. rupture) at the nanoscale by AFM. To that end, the work described here was focused on finding long and isolated fibers easily visualized by AFM. To select a proper model, different amyloid fibers were evaluated: α-syn and Aβ, for being involved in neurodegenerative diseases,[178, 179] and some variations thereof which form alternatives morphologies as explained below. Also, BLG was considered for its well-known amyloid structure.[171]

Another important consideration is that the photodamage experiments in *Chapter 6* rely on the production of ROS for damaging the amyloid fibers.[142, 143] Thus, the presence in the protein sequence of amino acids susceptible to oxidation such as His or Met among others could be important for the extent of photodamage.[143, 180]

5.2. Fibrillar model candidates for photodamage experiments

5.2.1. α-syn, ΔH1 and ΔN

α-Syn is an IDP formed by 140-residues that is expressed extensively in neurons.[181] Its function remains unclear, but it is able to interact with fatty acids and many different proteins involved in diverse functions like vesicle trafficking or neurotransmitter release.[182] It is the main component of the proteinaceous deposits involved in neurological diseases such as Parkinson, multiple system atrophy and dementia with Lewy bodies.[183] Different causes, like mutations or overexpression of

α-syn, promote oligomerization and amyloid fiber formation inducing neuron death.[184]

α-Syn is divided it three different regions: an amphiphilic, basic N-terminal region, a central hydrophobic region (non-Aβ component; NAC) which is responsible for β-sheet structure and the fibrillation process, and a very negatively charged, unstructured C-terminal region[184, 185] (**figure 5.1**). α-Syn truncated derivates without the N-terminal region are also found to form amyloid fibers and have an important role as a seed for new aggregates.[186, 187] Two N-terminal truncated mutants were observed by our collaborator Dr. Begoña Sot (IMDEA Nanoscience) to form long and isolated fibers (**figure 5.5 a, b** and **c**), thus they were evaluated as possible candidates for photodamage studies. Mutations involved a deletion in the N-terminal region of 1-37 and 1-63 amino acids for ΔH1 and ΔN mutants, respectively, as shown in **figure 5.1**.[184] It should be noted that some of the amino acids susceptible to oxidation are deleted in ΔN in comparison with ΔH1, which could be helpful to analyze the influence of specific amino acids in photodamage[143, 180] (see *Chapter 6*).

Figure 5.1. Amino acid sequence of α-syn and mutants ΔH1 and ΔN. The blue, yellow and purple colors indicate the different regions of the proteins (N-terminal, NAC and C-terminal, respectively). The grey sequence indicates the deleted part of the mutants and the amino acids susceptible to oxidation are highlighted in red.

5.2.2. Aβs: Aβ 1-42, Aβ lactam 1-40 and Aβ lactam 1-40 SO

Aβ is a 38- to 43- amino acid peptide generated after enzymatic cleavage of the Amyloid Precursor Protein (APP). Although its physiological function is unclear, Aβ would play an important role in brain development, memory and synaptic plasticity.[188-190] Aβ is normally produced in healthy individuals, but under certain circumstances, this molecule aggregates forming an accumulation of extracellular senile plaques, which are involved in Alzheimer's disease progression.[191] Isoforms Aβ 1-40 and Aβ 1-42 peptide are the most common forms of Aβ found in both diseased and normal human brains.[192] Although polymorphism in the formed fibers has been observed,[113] generally, Aβ 1-40 forms longer and thinner fibers than Aβ 1-42,[193] being more appropriate as a model fiber for photodamage experiments. To further increase fiber homogeneity and to obtain more reproducible results, the Aβ 1-40 peptides used in this study contain a lactam bridge formed between Asp23 and Lys28, mimicking the salt bridge formed on the non-modified structures (**figure 5.2**). This strategy accelerates fibrogenesis since salt bridge formation entails a kinetic barrier to fibril formation. Importantly, the lactam bridge (D23/K28) reduces the number of resulting fibrillated structures, since it limits the possible conformations of Aβ 1-40.[194]

Additionally, a variant of Aβ 1-40 lactam that contains a sulfoxide (SO) modification in the Met 35 was synthetized to evaluate its morphology. This modification has been detected in a proportion of Aβ1-40 peptides in patients' amyloid plaques.[195, 196] Therefore, exploring photodamage effects on fibers containing SO modification could have biomedical interest.

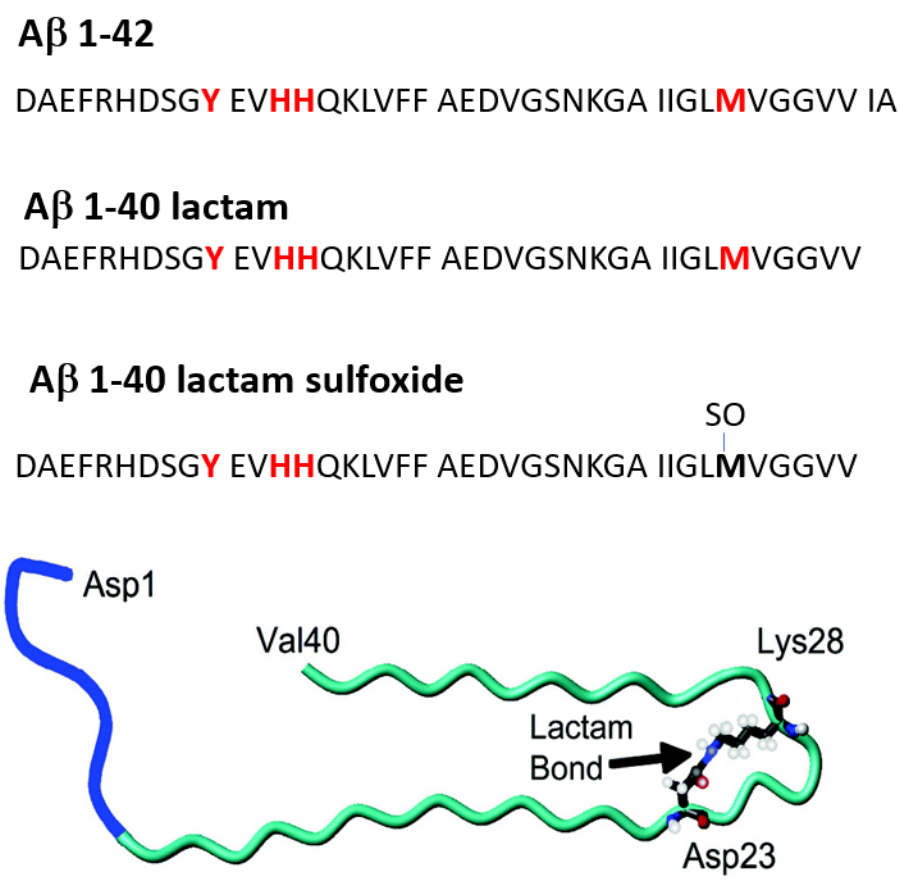

Figure 5.2. Amino acid sequence of the Aβ peptides and structural model for Aβ 1-40 lactam (D23/K28) peptide in the fibril conformation. The highlighted amino acids are susceptible of photo-oxidation. The Aβ 1-40 structural model represents the disordered N-terminal segment (blue), two β-strand segments (residues 10-22 and 30-40 in green), and the bent segment (residues 23-29) containing the lactam bond. Structural model obtained from.[194]

5.2.3. BLG

BLG protein is the major component of the whey of milk[197] and is able to form amyloid aggregates under specific incubation conditions, finding applications in very different fields. Commonly, BLG has been used in the food industry to control texturing properties, such as stabilization of foams or gelation processes,[198] but also, in biomedicine[199] as a model to study amyloid structure and fibrillation process or even for new nanotechnological applications such as hybrid materials (see *Chapter 4*).[57] BLG is a globular protein that forms dimers in physiological conditions, but modifies its structure under environmental changes of concentration, temperature, pH, or the presence of salts, forming different morphologies such as fibers,[199] multistranded ribbons,[200]

spherulites[201] or spherical particles.[202] Particularly, as the purpose of this chapter is to obtain long and isolated fibers, the conditions required consisted in incubating at low pH, in absence of salts and high temperatures. These conditions promote protein cleavage due to an acid hydrolysis reaction forming peptides that are able to interact and assemble into fibers.[203, 204] The resulted amyloid structures were considered as an interesting model candidate for photodamage experiments since features of height and periodicity provide information about the number of filaments forming the fibers (see *4.2.3. Multicolor correlative microscopy*).[171]

Importantly, the peptides involved in fiber formation contain some residues susceptible of photo-oxidation (**figure 5.3**).[180] However, it should be pointed out that variations in the fiber peptide composition have been reported depending on the fibrillation time used to form these structures (see *5.3.3. BLG fibers*).[205]

β-Lactoglobulin

LIVTQT**M**KGLDIQKVAGT**WY**SLA**M**AASDISLLDAQSAPLRV**Y**VEELKPTPEGD

LEILLQK**W**END~~ECAQKKIIAEKTKIPAVFKIDALNENKVLVLD~~TD**Y**KKYLLFC**M**E

NSAEPEQSLVCQCLVRTPEVD~~DEALEKFD~~KALKALP**MH**IRLSFNPTQLEEQC**H**I

Figure 5.3. BLG protein sequence. Amino acids that are not involved on fiber formation are strikethrough in the sequence.[203] Amino acids susceptible of photo-oxidation are highlighted in red.[180]

5.3. Materials and methods

5.3.1. Production of α-syn, ΔH1 and ΔN fibers

The plasmid containing the sequence of α-syn was provided by Dr. Begoña Sot. Protein α-syn was expressed in *E. coli* BL21 and purified as described in the literature.[184, 206] Bacteria were transformed with pT7.7 plasmid containing the protein sequence and grown in LB (Lysogeny broth medium) (Broth Miller) in the presence of ampicillin (100 mg/ml, Fisher Chemical). Protein expression was induced with IPTG (Isopropyl β-D-1-thiogalactopyranoside), cultured at 37°C for four hours and harvested by centrifugation.

The cell pellet was resuspended in 10 mM Tris–HCl (pH 8.0) (2-Amino-2-(hydroxymethyl) propane-1,3-diol, VWR), 1 mM EDTA (Ethylenediaminetetraacetic acid, Fisher BioReagents), 1 mM of protease inhibitor PMSF (phenylmethylsulfonyl fluoride), and lysed by sonication. It was centrifuged (10000 rpm, 60 min, 4 °C) in a FX6100 rotor (Beckman Coulter). The recovered supernatant was heated (20 min) at 90°C in a thermoblock (Fisher Scientific), and centrifuged at 13500 rpm 20 min 4°C in a microcentrifuge. The supernatant was collected, precipitated with 60% ammonium sulphate (PubChem) (3 h, 4 °C) and centrifuged again as before. The pellet was resuspended in 25 mM Tris–HCl (pH 8.0) and loaded onto a 5 ml HiTrap Q-Sepharose column using fast protein liquid chromatography (ÄKTAFPLC, GE Healthcare). The protein was eluted with a 0 to 600 mM NaCl (VWR, 7647-14-5) gradient and fractions containing the protein were concentrated by ultrafiltration and loaded onto a Superdex-200 16/60 chromatography column, previously equilibrated with 25 mM Tris–HCl (pH 7.5). The eluted protein was concentrated and stored at −80 °C. ΔH1 and ΔN proteins were kindly provided by Dr. Begoña Sot and were produced using a similar protocol. Protein concentrations were estimated from absorbance at 280 nm with an extinction coefficient of 5960 $M^{-1}{\cdot}cm^{-1}$ for α-syn, 4470 $M^{-1}{\cdot}cm^{-1}$ for ΔN and 5960 $M^{-1}{\cdot}cm^{-1}$ for ΔH1. Fiber formation was promoted by incubating 70 µM α-syn or 400 µM of ΔH1 and ΔN in 25 mM Tris pH 7.4, 5 mM $MgCl_2$ (AppliChem), 150 mM NaCl (AppliChem), 5 mM KCl (AppliChem,) and 0.01% SDS (Sodium dodecyl sulfate, AppliChem) at 37 ^oC and 800 rpm of shaking in a Thermoshaker (VWR, Thermal Shake lite) during 24-36h. Buffers pH was adjusted to the required values using NaOH (VWR Chemicals) or HCl (Millipore Sigma)

5.3.2. Production of Aβ fibers: Aβ 1-42, Aβ lactam 1-40 and Aβ lactam 1-40 SO

Aβ 1-42 and Aβ 1-40 lactam were kindly provided by our collaborators Prof. Kanai and Dr. Somha (University of Tokyo). Aβ 1-40 lactam SO was synthesized using solid phase peptide synthesis (SPPS) during a 5-week visit at their laboratory. The intense aggregation of Aβ peptides commonly hinders their synthesis and purification process. To circumvent this issue, the O-Acyl Isopeptide method was applied,[207, 208] which involves the use of an ester bond between Gly25 and Ser26 in acid pH as an Aβ

precursor. The O-acyl Isopeptide is then converted to Aβ via the O-to-N acyl rearrangement, under physiological conditions (**figure 5.4**).

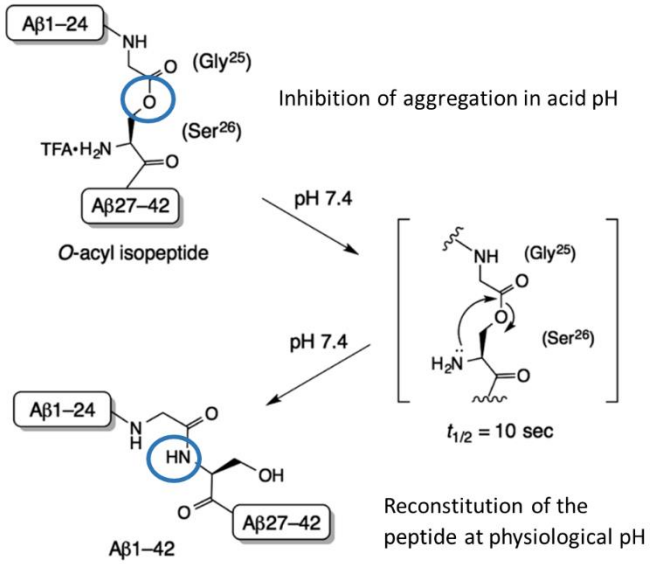

Figure 5.4. O-Acyl Isopeptide method. Aβ aggregation is inhibited by the introduction of an ester bond between Gly25 and Ser26 in acid pH. When the peptide is diluted in physiological pH occurs the O-to-N acyl rearrangement and the Aβ is reconstituted and able to aggregate. This figure was modified from.[208]

The synthesis of Aβ lactam 1-40 SO was carried out similarly to protocol described in[209] from the C-terminus to the N-terminus. SPPS was performed using amino acids coupled with different protecting groups, which are helpful to avoid undesired reactions such as fluorenylmethyloxycarbonyl (Fmoc), tert-butyloxycarbonyl (Boc), allyloxycarbonyl (aloc) and allyl. It was performed on a 0.1 mmol scale using Fmoc-Val-2-TrtA-PEG resin (tritylcarboxamidomethyl (TrtA) polyethylene glycol (PEG) resin). The resin was washed with dimethylformamide (DMF) (×5), and later the amino acid was deprotected by removing the Fmoc group using 20% piperidine/DMF (*v*/*v*) (1 min × 1 and 10 min × 1), followed by washing with DMF (×10). The peptide chains were assembled by sequential coupling of Fmoc-amino acids in DMF in the presence of *N*,*N*'-diisopropylcarbodiimide (DIC) and 1-hydroxybenzotriazole (HOBt) during 1 h at RT. This cycle was repeated for every amino acid. The added Met in position 35 contained a sulfoxide group.

For obtaining O-Acyl Isopeptide, Boc-Ser (Fmoc-Gly)-OH was added at position 26. Protecting groups were normally removed and the peptide was washed with CH_2Cl_2 (×5). After, it was subjected to coupling with the next amino acid during 3h.

For lactam bond formation, Fmoc-Lys(Aloc)-OH was introduced at position 28. When Fmoc-Asp(Allyl)-OH was introduced at position 23, the formation of the lactam bond was induced by removing the Aloc and allyl protecting groups with $Pd(PPh_3)_4$ (23.1 mg, 0.020 mmol) and $PhSiH_3$ (0.147 mL, 1.2 mmol) in CH_2Cl_2 under Argon atmosphere overnight. After washing with CH_2Cl_2 (×10) and DMF (×10), lactam formation was carried out using HATU ((1-[Bis (dimethylamino) methylene]-1H-1,2,3-triazolo[4,5-b]pyridinium 3-oxid hexafluorophosphate, Hexafluorophosphate Azabenzotriazole Tetramethyl Uronium))(190 mg, 0.500 mmol), HOAt (1-Hydroxy-7-azabenzotriazole) (13.6 mg, 0.100 mmol), and *N*-methylmorpholine (54.9 µL, 0.500 mmol) in DMF (4 mL) during 4h. After that, the elongation of the peptide chain continued until the end following the coupling and deprotection cycle previously explained.

When the Aβ peptide was synthetized, the peptide-resin was washed with MeOH (×5) and dried for 2 h in vacuum. The peptides were cleaved from the resins with TFA (trifluoroacetic acid) in the presence of triisopropylsilane and MQ water (95:2.5:2.5 [v/v]) for 90 min RT. The resin was removed through filtration, the solution was concentrated in vacuum, and precipitated with ether. The resulting precipitate was collected by filtration, dissolved with 0.1% aqueous TFA/ACN (1:1), and lyophilized for at least 12 h to obtain the crude peptide. It was purified by preparative reversed-phase HPLC (High Performance Liquid Chromatography) with 0.1% aqueous TFA/ACN (acetonitrile) system as an eluent, immediately frozen using liquid nitrogen, and lyophilized for at least 24 h. MALDI-TOF analysis show a main peak of 4329 Da as expected.

-Aβs stock preparation and fibrillization

To prepare the stock solution, Aβ amyloid peptide was dissolved in 0.1% aqueous TFA and the solution was treated with ultracentrifugation (100000 rpm) at 4 °C for 3 h on an ultracentrifuge OptimaTM TLX (Beckman Coulter, Inc., Brea, CA) with a TLA100 or

TLA120.2 rotor (Beckman Coulter, Inc.). The upper three-quarters fraction of the solution were collected. Protein concentration were estimated by absorbance at 280 nm with a molar extinction coefficient of 1490 M^{-1} cm^{-1}. The collected supernatant was diluted to obtain 200 µM stock solutions and kept at −80 °C until use.

For fiber formation, Aβ amyloid was unfrozen and buffer exchanged to 0.1 M HEPES (4-(2-hydroxyethyl)-1-piperazineethanesulfonic acid, VWR) buffer containing 0.1 M NaCl (pH 7.4). The sample was centrifuged at 8000 rpm 30 min (x2) at 4 °C using Amicon Ultra 0.5 mL filters with a 3 kDa cutoff. After, it was incubated at 37 °C, without shaking during 24 h for Aβ 1–42, 90 min for Aβ 1-40 lactam and 6 h for Aβ 1-40 lactam SO using a concentration of 40 µM.

5.3.3. Preparation of BLG fibers

Two different methods were compared for obtaining BLG fibers. In both protocols, BLG protein was purchased from Sigma-Aldrich and was dissolved in MQ pH 2. MQ water pH was lowered using HCl 1M. Protein absorbance was measured before fibrillation using an extinction coefficient of 17600 M^{-1} cm^{-1} at 280 nm.

Method 1:

A solution of 10 mg/ml of BLG was prepared. To remove non-dissolved aggregates the sample was centrifuged at 13000 rpm during 90 min in a microcentrifuge, and the supernatant was filtered (0.22 µm filter GE Healthcare). To eliminate the salts remaining from the BLG stock, the sample was washed with MQ pH2 using Amicon® Ultra 4 mL Centrifugal Filters of 10 kDa cutoff. Centrifugation was performed at 4000 rpm (Beckman coulter allegra x-15r with rotor SX4750A) during 10 min at 4^{o}C (3x times). The sample was aliquoted to ~350 µM of BLG and stored at -80^{o}C.

For fibrillation, 1 ml of the prepared BLG solution was placed on a 1.5 ml tube and incubated during 24-36 h at 90^{o}C with constant agitation of 800 rpm in a Thermoshaker (Thermal Shake lite, VWR). This protocol was modified from.[210]

Method 2:

A solution of 20 mg/ml of BLG was prepared. To completely solubilize the sample, it was agitated at 4ºC during 1h. Salts from the BLG stock were removed by dialyzing the sample for 3 days against MQ pH2 using a Spectra-Por membrane with a cutoff of 6-8 kDa. After that, 4 ml of 750 µM of BLG were placed on a glass container and stirred using a magnet at 80-90ºC during 4h. This protocol was based on.[199]

5.4. Results and discussion

5.4.1. AFM characterization of α-syn, ΔH1 and ΔN fibers

Fibers formed by α-syn, ΔH1 and ΔN were studied by AFM and TEM imaging. As shown in **figure 5.5.a** and **d**, fibers formed by α-syn are short and tend to aggregate. In contrast, mutants ΔH1 and ΔN form longer and isolated fibers becoming a valuable model for photodamage experiments (**figure 5.5. b-e** and **c-f** respectively). Differences were also appreciated between both mutants, having ΔN fibers lower heights (2-6 nm) (ΔH1 fibers 2-10 nm) and more homogeneous structures than ΔH1.

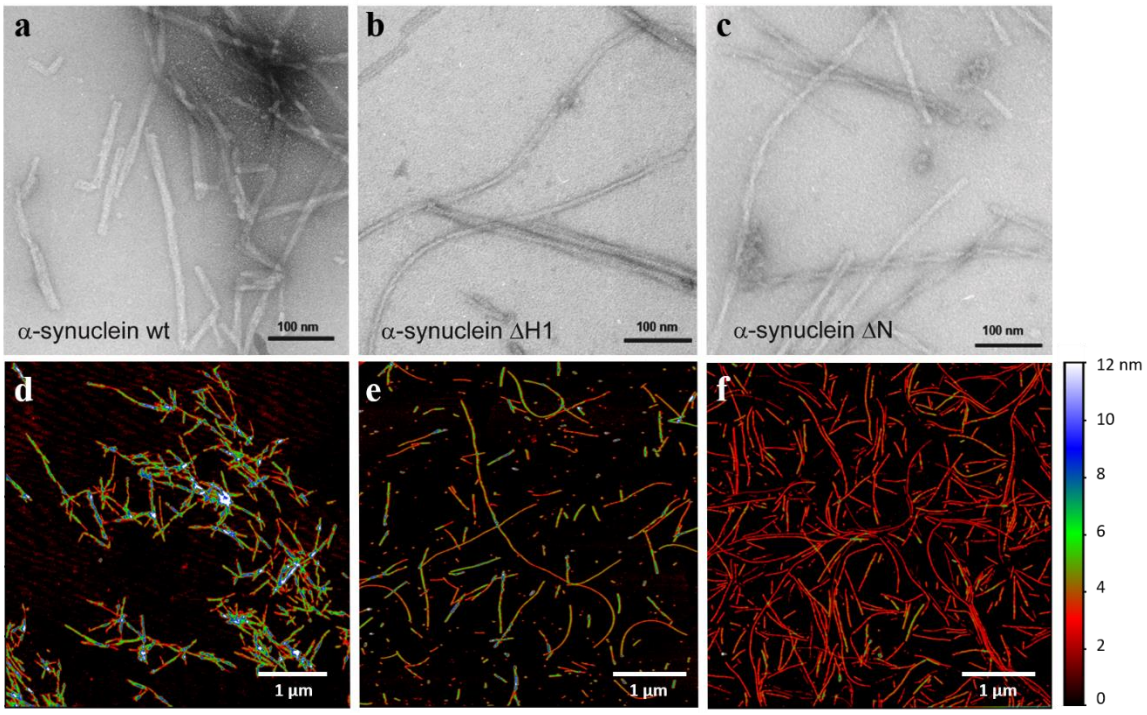

Figure 5.5. Morphological comparison of α-syn, ΔH1 and ΔN fibers by TEM (top) and AFM (bottom) imaging. a) and d) show α-syn fibers, b) and e) ΔH1 fibers and c) and f) ΔN fibers. TEM images were kindly provided by Dr. Begoña Sot. AFM samples were prepared in PBS and deposited on mica-PLL.

5.4.2. AFM characterization of Aβ1-42, Aβ 1-40 lactam and Aβ 1-40 lactam SO

The fiber morphologies obtained from the different Aβ peptides were compared by AFM imaging. **Figure 5.6.a** shows that Aβ1-42 peptide forms short fibers and heterogeneous aggregates covered with proteinaceous material. On the other hand, in **figure 5.6. b** and **c** is observed that Aβ 1-40 lactam and Aβ 1-40 lactam SO are able to form isolated and homogenous fibers with lengths from hundreds of nanometers to 1-2 µm. Therefore, Aβ 1-40 lactam and Aβ 1-40 lactam SO are potential models for photo-oxidation experiments, and Aβ1-42 was discarded.

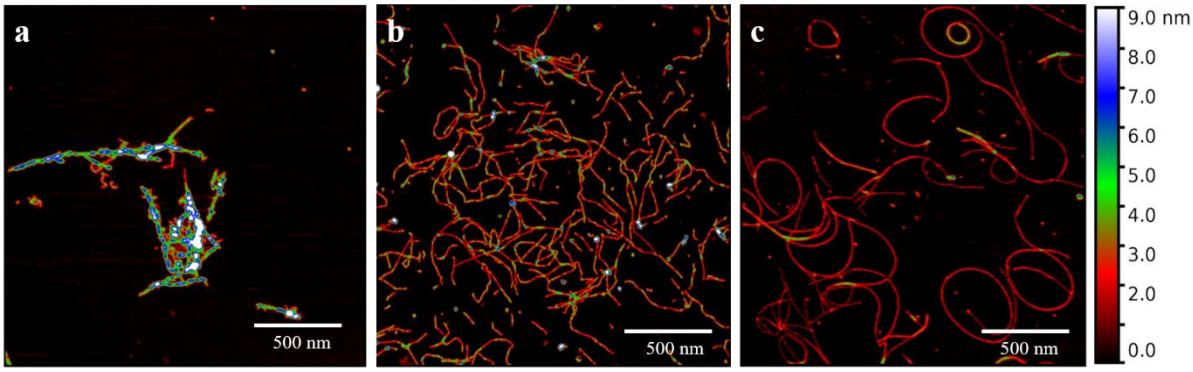

Figure 5.6. AFM characterization of Aβ peptides. a) Aβ 1-42, b) Aβ 1-40 lactam and c) Aβ 1-40 lactam SO. Fibers in 0.1 M HEPES buffer containing 0.1 M NaCl were directly deposited on mica.

5.4.3. AFM and MALDI-TOF characterization of BLG fibers

BLG fiber morphology is highly affected by the fibrillization conditions. Thus, fibers produced by two different methods were compared by AFM (**figure 5.7.a** and **b**) and MALDI-TOF MS (**figure 5.8**). AFM characterization shows very similar structures formed by long (3-10 µm) and isolated fibers that display the typical periodicity of BLG helical morphologies (also detected by TEM in **figure 5.7.c.**).[171] On the other hand, MALDI-TOF analysis provides information about the peptide composition of the fibers. **Figure 5.8** shows the MS spectra of the fragmented peptides from 2000-6500 Da for each method and the correspondent assigned amino acid sequence based in literature.[203] MS spectra show that fibers formed by method 2 contain more peptide variability than by method 1. For example, peptide 1 is only present in fibers formed by method 2. This is relevant for our subsequent studies in *Chapter 6* because peptide 1 contains two His residues,

which is a major target for photo-oxidation.[143] For this reason, fibers formed by method 2 were selected as a amyloid model for photodamage studies.

Solvent changes (pH and ionic strength) after fiber formation also produced differences in the morphology of the fibers,[211] thus fibers diluted in MQ pH2 or PBS were compared through AFM and TEM. As observed in **figure 5.7.d** and **e**, PBS produces fiber interaction, and it is no longer possible to differentiate features such as fiber periodicity. The TEM image (**figure 5.7. e**) suggests that some proteinaceous material is covering the fibers. Therefore, MQ at pH 2 was selected as a solvent for BLG photodamage experiments.

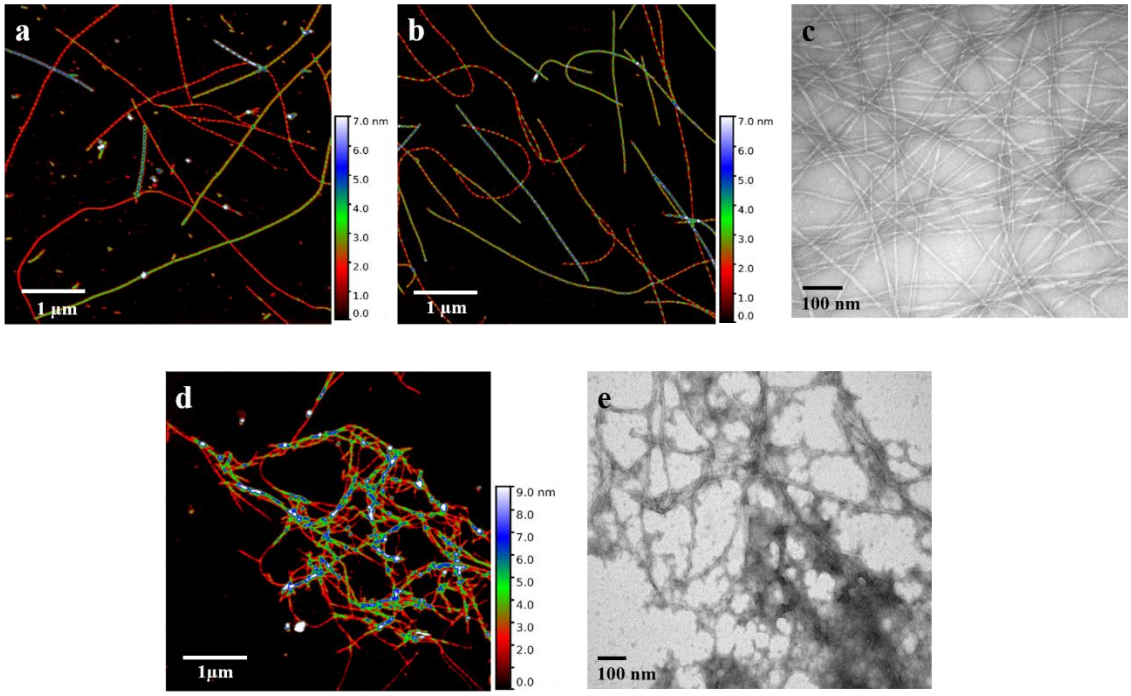

Figure 5.7. Comparison of different BLG fiber conditions. Images a) and b) show AFM measurements of BLG in pH2 in mica produced by method 1 or method 2 respectively. In c) BLG fibers in pH2 were imaged by TEM. d) shows AFM images of BLG fibers diluted in PBS on a mica-PLL substrate and the same sample imaged by TEM (e).

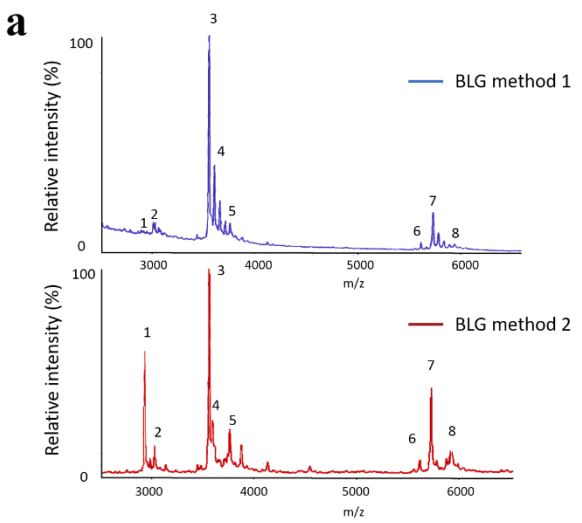

Peak	Sequence	m/z
1	KALKALPMHIRLSFNPTQLEEQCHI	2917.7
2	LIVTQTMKGLDIQKVAGTWYSLAMAASD	3011,5
3	LIVTQTMKGLDIQKVAGTWYSLAMAASDISLLD	3552.9
4	(D)YKKYLLFCMENSAEPEQSLACQCLVRTPEV(D)	3607.2
5	TDYKKYLLFCMENSAEPEQSLVCQCLVRTPEV	3733.0+ 23 (Na+)=3756
6	LIVTQTMKGLDIQKVAGTWYSLAMAASDISLLDAQSAPLRVYVEELKPTPEG	5622
7	LIVTQTMKGLDIQKVAGTWYSLAMAASDISLLDAQSAPLRVYVEELKPTPEGD	5737
8	(D)IQKVAGTWYSLAMAASDISLLDAQSAPLRVYVEELKPTPEGDLEILLQKWEN(D)	5921

Figure 5.8. MALDI-TOF MS comparison of fibers obtained by method 1 and 2. a) MALDI-TOF spectra of BLG peptides. Numbered peaks are assigned to a peptide fragment in table b).

5.5. Conclusion

Different amyloid morphologies were explored by AFM and TEM imaging with the purpose of selecting the most suitable model to study photodamage. Long and isolated structures were successfully obtained with ΔH1 and ΔN mutants of α-syn, Aβ 1-40 lactam, Aβ 1-40 lactam SO and BLG fibers diluted in MQ pH2. For the next chapter, BLG was chosen as a first model for photodamage experiments for its structure, the presence of amino acids susceptible to oxidation, and simplicity of fiber preparation.

Chapter 6

Light-induced damage in amyloid fibers: from bulk to single fiber characterization

6. Light-induced damage in amyloid fibers: from bulk to single fiber characterization

Adapted from:

Bondia, P., Torra, J., Tone, C., Sawazaki, T., del Valle, A., Sot, B., Nonell, S., Kanai, M., Sohma, Y. and Flors, C. A nanoscale view of amyloid photodynamic damage (in preparation).

6.1. Introduction

The misfolding and aggregation of proteins into amyloid fibers is generally toxic and is involved in many different disorders. Recently, photochemical tools based on ROS photosensitizers or photocatalysts to disrupt amyloid aggregates have been developed.[138-141] Since peptide and protein aggregation is generally driven by intermolecular hydrophobic interactions, the working hypothesis is that oxygenation renders the monomer and/or early aggregate seeds more hydrophilic and stable in their hydrated state, and disrupts the aggregates in non-toxic and non-amyloid prone forms.[212-218] A promising strategy relies in the use of switchable photocatalysts, which stand out for their selectivity recognizing cross-β-sheet structures and only producing singlet oxygen when bound, reducing the damage of off-target molecules (**figure 1.6**).[143] Several families of compounds have been developed so far with structural modifications that include the introduction of a heavy atom to enhance intersystem crossing to the triplet state and singlet oxygen formation, improved solubilization and red-shifting of their absorption spectra by tuning electron donor and acceptor capabilities.[142-144] In all cases, the mechanism for selective photo-oxidation involves the enhancement of the excited-state lifetime, and in turn improved singlet oxygen production, upon binding to cross-β-sheet structures due to rotational restriction of the bond between electron donor and acceptor (**figure 6.1.b**).

While switchable photocatalysts are promising as potential phototherapeutic compounds for amyloid-related diseases, preliminary experiments in cells and mice suggest that there is scope to improve the efficiency of photo-oxygenation as well as their selectivity to aggregates.[142, 144] By using a combination of biochemical techniques and nanoscale imaging methods, this chapter addresses several issues related to the

interaction between photocatalyst and amyloids and shows that photo-oxygenation at the molecular level leads to dramatic changes that can be visualized at the nanoscale by AFM. Although the methodology reported here is generally applicable to any (switchable) photocatalyst, for these experiments a ThT derivative (ROS-ThT, **figure 6.1.a**) is used, which in addition to fluorescence produces ROS and has been shown to selectively photo-oxygenate a range of amyloid proteins upon blue light irradiation.[143] As model amyloid system, BLG fibers were selected since their topography potentially favors the observation of rupture events in AFM experiments (see *Chapter 5*).

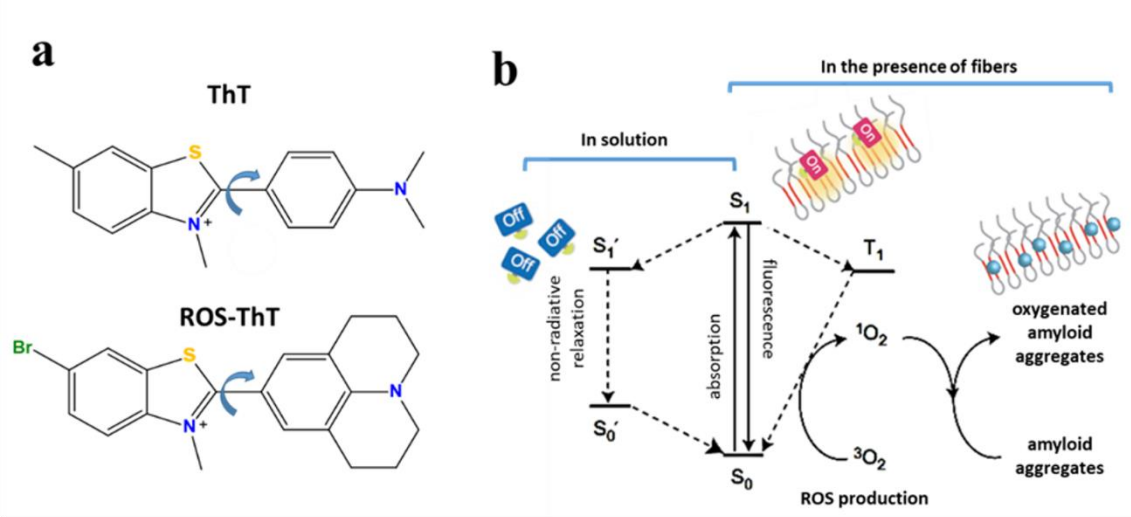

Figure 6.1. Molecular structure of ThT and ROS-ThT (a) and Jablonski diagram (b). The latter shows that when ROS-ThT is excited, different relaxation pathways are plausible. If it is bound to the amyloid fibers it would produce either fluorescence or ROS species and if it is in solution it would deactivate to the ground state by the free rotation of the molecule. Figure modified from.[143]

6.2. Materials and methods

6.2.1. Dyes

ThT was purchased from Sigma-Aldrich, dissolved in MQ at a concentration of 8 mM and stored at -20 ºC. Before experiments, ThT was thawed and diluted to 20 µM in MQ. Once the stock was thawed it was kept in the fridge during short periods of time (~1 week). ROS-ThT was synthesized as previously described by the group of Prof. Motomu Kanai.[143] The solid compound was stored at -20 ºC, and a few mg were dissolved in the experimental solvent just before measurements. Concentration of ThT and ROS-ThT

solutions was determined by absorbance using extinction coefficients of 23800 $M^{-1}\cdot cm^{-1}$ at 412 nm[219] and 23500 $M^{-1}\cdot cm^{-1}$ at 456 nm, respectively.

6.2.2. Bulk irradiation experiments: MALDI-TOF, CD and AFM

BLG fibers were filtered to avoid the signal contribution from the monomer or free peptides in bulk experiments (see *2.7.2. Fiber purification for bulk experiments*) and diluted in D_2O. ROS-ThT was added to an aliquot of the BLG dilution. Part of the sample was deposited on a well in a 96 multiwell plate (Sigma-Aldrich) and irradiated during 1 h using a LED (Thorlabs, M420L2) of 420 nm at 70 mW/cm^2, and other part was kept in the dark. An aliquot of BLG fibers was irradiated in the same conditions but without ROS-ThT. Each condition was measured by MALDI-TOF MS, CD and AFM as described in *Chapter 2*.

6.2.3. Nanoscale photodamage experiments

For the nanoscale photodamage irradiation experiments, BLG fibers in MQ pH2 were deposited on mica and measured by AFM obtaining a reference image. The surface was covered by ROS-ThT in MQ at pH 2 and incubated in the dark for 5 minutes before irradiation with a 420 nm LED at 70 mW/cm^2 for 15 min. After the sample was dried, AFM imaging of the previously measured area was performed again. As a control, the same experiment was repeated using ThT instead of ROS-ThT, in absence of ROS-ThT and incubating the sample in the presence of the photocatalyst for 15 min in dark.

6.3. Results and discussion

6.3.1. Absorption and fluorescence spectroscopy

The absorption spectra of ThT and ROS-ThT at the same concentration (20 μM) are shown, with maximum peaks at 412 nm and 456 nm, respectively (**figure 6.2.a**). In the presence of fibers an increase of absorbance was observed for ThT but not for ROS-ThT, which is in agreement with previously reported absorption spectra.[143] Both spectra intersect at 435 nm, which was used as excitation wavelength in fluorescence

spectroscopy experiments (**figure 6.2.b**), so that fluorescence intensity of both molecules in the presence of BLG fibers can be compared.

Fluorescence enhancement of ThT[220, 221] and ROS-ThT[143] is produced when biding to the cross-β-sheet motif characteristic of amyloid structures. ROS-ThT recognition of the cross β-sheet motif has been previously observed for other amyloid aggregates, such as Aβ and α-syn, and it is confirmed here for BLG fibers (**figure 6.2.b**). As expected, very low fluorescence signal was detected in the presence of BLG monomer since the native protein is not recognized by the photocatalyst (**figure 6.2.b**). Previous studies indicate that amyloid affinity of ROS-ThT is higher than of ThT,[143] which should enhance the ROS-ThT signal. In contrast, when compared fluorescence intensity of ThT and ROS-ThT in the presence of BLG fibers, fluorescence is lower in the latter. This result is consistent with the presence of an alternative relaxation pathway (i.e. triplet state and ROS production) (**figure 6.1.b**).

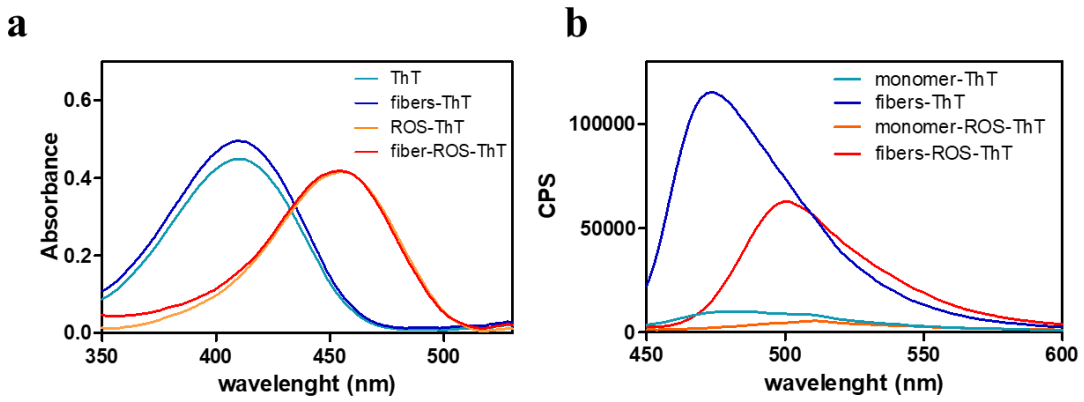

Figure 6.2. Absorption (a) and fluorescence (b) spectra of ThT and ROS-ThT with BLG fibers. Spectra were measured from a solution of 20 µM of ThT or of ROS-ThT in absence and presence of 60 µM of BLG fibers in MQ pH2. Fluorescence spectra were also performed in the presence BLG monomer showing no signal increase. Samples were excited at 435 nm.

6.3.2. ROS-ThT binding at the single-fiber level: correlative AFM and fluorescence microscopy

In our group, fluorescence decay kinetics of ROS-ThT was studied in bulk samples by time-resolved fluorescence spectroscopy, showing at least two binding modes contributing to the signal decay,[222] similarly to previously observed for ThT.[219, 221, 223-225]

Given the binding complexity as well as the heterogeneity of the amyloid aggregate population, correlative fluorescence microscopy and AFM was performed to study fluorescence enhancement of ROS-ThT at the single-fiber level.

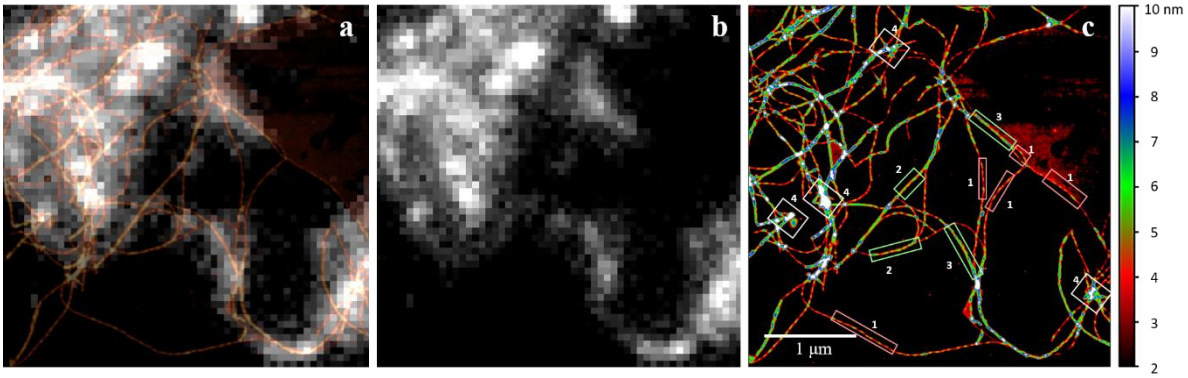

Figure 6.3. Correlative AFM and fluorescence microscopy of BLG fibers labelled with ROS-ThT. a) overlaid images; b) fluorescence image; c) AFM image. Boxes labelled 1-4 correspond to fibers of different thickness and fluorescent behaviour (see text). For these images 20 µl of ~30 nM of filtered BLG fibers labelled with 30 nM of ROS-ThT in MQ were dried on a glass coverslip. Fluorescence imaging was performed using a 488 nm laser with an intensity of 46 W/cm^2.

The overlaid fluorescence and AFM image in **figure 6.3.a** shows heterogeneous staining of BLG fibers by ROS-ThT, as observed in similar systems.[63, 226, 227] A deeper analysis of the high resolution AFM image suggests a morphology-dependent binding, or fluorescence enhancement, of ROS-ThT to BLG (**figure 6.3.c**). The thinnest BLG fibers, which correspond to boxes labeled as "1", are non-fluorescent, while thicker fibers and fiber aggregates (labeled as "4") can be readily observed in the fluorescence image. An intermediate situation occurs in intermediate-height fibers, which are emissive in some cases (labeled as "3"), and non-emissive in others ("2").

The binding mechanism of ThT to amyloids is complex and controversial[219-221, 224] although it is thought to involve at least a tight binding mode that forces a highly fluorescent ThT geometry via hydrophobic interactions, and a main and weaker electrostatic binding mode with a low fluorescence yield.[223] Our finding that more ROS-ThT fluorescence can be observed in thicker, more intertwined, fibers (type "4") could be explained, at least partially, by a recent report that highlights the importance of hydrophobic pockets located at the junction between protofilaments in the binding of

ThT.[228] Specifically for heat-denatured BLG, whose aggregates are formed by different peptides after fragmentation of the full-length protein, it has been shown that subtle differences in structure and/or composition lead to different ThT staining.[204] While it is not possible to clearly distinguish fibers "2" and "3" from the AFM topography in **figure 6.3**, the correlative fluorescence data does show differential ThT fluorescence, suggesting that they are formed by different types of BLG peptide fragments and/or morphologies. These experiments highlight that studies at the single-fiber level using correlative AFM and fluorescence microscopy are a useful tool to probe the heterogeneity of amyloid material and to disentangle the complex dependence between fluorophore binding and fiber morphology and/or composition.[57]

6.3.3. Photo-oxidation of amyloid fibers using bulk techniques: MALDI-TOF and CD

Classical biochemical techniques such as MALDI-TOF MS and CD are commonly used to characterize global photo-oxidation effects,[143, 229] and we applied these techniques to further characterize photo-oxidation of BLG fibers by ROS-ThT. For these experiments D_2O was used as a solvent since it enhances singlet oxygen lifetime compared to H_2O,[230] a strategy to increase the observed oxidation effects.

Previous studies using MALDI-TOF have identified the effects of singlet oxygen photosensitized by ThT derivatives on residues of Aβ1-42 that are particularly susceptible to photo-oxidation.[143, 229] We have performed similar studies on BLG that confirm photo-oxidation of several residues (**figure 6.4**). MS spectra were recorded from 2000 Da to 20000 Da since a BLG monomer is 18400 Da, but most of the peaks were found under 9000 Da, corresponding with the different fragmented peptides forming the fibers. The amino acid sequences were assigned to the detected MS peaks based on previous literature.[203] Photo-oxidation was observed as an increase of 16 Da resulted from oxygen addition to the peptide and it was only detected in the mass range shown in **figure 6.4**. BLG (**a**) and BLG irradiated in the presence of ROS-ThT (**d**) are compared, and oxygenation was detected in at least two peptides labeled as "1" and "2", with a clear change in the shape of the peaks. To further resolve the mass of oxygenated peptides, MS was also recorded using a DHAP matrix, which provides better resolution

in this mass range (see red inset in **figure 6.4.d**). In this spectrum up to five oxidations were detected for peptide 1 and four for peptide 2. MS experiments using this photocatalyst on other amyloid aggregates show that His residues are the major oxidation site, as well as Met residues to a minor extend.[143] Peptides corresponding to peaks 1 and 2 in **figure 6.4.a** indeed contain these amino acids, and therefore are the most probable target of the detected oxygenation. For peptide 1, the observed oxidations are consistent with the addition of two oxygens to each His residue and one to Met. [231] Peptide 2 shows up to 4 oxygenation sites that likely corresponds to amino acids susceptible to oxidation such as Met, Tyr or Trp .[180, 231]

AFM imaging was performed on the same samples analyzed by MALDI-TOF. Interestingly, after irradiating in the presence of ROS-ThT lower concentration of fibers was found, which is consistent with part of the fibers being disaggregated due to oxidation. Moreover, controls in which fibers were irradiated in absence of ROS-ThT or not irradiated in the presence of ROS-ThT were performed and neither oxygenation nor AFM fibers changes were detected (**figure 6.4.b** and **c**).

Previous literature has reported that amyloid photo-oxidation affects the secondary structure of the amyloid aggregates reducing the β-sheet content.[140, 232] Therefore, CD was performed to evaluate the effect of photo-oxidation due to ROS-ThT over the secondary structure of BLG fibers. **Figure 6.4.e** shows the CD spectra of BLG fibers, which exhibit negative peak at 218 nm typical from a β-sheet-rich secondary structure. When BLG fibers were irradiated in the presence of ROS-ThT an decrease in the signal at 218 nm is detected, which suggests that the oxidation of the protein is inducing changes in the BLG fiber secondary structure.

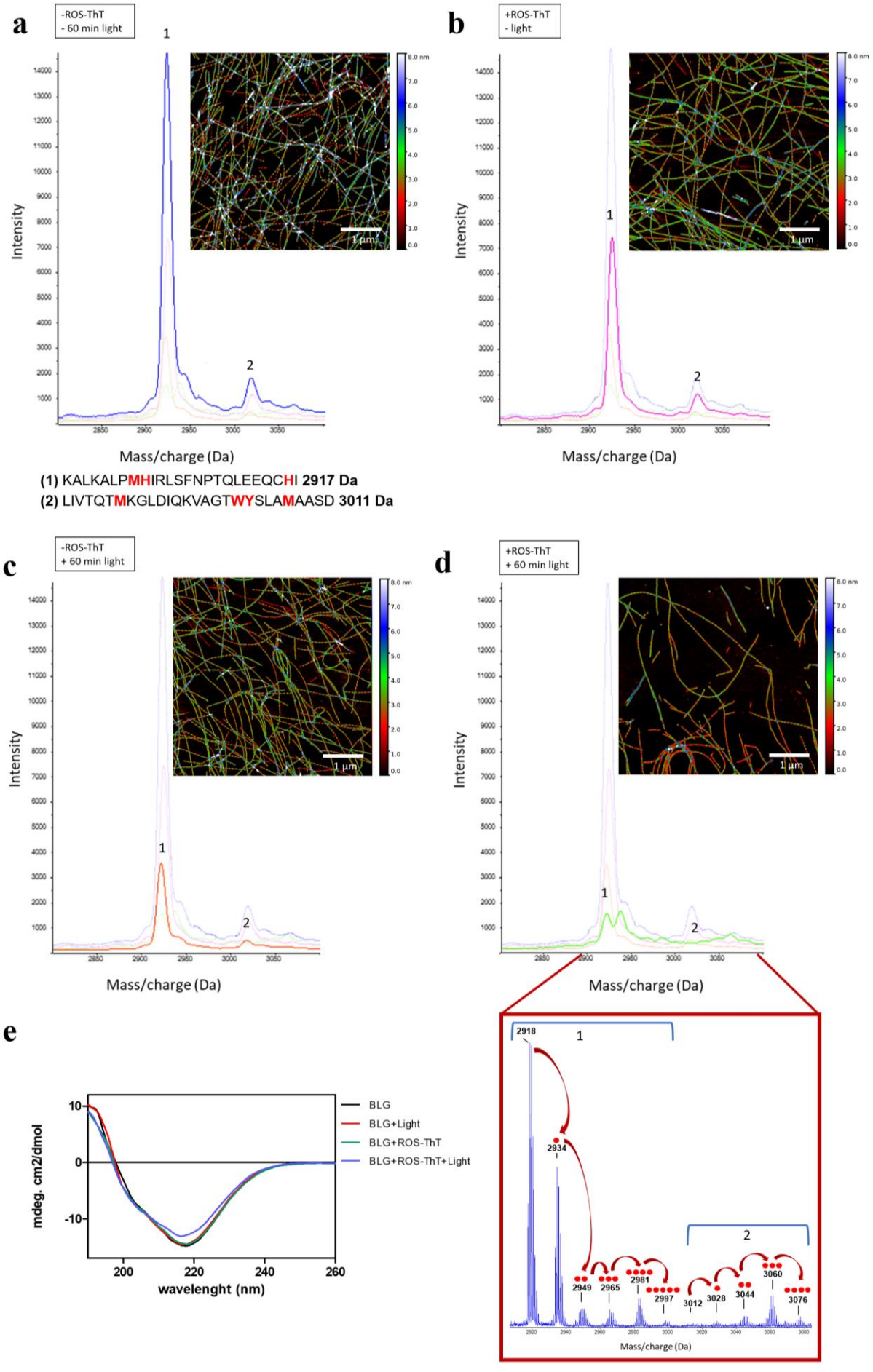
a
-ROS-ThT
- 60 min light
b
+ROS-ThT
- light
Intensity
Mass/charge (Da)
1 µm
(1) KALKALPMHIRLSFNPTQLEEQCHI 2917 Da
(2) LIVTQTMKGLDIQKVAGTWYSLAMAASD 3011 Da
c
-ROS-ThT
+ 60 min light
d
+ROS-ThT
+ 60 min light
e
mdeg. cm2/dmol
wavelenght (nm)
BLG
BLG+Light
BLG+ROS-ThT
BLG+ROS-ThT+Light
2918
2934
2949
2965
2981
2997
3012
3028
3044
3060
3076

Figure 6.4. Bulk analysis of BLG fibers photo-oxidation produced by ROS-ThT. Images a-d show MALDI-TOF spectra in SPA matrix of 60 μM BLG fibers diluted in D_2O using different conditions and the AFM image of the same. a) BLG fibers. The peptide sequences assigned to the peaks 1 and 2 are indicated on the top-right with the amino acids most susceptible to oxidation highlighted in red. b) BLG fibers after 1h of irradiation (420 nm LED and 70 mW/cm^2), c) BLG with ROS-ThT (20 μM) incubated in dark and d) BLG with 20 μM ROS-ThT and 1h irradiation. The red inset shows a MALDI-TOF spectrum using a DHAP matrix to obtain higher resolution of peak 1 and 2. Red dots indicate the number of oxidation sites of the peak. e) shows the CD spectra of the same samples.

6.3.4. Nanoscale imaging of amyloid photodynamic damage

Singlet oxygen-mediated damage to susceptible residues is known to propagate by radical processes to neighboring sites, potentially leading to aggregate disassembly, or even protein fragmentation.[233] Therefore, AFM was applied to ascertain if photo-oxidation by singlet oxygen at the molecular level would bring about nanoscale morphological changes that could be imaged at the single-fiber level.

While AFM has been routinely used to visualize photosensitized inhibition of amyloid aggregation from bulk samples, here the same sample area is compared before and after irradiation in order to observe potential changes at the single-fiber level (see *6.2.3. Nanoscale photodamage experiments*). **Figures 6.5.a** and **b** show high-resolution AFM topography images of BLG fibers before and after irradiation in the presence of ROS-ThT on mica. Several fiber rupture events can be clearly observed after irradiation. Control experiments were also performed, in which the sample was subjected to the same preparation procedure (incubation time, washing, etc.) but ThT was used instead of ROS-ThT (**figure 6.5.c** and **d**), with no irradiation (**figure 6.5.e** and **f**), or without ROS-ThT (**figures 6.5.g** and **h**), showing no observable changes.

Interestingly, rupture occurred mostly in BLG fibers above a certain size (about 4-5 nm at their peak, green arrows in **figure 6.5. b**), although, not in every fiber (yellow arrows). Less damage could be observed in the thinnest fibers (red arrows). This is consistent with the weaker interaction of ROS-ThT with the latter, as revealed from correlative fluorescence/AFM images in **figure 6.3** and discussed above. While the absolute values of fiber heights cannot be directly compared between experiments on

glass (**figure 6.3**) and mica (**figure 6.5**) due to their different surface roughness, there is a clear trend that suggests that ROS-ThT has stronger binding, and in turn photo-catalytic activity, on thicker BLG aggregates.

As explained in *Chapter 5*, by AFM it is possible to observe fiber periodicity typical of BLG helical conformation. Height and periodicity patterns allow as to distinguish different fiber polymorphism. If similar height fiber are compared, in some of them the periodicity it is not clearly distinguished (green arrows). Intriguingly, fibers with clear periodicity (yellow arrows) seem to be more resilient to photodamage, as judged by comparing **figures 6.5.a** and **b**. This could be explained by a difference in binding of ROS-ThT, as observed in **figure 6.3** for intermediate-height fibers.

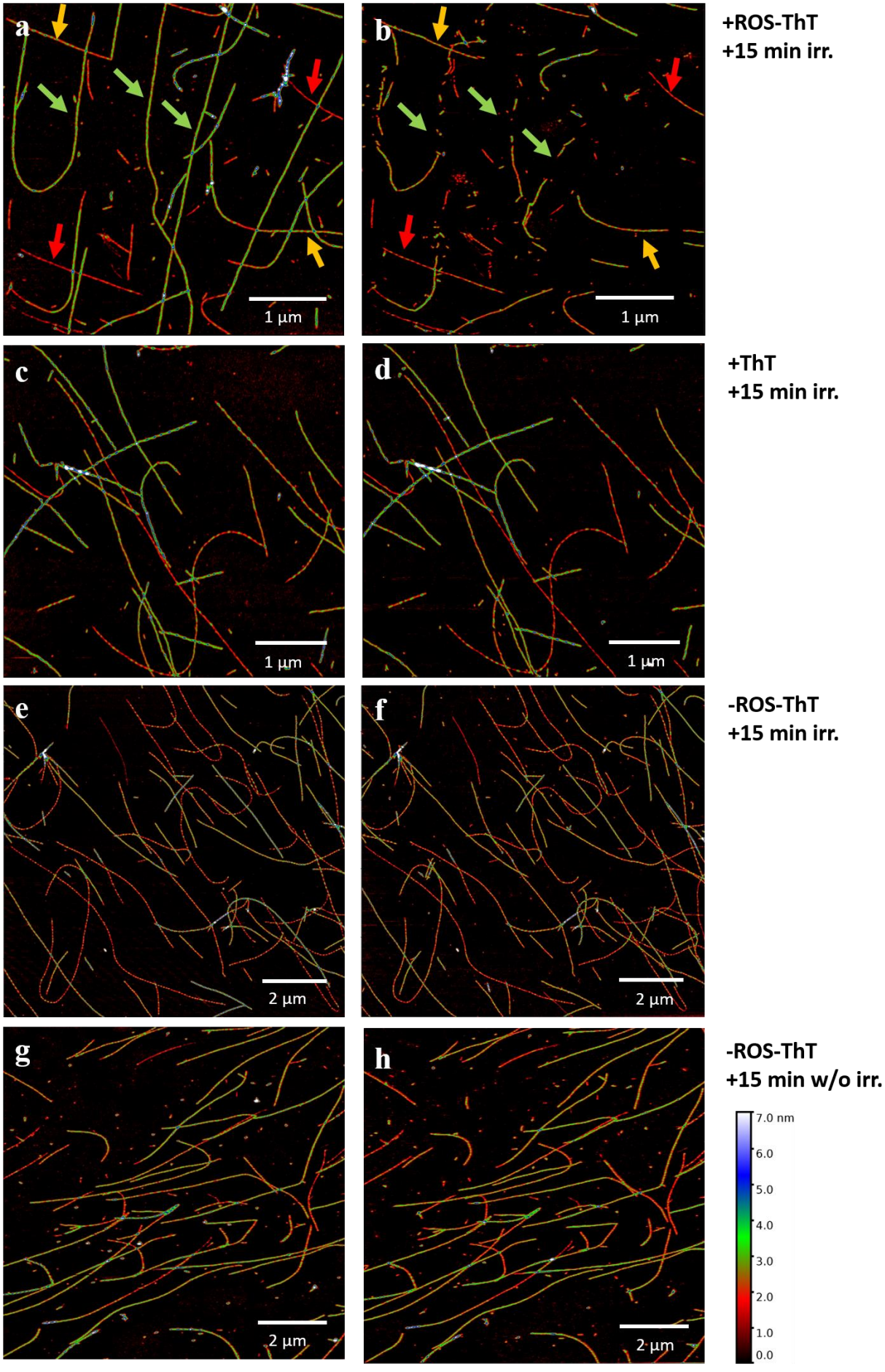
a
b
+ROS-ThT
+15 min irr.
1 µm
1 µm
c
d
+ThT
+15 min irr.
1 µm
1 µm
e
f
-ROS-ThT
+15 min irr.
2 µm
2 µm
g
h
-ROS-ThT
+15 min w/o irr.
2 µm
2 µm
7.0 nm
6.0
5.0
4.0
3.0
2.0
1.0
0.0

Figure 6.5. Nanoscale imaging of BLG fibers photodamage produced by ROS-ThT. AFM topographic images before (a) and after (b) irradiation (LED 420 nm, 15 min, 70 mW/cm^2) of BLG fibers in the presence of ROS-ThT 20 μM. Green arrows point to examples of rupture events and yellow arrows mark similar peak height but non-damaged. Same experiment before (c) and after (d) irradiation was performed using ThT. Control experiment before (e) and after (f) irradiation with no ROS-ThT. Control before (g) and after incubation with ROS-ThT for 15 min in dark (h).

Recently, in our group this methodology has been extended to other fibers such as α-syn mutants ΔH1 and ΔN proving to be a useful methodology to study different systems.[222] Interestingly, differential behavior was observed, ΔH1 was completely broken while ΔN was resistant to photodamage. This mutant lacks His50, which is an important target of oxidation suggesting breakage sequence dependence. In a near future, Aβ 1-40 and Aβ 1-40 SO are also going to be tested in order to address how fibers formed with the SO modification are affected by photodamage in comparison with the non-modified variant. Additionally, more specific and efficient photocatalysts with lower cell cytotoxic are being developed and nanoscale imaging of photodamage on amyloid fibers is expected to contribute to evaluate these new photocatalysis as part of the development process before *in vivo* studies.

6.4. Conclusion

A combination of bulk and advanced nanoscale imaging techniques has been used to study the complex binding to amyloids of a switchable photocatalyst (ROS-ThT), as well as its consequences upon irradiation. Bulk studies show that photodamage produces oxygenation of the amyloid fibers and, consequently, its β-sheet content is reduced and part of the fibers are disaggregated. Moreover, heterogeneity in ROS-ThT binding and breakage was detected by single-fiber imaging. Correlative AFM and fluorescence microscopy reveal topography-dependent binding of the dye to BLG fibers, which may also explain the difference in its response to photodamage, as assessed by AFM with *in situ* irradiation. Overall, our results help to unravel some of the complexity associated to highly heterogeneous populations and contribute to the development of improved phototherapeutics strategies for amyloid-related disorders.

Chapter 7

General discussion and outlook

7. General discussion and outlook

This thesis is focused on the application of imaging techniques and their correlative combination for the characterization of amyloid aggregates with interest in new materials and biomedicine research. The benefit of combining imaging techniques to achieve a more complete picture of the system is emphasized, obtaining complementary information about different features of the same sample. Additionally, correlative AFM and fluorescence microscopy was combined with bulk techniques to obtain a deeper understanding of the samples. The purpose of this chapter is to shortly discuss the current limitations, alternative experiments and future perspectives of the presented results.

7.1. Advanced correlative and single-fiber microscopy methods

During this thesis, correlative microscopy was successfully applied to analyze amyloid fibers in the context of new materials research and nanomedicine. These studies are an example of how combined techniques provide a better understanding of the sample, which cannot be obtained using the same techniques in an independent manner. Moreover, AFM topographical imaging in combination with SMLM was shown to be a helpful tool to learn about labelling quality and avoid analysis artefacts, proving to be a suitable strategy to validate SMLM methods. Alternatively, AFM could be adapted to perform different measurements providing another view of the sample such as peak-force maps for studying nanomechanical properties of different amyloids, polymorphisms or species formed along the fibrilization pathway.[234-236] Other valuable information for new materials research that could be obtained is surface potential[237] or magnetic maps.[34, 238]

Correlative microscopy has been also applied for studying ROS-ThT binding to amyloid fibers, but in this case, fluorescence imaging was limited by diffraction and the resolution gap is limiting the correlation of specific fluorescence signal locations with individual topographical features. While the fluorescent properties of ROS-ThT are not ideal for super-resolution fluorescence microscopy, imaging of ROS-ThT by SMLM and other techniques is being explored in the group, similarly to previously obtained SMLM

using ThT.[239, 240] While fluorescence imaging of BLG is challenging due to low fluorescence signal, other amyloid fibers, such as α-syn or its mutants ΔN or ΔH1, which show higher fluorescence are more promising, and preliminary SMLM images have been obtained (**figure 7.1**). The final goal of this study is to achieve correlative AFM and SMLM in combination with nanoscale photodamage experiments to analyze in depth the relationship between topography, photocatalyst binding and photodamage. On the other hand, these studies are focusing in one part of the picture, but other factors could be involved in ROS-ThT amyloid binding, and different single-fiber studies can provide helpful complementary information. For example, it would be interesting to use AFM for measuring the surface potential of amyloid fibers, which is critically dependent on its structural conformation[241] and some studies consider charge an important factor in some binding modes of ThT to the fibers.[219, 225] Other interesting experiment is using tip-enhanced Raman spectroscopy (TERS). In reported experiments,[242] heterogeneity on the BLG fibers surface β-sheet content was detected within the same fiber and in comparison with different fiber morphologies. Also, the compared structures display distinct amino acids at the surface. These heterogeneities that are not detected by AFM-fluorescence microscopy may explain that similar structures on AFM shown differential ROS-ThT binding and/or breakage.

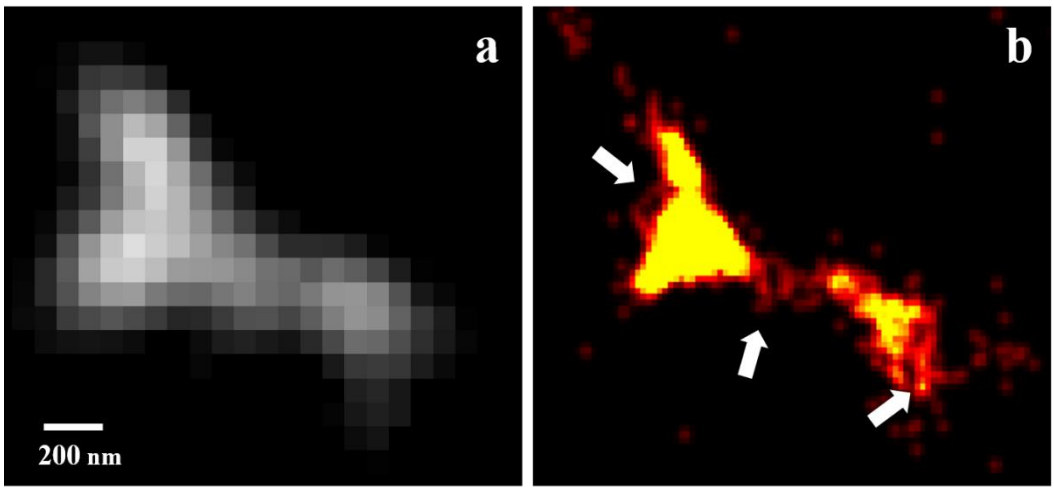

Figure 7.1. SMLM of ROS-ThT bound to α-syn amyloid aggregates. Imaging is performed on PLL glass coverslip using 60 µM of ROS-ThT in switching buffer (*see 3.2.2. SMLM imaging*). a) Standard fluorescence imaging. b) SMLM, white arrows point to structural details hidden in the diffraction limited image (a).

Although the thesis has focused on the combination of AFM with (super-resolution) fluoresce microscopy, during last years a wide variety of correlative systems are being developed extending our possibilities to perform multiparametric analysis on complex systems. For example, (super-resolution) fluorescence microscopy can be combined with different spectroscopic techniques for obtaining additional chemical information,[45] such as Fourier transform infrared (FTIR), which reveals the chemistry of an entire sample[243] or with MS systems, like imaging secondary ion mass spectrometry (SIMS), for mass-based identification of isotopes or molecules.[244] Alternatively, other high-resolution imaging techniques such as an EM or AFM can be combined with another instrument that provides information about the chemical composition of the sample, like MS systems[245-248] or an attached confocal Raman microscope[249], which can additionally be combined with an energy dispersive X-ray spectroscopy (EDXS) enabling elemental analysis.[250] AFM can be also used for obtaining nanomechanical information and its combination with infrared nanospectroscopy provides structural information, which is valuable for studying molecular changes in amyloid during the aggregation pathway [235, 236].

Apart from correlative techniques, the application of different single-molecule methods is broadening our understanding of amyloid structures by providing a view of individual events commonly hidden under bulk approaches. For example, AFM, in its force spectroscopy mode, is used to compare the mechanical stability of different IDPs in the monomeric form. It shows correlation between the propensity to develop a neurodegenerative disease and conformational polymorphism, in which some of the detected species present high mechanical resistance and are suggested as the amyloid aggregation precursors. Also, a reduction in the high mechanical resistant structures in the presence of an amyloid inhibitor has been observed.[251] A recently developed technique for single-molecule studies is the thermophoretic trap, which is promising for amyloid studies since it allows the observation of single fibril growth or fibril breakage in solution. Therefore, no immobilization is required reducing possible interferences on the protein structures.[252] The integration of the information provided by the different strategies is critical for elucidating mechanism formation steps, the events that drives

the change of a native functional protein to an aggregation-prone specie or what determines amyloid toxicity. [107, 253]

7.2. Studying the complexity of amyloid in biomedicine and materials

Amyloid fibers are formed by the β-sheet motif, which can be assembled into a variety of polymorphic structures adding complexity to these systems. To molecularly understand the implications of this morphological diversity, resolving the atomic structures of the fibers is required.[254] In the case of BLG fibers, the atomic structure is not solved but it would provide valuable information to interpret the results obtained during this thesis. For BLG fibers application as new material (explained in *Chapter 4*), it may explain the heterogeneous labelling observed at the nanoscale as a dependence of the surface amino acid exposure. Furthermore, it may help to clarify the interaction of these fibers with other molecules such as ThT and ROS-ThT. In fibers formed by Aβ 1-40, the molecular structure has shown different morphologies and structural dependent binding of ThT has been predicted,[228] thus, polymorphism may explain the heterogeneous binding of ROS-ThT to BLG fibers.

The complexity of amyloid structures is challenging our capabilities to treat amyloid related diseases, and phototherapy has risen as an alternative to commonly used therapies. AFM nanoscale photodamage characterization tries to provide another tool to evaluate the effects of photocatalyst at the single-fiber level to analyze differential response of individual fibers, as part of the photocatalyst development process. Particularly, ROS-ThT produces ROS and fluorescence, which has been useful for analyzing photocatalyst binding at the single-fiber level (*see Chapter 6*) and is valuable for theranostic applications (combination of therapeutic drugs and diagnostic imaging agents).[255] Unfortunately, ROS-ThT has been tested in cells and proved to be toxic.[143] Other promising photocatalyst have been developed by our collaborators[142] that have shown to reduce the amount of amyloid aggregates *in vivo*. However, improved compounds with higher oxygenation yield are needed.[144] Thus, new photosensitizers are being synthetized and feedback from advanced nanoscopy should offer a roadmap for developing an optimal catalyst.

An important limitation of phototherapy is that light irradiation in the brain is required for the treatment of neurological diseases with photocatalysis, which implies surgical procedures. A possible solution may come hand-in-hand with optogenetics developments such as brain injectable optoelectronics.[143, 256] Alternatively, photocatalysts may be suitable for treating peripheral amyloid diseases. Moreover, it has been suggested that there in a flux between the brain aggregates and peripheral areas,[257] or even that some amyloid aggregates are generated at peripheral areas and propagate into the brain.[258, 259] This implies that deficits in the amyloid clearance of the peripheral system might also contribute to neurological diseases becoming a therapeutic target.[257] Consequently, the traditionally monotherapies based on the concept “one target, one treatment” ignores the complexity of amyloid diseases and might be more effective combining brain and peripheral treatments.[260]

To sum up, strategies that study amyloid aggregates from an individual fiber perspective are key to understand its heterogeneity and implications of its diverse polymorphism. These strategies are required for unravelling the mechanism of its formation, its phenotypical effect in diseases or new treatment approaches. Furthermore, a deep understanding of these enigmatic structures will allow us to develop innovative applications in diverse fields such as materials research.

General conclusions

General conclusions

In this thesis, single-fiber imaging methods based on AFM or correlative AFM and (super-resolution) fluorescence microscopy have been developed and applied to the characterization of amyloid fibers with applications in very different fields, from new materials to biomedicine. These techniques allowed to extract multiparametric information from individual fibers providing a more advanced approach than traditional bulk techniques. The conclusions extracted from this thesis are:

1) Correlative microscopy is a helpful strategy to validate super-resolution fluorescence microscopy methods. The experiments performed in this thesis show how the combination of AFM used as a "ground truth" can be critical for SMLM optimization of the reconstruction image, evaluation of the labelling quality and image interpretation.

2) Correlative SMLM and AFM imaging has been successfully applied to evaluate the functionalization of BLG fibers with organic fluorophores and QDs, showing heterogeneous labeling at the nanoscale. These results prove that correlative microscopy is useful tool for characterizing luminescent nanomaterials providing valuable information about its structure and functionalization, which is relevant for new material development.

3) Different amyloid aggregates with wide morphological diversity were explored for selecting suitable models for AFM photodamage studies. Long and isolated fibers were desirable, and BLG, ΔN, ΔH1, Aβ 1-40 and Aβ 1-40 SO are identified as suitable models. Particularly BLG shows topographical periodicity related to its structural conformation, and is used as a first model for developing nanoscale photodamage imaging methodology.

4) Correlative fluorescence microscopy and AFM is a useful technique for studying binding of ROS-ThT at the single-fiber level. These experiments reveal complex binding of ROS-ThT and suggest a possible dependence with the fiber structural polymorphism.

5) Photodamage experiments show the effects of photo-oxidation produced by ROS-ThT on amyloid fibers at the nanoscale by AFM, revealing a complex dependency of photo-oxidation with structure. These experiments provide a novel way to visualize the effect of photosensitizers or photocatalysts at the nanoscale, and are relevant to improve phototherapeutic strategies for amyloid-related disorders.

Conclusiones generales

En esta tesis, se han desarrollado métodos de imagen basados en AFM, microscopía de fluorescencia (o súper resolución) y correlación entre ellas, para la caracterización de fibras individuales con aplicación en campos muy diferentes, desde los nuevos materiales hasta la biomedicina. Estas técnicas permitieron extraer información multiparamétrica de fibras individuales proporcionando una estrategia más avanzada que las técnicas bioquímicas tradicionales. Las conclusiones extraídas de esta tesis son:

1) La microscopía correlativa es una estrategia útil para validar los métodos de microscopía de fluorescencia de súper resolución. Los experimentos realizados en esta tesis muestran cómo la utilización de las imágenes de AFM como referencia puede ser crítica tanto para la optimización de la reconstrucción de la imagen de súper resolución y su interpretación como para la evaluación de la calidad del marcaje de la muestra.

2) La microscopía correlativa de AFM y de súper resolución se ha aplicado con éxito para evaluar la funcionalización de las fibras de BLG con fluoróforos orgánicos y QDs que muestran un marcaje heterogéneo a la nanoescala. Estos resultados demuestran que la microscopía correlativa es una herramienta útil para caracterizar nanomateriales luminiscentes proporcionando información valiosa sobre su estructura y funcionalización, lo cual es relevante para el desarrollo de nuevos materiales.

3) Se exploraron diferentes agregados amiloides con amplia diversidad morfológica para seleccionar los modelos más adecuados para estudiar por AFM el daño fotoquímico a la nanoescala. Se identificaron BLG, ΔN, ΔH1, Aβ 1-40 y Aβ 1-40 SO, como modelos apropiados por formar fibras largas y aisladas. Particularmente BLG muestra una periodicidad topográfica relacionada con su conformación estructural, y se utilizó como primer modelo para desarrollar la metodología de caracterización de daño fotodinámico a escala nanométrica.

4) La microscopía correlativa de AFM y fluorescencia es una técnica útil para estudiar la unión de ROS-ThT a nivel de fibra individual. Estos experimentos muestran la complejidad de la unión de ROS-ThT a las fibras y sugieren una posible dependencia con el polimorfismo de la fibra.

5) Los experimentos de daño fotoquímico muestran por AFM los efectos de la foto-oxidación producida por ROS-ThT sobre las fibras amiloides a la nanoescala, revelando una dependencia compleja entre la fotooxidación y la estructura. Estos experimentos proporcionan una forma novedosa de visualizar el efecto de los fotosensibilizadores a la nanoescala y son relevantes para mejorar las estrategias fototerapéuticas para los trastornos amiloides.

References

References

1. Land, M.F. & Fernald, R.D. The evolution of eyes. *Annual Review of Neuroscience* **15**, 1-29 (1992).
2. Kaas, J.H. The evolution of visual cortex in primates. *The Primate Visual System: A Comparative Approach* **9**, 267-283 (2005).
3. Egerton, F.N. A history of the ecological sciences, part 19: Leeuwenhoek's microscopic natural history. *The Bulletin of the Ecological Society of America* **87**, 47-58 (2006).
4. Masters, B.R. History of the optical microscope in cell biology and medicine. *In eLS (Ed.).* Doi:10.1002/9780470015902.a0003082. (2001).
5. Haguenau, F. et al. Key events in the history of electron microscopy. *Microscopy and Microanalysis* **9**, 96-138 (2003).
6. Cuevas, J. & Heglar, L.E. Photography and the discovery of the double helix structure of DNA. *Philosophy of Photography* **4**, 163-180 (2013).
7. Wuthrich, K. Protein structure determination in solution by nuclear magnetic resonance spectroscopy. *Science* **243**, 45-50 (1989).
8. Binnig, G., Quate, C.F. & Gerber, C. Atomic force microscope. *Physical Review Letters* **56**, 930 (1986).
9. Lal, R. & John, S.A. Biological applications of atomic force microscopy. *American Journal of Physiology-Cell Physiology* **266**, C1-C21 (1994).
10. Pohl, D.W., Denk, W. & Lanz, M. Optical stethoscopy: Image recording with resolution λ/20. *Applied Physics Letters* **44**, 651-653 (1984).
11. Klar, T.A., Jakobs, S., Dyba, M., Egner, A. & Hell, S.W. Fluorescence microscopy with diffraction resolution barrier broken by stimulated emission. *Proceedings of the National Academy of Sciences* **97**, 8206-8210 (2000).
12. Betzig, E. et al. Imaging intracellular fluorescent proteins at nanometer resolution. *Science* **313**, 1642-1645 (2006).
13. Knowles, T.P. & Mezzenga, R. Amyloid fibrils as building blocks for natural and artificial functional materials. *Advanced Materials* **28**, 6546-6561 (2016).
14. Fowler, D.M., Koulov, A.V., Balch, W.E. & Kelly, J.W. Functional amyloid–from bacteria to humans. *Trends in Biochemical Sciences* **32**, 217-224 (2007).
15. Huang, B., Bates, M. & Zhuang, X. Super-resolution fluorescence microscopy. *Annual Review of Biochemistry* **78**, 993-1016 (2009).
16. Patterson, G.H. Fluorescence microscopy below the diffraction limit. *Seminars In Cell & Developmental Biology* **20**, 886-893 (2009).
17. Leung, B.O. & Chou, K.C. Review of super-resolution fluorescence microscopy for biology. *Applied Spectroscopy* **65**, 967-980 (2011).
18. Rottenfusser, R., Wilson, E. E., & Davidson, M. W. Microscopy Basics | Image Formation - ZEISS Campus. (Access date: 7/09/2019) http://zeiss-campus.magnet.fsu.edu/articles/basics/imageformation.html
19. Möckl, L., Lamb, D.C. & Bräuchle, C. Super-resolved Fluorescence Microscopy: Nobel Prize in Chemistry 2014 for Eric Betzig, Stefan Hell, and William E. Moerner. *Angewandte Chemie International Edition* **53**, 13972-13977 (2014).
20. Betzig, E. Proposed method for molecular optical imaging. *Optics Letters* **20**, 237-239 (1995).
21. Moerner, W.E. & Kador, L. Optical detection and spectroscopy of single molecules in a solid. *Physical Review Letters* **62**, 2535-2538 (1989).
22. Dickson, R.M., Cubitt, A.B., Tsien, R.Y. & Moerner, W.E. On/off blinking and switching behaviour of single molecules of green fluorescent protein. *Nature* **388**, 355 (1997).

23. Hell, S.W. & Wichmann, J. Breaking the diffraction resolution limit by stimulated emission: stimulated-emission-depletion fluorescence microscopy. *Optics Letters* **19**, 780-782 (1994).
24. Bhattacharya, M. & Mukhopadhyay, S. Nanophotonics of protein amyloids. *Nanophotonics* **3**, 51-59 (2014).
25. Müller, T., Schumann, C. & Kraegeloh, A. STED microscopy and its applications: new insights into cellular processes on the nanoscale. *ChemPhysChem* **13**, 1986-2000 (2012).
26. Kner, P., Chhun, B.B., Griffis, E.R., Winoto, L. & Gustafsson, M.G. Super-resolution video microscopy of live cells by structured illumination. *Nature Methods* **6**, 339-342 (2009).
27. Van de Linde, S. et al. Direct stochastic optical reconstruction microscopy with standard fluorescent probes. *Nature Protocols* **6**, 991-1009 (2011).
28. Rust, M.J., Bates, M. & Zhuang, X. Sub-diffraction-limit imaging by stochastic optical reconstruction microscopy (STORM). *Nature Methods* **3**, 793-796 (2006).
29. Whelan, D.R. & Bell, T.D. Super-resolution single-molecule localization microscopy: tricks of the trade. *The Journal of Physical Chemistry Letters* **6**, 374-382 (2015).
30. Sahl, S.J. & Moerner, W. Super-resolution fluorescence imaging with single molecules. *Current Opinion in Structural Biology* **23**, 778-787 (2013).
31. Jradi, F.M. & Lavis, L.D. Photosensitive fluorophores for single-molecule localization microscopy. *ACS Chemical Biology* **14**, 1077-1090 (2019).
32. Jalili, N. & Laxminarayana, K. A review of atomic force microscopy imaging systems: application to molecular metrology and biological sciences. *Mechatronics* **14**, 907-945 (2004).
33. Dufrêne, Y.F., Martínez-Martín, D., Medalsy, I., Alsteens, D. & Müller, D.J. Multiparametric imaging of biological systems by force-distance curve–based AFM. *Nature Methods* **10**, 847-854 (2013).
34. Dufrêne, Y.F. et al. Imaging modes of atomic force microscopy for application in molecular and cell biology. *Nature Nanotechnology* **12**, 295-307 (2017).
35. Müller, D.J. & Dufrêne, Y.F. Atomic force microscopy as a multifunctional molecular toolbox in nanobiotechnology. *Nature Nanotechnology* **3**, 261-269 (2008).
36. Rief, M., Gautel, M., Oesterhelt, F., Fernandez, J.M. & Gaub, H.E. Reversible unfolding of individual titin immunoglobulin domains by AFM. *Science* **276**, 1109-1112 (1997).
37. Florin, E.-L., Moy, V.T. & Gaub, H.E. Adhesion forces between individual ligand-receptor pairs. *Science* **264**, 415-417 (1994).
38. Hinterdorfer, P., Baumgartner, W., Gruber, H.J., Schilcher, K. & Schindler, H. Detection and localization of individual antibody-antigen recognition events by atomic force microscopy. *Proceedings of the National Academy of Sciences* **93**, 3477-3481 (1996).
39. Gerber, C. & Lang, H.P. How the doors to the nanoworld were opened. *Nature Nanotechnology* **1**, 3-5 (2006).
40. Kumar, S. & LeDuc, P.R. Dissecting the molecular basis of the mechanics of living cells. *Experimental Mechanics* **49**, 11-23 (2009).
41. Rubio-Sierra, F.J., Heckl, W.M. & Stark, R.W. Nanomanipulation by atomic force microscopy. *Advanced Engineering Materials* **7**, 193-196 (2005).
42. Hernando-Pérez, M. et al. The interplay between mechanics and stability of viral cages. *Nanoscale* **6**, 2702-2709 (2014).
43. Mertens, J. et al. Mechanics of virus-like particles labeled with green fluorescent protein. *Biophysical journal* **115**, 1561-1568 (2018).
44. Oesterhelt, F. et al. Unfolding pathways of individual bacteriorhodopsins. *Science* **288**, 143-146 (2000).
45. Hauser, M. et al. Correlative super-resolution microscopy: new dimensions and new opportunities. *Chemical Reviews* **117**, 7428-7456 (2017).
46. Sosinsky, G.E., Giepmans, B.N., Deerinck, T.J., Gaietta, G.M. & Ellisman, M.H. Markers for correlated light and electron microscopy. *Methods in Cell Biology* **79**, 575-591 (2007).

47. De Boer, P., Hoogenboom, J.P. & Giepmans, B.N. Correlated light and electron microscopy: ultrastructure lights up! *Nature Methods* **12**, 503-513 (2015).
48. Caplan, J., Niethammer, M., Taylor II, R.M. & Czymmek, K.J. The power of correlative microscopy: multi-modal, multi-scale, multi-dimensional. *Current Opinion in Structural Biology* **21**, 686-693 (2011).
49. Lee, M.J. et al. Engineered synthetic scaffolds for organizing proteins within the bacterial cytoplasm. *Nature Chemical Biology* **14**, 142 (2018).
50. Bondia, P., Casado, S. & Flors, C. Correlative super-resolution fluorescence imaging and atomic force microscopy for the characterization of biological samples. *In: Erfle H. (eds) Super-Resolution Microscopy. Methods in Molecular Biology,* **1663**, 105-113 Humana Press, New York, NY. (2017).
51. Hecht, E. et al. Combined atomic force microscopy–fluorescence microscopy: analyzing exocytosis in alveolar type II cells. *Analytical Chemistry* **84**, 5716-5722 (2012).
52. Fantner, G.E., Barbero, R.J., Gray, D.S. & Belcher, A.M. Kinetics of antimicrobial peptide activity measured on individual bacterial cells using high-speed atomic force microscopy. *Nature Nanotechnology* **5**, 280-285 (2010).
53. Ortega-Esteban, A. et al. Fluorescence tracking of genome release during mechanical unpacking of single viruses. *ACS Nano* **9**, 10571-10579 (2015).
54. Nishida, S., Funabashi, Y. & Ikai, A. Combination of AFM with an objective-type total internal reflection fluorescence microscope (TIRFM) for nanomanipulation of single cells. *Ultramicroscopy* **91**, 269-274 (2002).
55. Odermatt, P.D. et al. High-resolution correlative microscopy: bridging the gap between single molecule localization microscopy and atomic force microscopy. *Nano Letters* **15**, 4896-4904 (2015).
56. Harke, B., Chacko, J.V., Haschke, H., Canale, C. & Diaspro, A. A novel nanoscopic tool by combining AFM with STED microscopy. *Optical Nanoscopy* **1**, 3 (2012).
57. Bondia, P. et al. Hybrid nanoscopy of hybrid nanomaterials. *Small* **13**, 1603784 (2017).
58. Dahmane, S. et al. Nanoscale organization of tetraspanins during HIV-1 budding by correlative dSTORM/AFM. *Nanoscale* **11**, 6036-6044 (2019).
59. Curry, N., Ghézali, G., Kaminski Schierle, G.S., Rouach, N. & Kaminski, C.F. Correlative STED and atomic force microscopy on live astrocytes reveals plasticity of cytoskeletal structure and membrane physical properties during polarized migration. *Frontiers in Cellular Neuroscience* **11**, 104 (2017).
60. Chacko, J.V., Zanacchi, F.C. & Diaspro, A. Probing cytoskeletal structures by coupling optical superresolution and AFM techniques for a correlative approach. *Cytoskeleton* **70**, 729-740 (2013).
61. Chacko, J.V., Harke, B., Canale, C. & Diaspro, A. Cellular level nanomanipulation using atomic force microscope aided with superresolution imaging. *Journal of Biomedical Optics* **19**, 105003 (2014).
62. Chacko, J.V., Canale, C., Harke, B. & Diaspro, A. Sub-diffraction nano manipulation using STED AFM. *PloS One* **8**, e66608 (2013).
63. Cosentino, M., Canale, C., Bianchini, P. & Diaspro, A. AFM-STED correlative nanoscopy reveals a dark side in fluorescence microscopy imaging. *Science Advances* **5**, eaav8062 (2019).
64. Monserrate, A., Casado, S. & Flors, C. Correlative atomic force microscopy and localization-based super-resolution microscopy: revealing labelling and image reconstruction artefacts. *ChemPhysChem* **15**, 647-650 (2014).
65. Janel, S. et al. Stiffness tomography of eukaryotic intracellular compartments by atomic force microscopy. *Nanoscale* **11**, 10320-10328 (2019).
66. O'Connor, C.M., Adams, J.U. & Fairman, J. Essentials of cell biology. *Cambridge, MA: NPG Education* **1**, 14749010 (2010).

67. Pappu, R.V., Wang, X., Vitalis, A. & Crick, S.L. A polymer physics perspective on driving forces and mechanisms for protein aggregation. *Archives of Biochemistry and Biophysics* **469**, 132-141 (2008).
68. Wei, G. et al. Self-assembling peptide and protein amyloids: from structure to tailored function in nanotechnology. *Chemical Society Reviews* **46**, 4661-4708 (2017).
69. Wu, J.W. et al. Carnosine's effect on amyloid fibril formation and induced cytotoxicity of lysozyme. *PloS One* **8**, e81982 (2013).
70. Karamanos, T.K., Kalverda, A.P., Thompson, G.S. & Radford, S.E. Mechanisms of amyloid formation revealed by solution NMR. *Progress in Nuclear Magnetic Resonance Spectroscopy* **88**, 86-104 (2015).
71. Sasso, L. et al. Versatile multi-functionalization of protein nanofibrils for biosensor applications. *Nanoscale* **6**, 1629-1634 (2014).
72. Cherny, I. & Gazit, E. Amyloids: not only pathological agents but also ordered nanomaterials. *Angewandte Chemie International Edition* **47**, 4062-4069 (2008).
73. Zeng, G. et al. Functional bacterial amyloid increases Pseudomonas biofilm hydrophobicity and stiffness. *Frontiers in Microbiology* **6**, 1099 (2015).
74. Chapman, M.R. et al. Role of Escherichia coli curli operons in directing amyloid fiber formation. *Science* **295**, 851-855 (2002).
75. Jensen, M.A., True, H.L., Chernoff, Y.O. & Lindquist, S. Molecular population genetics and evolution of a prion-like protein in Saccharomyces cerevisiae. *Genetics* **159**, 527-535 (2001).
76. Wickner, R.B. [URE3] as an altered URE2 protein: evidence for a prion analog in Saccharomyces cerevisiae. *Science* **264**, 566-569 (1994).
77. Dalstra, H.J. et al. Non-mendelian inheritance of the HET-s prion or HET-s prion domains determines the het-S spore killing system in Podospora anserina. *Fungal Genetics and Biology* **42**, 836-847 (2005).
78. Shorter, J. & Lindquist, S. Prions as adaptive conduits of memory and inheritance. *Nature Reviews Genetics* **6**, 435-450 (2005).
79. Maji, S.K. et al. Functional amyloids as natural storage of peptide hormones in pituitary secretory granules. *Science* **325**, 328-332 (2009).
80. Reynolds, N.P., Charnley, M., Mezzenga, R. & Hartley, P.G. Engineered lysozyme amyloid fibril networks support cellular growth and spreading. *Biomacromolecules* **15**, 599-608 (2014).
81. Reynolds, N.P. et al. Nanotopographic surfaces with defined surface chemistries from amyloid fibril networks can control cell attachment. *Biomacromolecules* **14**, 2305-2316 (2013).
82. Li, C. et al. Amyloid-hydroxyapatite bone biomimetic composites. *Advanced Materials* **26**, 3207-3212 (2014).
83. Bolisetty, S., Adamcik, J., Heier, J. & Mezzenga, R. Amyloid directed synthesis of titanium dioxide nanowires and their applications in hybrid photovoltaic devices. *Advanced Functional Materials* **22**, 3424-3428 (2012).
84. Men, D. et al. Seeding-induced self-assembling protein nanowires dramatically increase the sensitivity of immunoassays. *Nano Letters* **9**, 2246-2250 (2009).
85. Zhong, C. et al. Strong underwater adhesives made by self-assembling multi-protein nanofibres. *Nature Nanotechnology* **9**, 858-866 (2014).
86. Jurado, R. et al. Apoferritin fibers: a new template for 1D fluorescent hybrid nanostructures. *Nanoscale* **8**, 9648-9656 (2016).
87. Hendler, N. et al. Multiple self-assembly functional structures based on versatile binding sites of β-Lactoglobulin. *Advanced Functional Materials* **22**, 3765-3776 (2012).
88. Pilkington, S.M., Roberts, S.J., Meade, S.J. & Gerrard, J.A. Amyloid fibrils as a nanoscaffold for enzyme immobilization. *Biotechnology progress* **26**, 93-100 (2010).

89. Schreiber, R. et al. Hierarchical assembly of metal nanoparticles, quantum dots and organic dyes using DNA origami scaffolds. *Nature Nanotechnology* **9**, 74 (2013).
90. Bolisetty, S. et al. Amyloid fibrils enhance transport of metal nanoparticles in living cells and induced cytotoxicity. *Biomacromolecules* **15**, 2793-2799 (2014).
91. Bolisetty, S., Vallooran, J.J., Adamcik, J. & Mezzenga, R. Magnetic-responsive hybrids of Fe3O4 nanoparticles with β-lactoglobulin amyloid fibrils and nanoclusters. *ACS Nano* **7**, 6146-6155 (2013).
92. Rizzo, A., Solin, N., Lindgren, L.J., Andersson, M.R. & Inganäs, O. White light with phosphorescent protein fibrils in OLEDs. *Nano Letters* **10**, 2225-2230 (2010).
93. Chen, A.Y. et al. Synthesis and patterning of tunable multiscale materials with engineered cells. *Nature Materials* **13**, 515-523 (2014).
94. Aili, D. & Stevens, M.M. Bioresponsive peptide–inorganic hybrid nanomaterials. *Chemical Society Reviews* **39**, 3358-3370 (2010).
95. Wang, X., Li, Y. & Zhong, C. Amyloid-directed assembly of nanostructures and functional devices for bionanoelectronics. *Journal of Materials Chemistry B* **3**, 4953-4958 (2015).
96. Tipping, K.W., van Oosten-Hawle, P., Hewitt, E.W. & Radford, S.E. Amyloid Fibres: Inert End-Stage Aggregates or Key Players in Disease? *Trends in Biochemical Sciences* **40**, 719-727 (2015).
97. Chiti, F. & Dobson, C.M. Protein Misfolding, Amyloid Formation, and Human Disease: A Summary of Progress Over the Last Decade. *Annual Review of Biochemistry* **86**, 27-68 (2017).
98. Tompa, P. Structural disorder in amyloid fibrils: its implication in dynamic interactions of proteins. *The FEBS Journal* **276**, 5406-5415 (2009).
99. Li, J., Uversky, V.N. & Fink, A.L. Effect of familial Parkinson's disease point mutations A30P and A53T on the structural properties, aggregation, and fibrillation of human α-synuclein. *Biochemistry* **40**, 11604-11613 (2001).
100. Krone, M.G. et al. Effects of familial Alzheimer's disease mutations on the folding nucleation of the amyloid β-protein. *Journal of Molecular Biology* **381**, 221-228 (2008).
101. Sun, X., Chen, W.-D. & Wang, Y.-D. β-Amyloid: the key peptide in the pathogenesis of Alzheimer's disease. *Frontiers in Pharmacology* **6**, 221 (2015).
102. Chartier-Harlin, M.-C. et al. α-Synuclein locus duplication as a cause of familial Parkinson's disease. *The Lancet* **364**, 1167-1169 (2004).
103. Viles, J.H. Metal ions and amyloid fiber formation in neurodegenerative diseases. Copper, zinc and iron in Alzheimer's, Parkinson's and prion diseases. *Coordination Chemistry Reviews* **256**, 2271-2284 (2012).
104. Simons, M. et al. Cholesterol depletion inhibits the generation of β-amyloid in hippocampal neurons. *Proceedings of the National Academy of Sciences* **95**, 6460-6464 (1998).
105. Xiong, H. et al. Cholesterol retention in Alzheimer's brain is responsible for high β- and γ-secretase activities and Aβ production. *Neurobiology of Disease* **29**, 422-437 (2008).
106. Stewart, K.L. et al. Atomic details of the interactions of glycosaminoglycans with amyloid-β fibrils. *Journal of the American Chemical Society* **138**, 8328-8331 (2016).
107. Iadanza, M.G., Jackson, M.P., Hewitt, E.W., Ranson, N.A. & Radford, S.E. A new era for understanding amyloid structures and disease. *Nature Reviews Molecular Cell Biology* **19**, 755-773 (2018).
108. Wentink, A., Nussbaum-Krammer, C. & Bukau, B. Modulation of amyloid states by molecular chaperones. *Cold Spring Harbor Perspectives in Biology* **11**, a033969 (2019).
109. Glabe, C.G. Common mechanisms of amyloid oligomer pathogenesis in degenerative disease. *Neurobiology of Aging* **27**, 570-575 (2006).
110. Li, Y. et al. Amyloid fibril structure of α-synuclein determined by cryo-electron microscopy. *Cell Research* **28**, 897-903 (2018).

111. Tuttle, M.D. et al. Solid-state NMR structure of a pathogenic fibril of full-length human α-synuclein. *Nature Structural & Molecular Biology* **23**, 409-415 (2016).
112. Gremer, L. et al. Fibril structure of amyloid-β (1–42) by cryo–electron microscopy. *Science* **358**, 116-119 (2017).
113. Lu, J.-X. et al. Molecular structure of β-amyloid fibrils in Alzheimer's disease brain tissue. *Cell* **154**, 1257-1268 (2013).
114. Paravastu, A.K., Leapman, R.D., Yau, W.-M. & Tycko, R. Molecular structural basis for polymorphism in Alzheimer's β-amyloid fibrils. *Proceedings of the National Academy of Sciences* **105**, 18349-18354 (2008).
115. Toyama, B.H. & Weissman, J.S. Amyloid structure: conformational diversity and consequences. *Annual Review of Biochemistry* **80**, 557-585 (2011).
116. Tycko, R. Amyloid polymorphism: structural basis and neurobiological relevance. *Neuron* **86**, 632-645 (2015).
117. Sweeney, P. et al. Protein misfolding in neurodegenerative diseases: implications and strategies. *Translational Neurodegeneration* **6**, 6 (2017).
118. Sanders, D.W. et al. Distinct tau prion strains propagate in cells and mice and define different tauopathies. *Neuron* **82**, 1271-1288 (2014).
119. Heilbronner, G. et al. Seeded strain-like transmission of β-amyloid morphotypes in APP transgenic mice. *EMBO Rep* **14**, 1017-1022 (2013).
120. Cheng, B. et al. Interaction between amyloidogenic proteins and biomembranes in protein misfolding diseases: Mechanisms, contributors, and therapy. *Biochimica et Biophysica Acta (BBA) - Biomembranes* **1860**, 1876-1888 (2018).
121. Lewis, F.W. & Tétard, D. An overview of multifunctional metal chelators as potential treatments for neurodegenerative diseases. *In Biometals in Neurodegenerative Diseases*, 399-414. Elsevier, San Diego (2017).
122. Lindberg, I. et al. Chaperones in neurodegeneration. *The Journal of Neuroscience* **35**, 13853-13859 (2015).
123. Li, X. et al. Naturally occurring antibodies isolated from PD patients inhibit synuclein seeding in vitro and recognize Lewy pathology. *Acta Neuropathologica* **137**, 825-836 (2019).
124. Cheng, B. et al. Silibinin inhibits the toxic aggregation of human islet amyloid polypeptide. *Biochemical and Biophysical Research Communications* **419**, 495-499 (2012).
125. Gong, H. et al. Effects of several quinones on insulin aggregation. *Scientific Reports* **4**, 5648 (2014).
126. Barten, D.M. et al. Dynamics of β-amyloid reductions in brain, cerebrospinal fluid, and plasma of β-amyloid precursor protein transgenic mice treated with a γ-secretase inhibitor. *Journal of Pharmacology and Experimental Therapeutics* **312**, 635-643 (2005).
127. Jick, H., Zornberg, G.L., Jick, S.S., Seshadri, S. & Drachman, D.A. Statins and the risk of dementia. *The Lancet* **356**, 1627-1631 (2000).
128. Wijesekara, N. et al. ABCA1 deficiency and cellular cholesterol accumulation increases islet amyloidogenesis in mice. *Diabetologia* **59**, 1242-1246 (2016).
129. Malishev, R. et al. Toxicity inhibitors protect lipid membranes from disruption by Aβ42. *ACS Chemical Neuroscience* **6**, 1860-1869 (2015).
130. Lolicato, F., Raudino, A., Milardi, D. & La Rosa, C. Resveratrol interferes with the aggregation of membrane-bound human-IAPP: a molecular dynamics study. *European Journal of Medicinal Chemistry* **92**, 876-881 (2015).
131. Anekonda, T.S. & Quinn, J.F. Calcium channel blocking as a therapeutic strategy for Alzheimer's disease: the case for isradipine. *Biochimica Et Biophysica Acta (BBA)-Molecular Basis of Disease* **1812**, 1584-1590 (2011).

132. Diaz, J.C., Simakova, O., Jacobson, K.A., Arispe, N. & Pollard, H.B. Small molecule blockers of the Alzheimer Aβ calcium channel potently protect neurons from Aβ cytotoxicity. *Proceedings of the National Academy of Sciences* **106**, 3348-3353 (2009).
133. Smith, H.L., Li, W. & Cheetham, M.E. Molecular chaperones and neuronal proteostasis. *Seminars in Cell & Developmental Biology* **40**, 142-152 (2015).
134. DeSantis, Morgan E. et al. Operational plasticity enables Hsp104 to disaggregate diverse amyloid and nonamyloid clients. *Cell* **151**, 778-793 (2012).
135. Liu, Y.-H. et al. Heat shock protein 104 inhibited the fibrillization of prion peptide 106–126 and disassembled prion peptide 106–126 fibrils in vitro. *The International Journal of Biochemistry & Cell Biology* **43**, 768-774 (2011).
136. De Genst, E., Messer, A. & Dobson, C.M. Antibodies and protein misfolding: From structural research tools to therapeutic strategies. *Biochimica et Biophysica Acta (BBA) - Proteins and Proteomics* **1844**, 1907-1919 (2014).
137. Baskaran, R., Lee, J. & Yang, S.-G. Clinical development of photodynamic agents and therapeutic applications. *Biomater Res* **22**, 25-25 (2018).
138. Chung, Y.J., Lee, B.I., Ko, J.W. & Park, C.B. Photoactive g-C3N4 nanosheets for light-Induced suppression of Alzheimer's β-Amyloid aggregation and toxicity. *Advanced Healthcare Materials* **5**, 1560-1565 (2016).
139. Lee, B.I., Suh, Y.S., Chung, Y.J., Yu, K. & Park, C.B. Shedding light on Alzheimer's β-Amyloidosis: Photosensitized methylene blue inhibits self-assembly of β-Amyloid peptides and disintegrates their aggregates. *Scientific Reports* **7**, 7523 (2017).
140. Son, G., Lee, B.I., Chung, Y.J. & Park, C.B. Light-triggered dissociation of self-assembled β-amyloid aggregates into small, nontoxic fragments by ruthenium (II) complex. *Acta Biomaterialia* **67**, 147-155 (2018).
141. Kang, J. et al. An iridium(III) complex as a photoactivatable tool for oxidation of amyloidogenic peptides with subsequent modulation of peptide aggregation. *Chemistry – A European Journal* **23**, 1645-1653 (2017).
142. Ni, J. et al. Near-infrared photoactivatable oxygenation catalysts of amyloid peptide. *Chem* **4**, 807-820 (2018).
143. Taniguchi, A., Shimizu, Y., Oisaki, K., Sohma, Y. & Kanai, M. Switchable photooxygenation catalysts that sense higher-order amyloid structures. *Nature Chemistry* **8**, 974 (2016).
144. Suzuki, T. et al. Photo-oxygenation inhibits tau amyloid formation. *Chemical Communications* **55**, 6165-6168 (2019).
145. Schindelin, J. et al. Fiji: an open-source platform for biological-image analysis. *Nature methods* **9**, 676 (2012).
146. Nečas, D. & Klapetek, P. Gwyddion: an open-source software for SPM data analysis. *Open Physics* **10**, 181-188 (2012).
147. Dedecker, P., Duwé, S., Neely, R.K. & Zhang, J. Localizer: fast, accurate, open-source, and modular software package for superresolution microscopy. *Journal of Biomedical Optics* **17**, 126008 (2012).
148. Fronczek, D. et al. High accuracy FIONA–AFM hybrid imaging. *Ultramicroscopy* **111**, 350-355 (2011).
149. Saraji, S., Piri, M. & Goual, L. The effects of SO2 contamination, brine salinity, pressure, and temperature on dynamic contact angles and interfacial tension of supercritical CO2/brine/quartz systems. *International Journal of Greenhouse Gas Control* **28**, 147-155 (2014).
150. Pinotsi, D., Schierle, G.S.K., Rees, E. & Kaminski, C.F. Localization microscopy for the study of amyloid fibril formation. *Nanoimaging and Nanospectroscopy* **8815**, 88150G (2013).
151. Zhang, W.I., Röhse, H., Rizzoli, S.O. & Opazo, F. Fluorescent in situ hybridization of synaptic proteins imaged with super-resolution STED microscopy. *Microscopy Research and Technique* **77**, 517-527 (2014).

152. Dempsey, G.T., Vaughan, J.C., Chen, K.H., Bates, M. & Zhuang, X. Evaluation of fluorophores for optimal performance in localization-based super-resolution imaging. *Nature Methods* **8**, 1027-1036 (2011).
153. Xu, J., Tehrani, K.F. & Kner, P. Multicolor 3D super-resolution imaging by quantum dot stochastic optical reconstruction microscopy. *ACS Nano* **9**, 2917-2925 (2015).
154. Lidke, K.A., Rieger, B., Jovin, T.M. & Heintzmann, R. Superresolution by localization of quantum dots using blinking statistics. *Optics Express* **13**, 7052-7062 (2005).
155. Chien, F.-C., Kuo, C.W. & Chen, P. Localization imaging using blinking quantum dots. *Analyst* **136**, 1608-1613 (2011).
156. Dertinger, T., Colyer, R., Iyer, G., Weiss, S. & Enderlein, J. Fast, background-free, 3D super-resolution optical fluctuation imaging (SOFI). *Proceedings of the National Academy of Sciences* **106**, 22287-22292 (2009).
157. Watanabe, T.M., Fukui, S., Jin, T., Fujii, F. & Yanagida, T. Real-time nanoscopy by using blinking enhanced quantum dots. *Biophysical Journal* **99**, L50-L52 (2010).
158. Wang, Y., Fruhwirth, G., Cai, E., Ng, T. & Selvin, P.R. 3D super-resolution imaging with blinking quantum dots. *Nano Letters* **13**, 5233-5241 (2013).
159. Hansma, P. et al. Tapping mode atomic force microscopy in liquids. *Applied Physics Letters* **64**, 1738-1740 (1994).
160. De Pablo, P., Colchero, J., Gomez-Herrero, J. & Baro, A. Jumping mode scanning force microscopy. *Applied Physics Letters* **73**, 3300-3302 (1998).
161. Moreno-Herrero, F., Colchero, J., Gomez-Herrero, J. & Baro, A. Atomic force microscopy contact, tapping, and jumping modes for imaging biological samples in liquids. *Physical Review E* **69**, 031915 (2004).
162. Dorobantu, L.S., Goss, G.G. & Burrell, R.E. Atomic force microscopy: a nanoscopic view of microbial cell surfaces. *Micron* **43**, 1312-1322 (2012).
163. Duim, W.C., Chen, B., Frydman, J. & Moerner, W. Sub-diffraction imaging of Huntingtin protein aggregates by aluorescence blink-microscopy and atomic force microscopy. *ChemPhysChem* **12**, 2387-2390 (2011).
164. Bowen, W.R. & Doneva, T.A. Artefacts in AFM studies of membranes: correcting pore images using fast fourier transform filtering. *Journal of Membrane Science* **171**, 141-147 (2000).
165. Lee, J.K., Jäckel, F., Moerner, W.E. & Bao, Z. Micrometer-sized DNA–single-fluorophore–DNA supramolecule: Synthesis and single-molecule characterization. *Small* **5**, 2418-2423 (2009).
166. Sanchez, H., Kertokalio, A., van Rossum-Fikkert, S., Kanaar, R. & Wyman, C. Combined optical and topographic imaging reveals different arrangements of human RAD54 with presynaptic and postsynaptic RAD51–DNA filaments. *Proceedings of the National Academy of Sciences* **110**, 11385-11390 (2013).
167. Sanchez, H., Kanaar, R. & Wyman, C. Molecular recognition of DNA–protein complexes: A straightforward method combining scanning force and fluorescence microscopy. *Ultramicroscopy* **110**, 844-851 (2010).
168. Dickerson, M.B., Sandhage, K.H. & Naik, R.R. Protein- and peptide-directed syntheses of inorganic materials. *Chemical Reviews* **108**, 4935-4978 (2008).
169. Reches, M. & Gazit, E. Controlled patterning of aligned self-assembled peptide nanotubes. *Nature Nanotechnology* **1**, 195-200 (2006).
170. Zan, X., Feng, S., Balizan, E., Lin, Y. & Wang, Q. Facile method for large scale alignment of one dimensional nanoparticles and control over myoblast orientation and differentiation. *ACS Nano* **7**, 8385-8396 (2013).
171. Adamcik, J. et al. Understanding amyloid aggregation by statistical analysis of atomic force microscopy images. *Nature Nanotechnology* **5**, 423 (2010).

172. Ebenstein, Y., Mokari, T. & Banin, U. Fluorescence quantum yield of CdSe/ZnS nanocrystals investigated by correlated atomic-force and single-particle fluorescence microscopy. *Applied Physics Letters* **80**, 4033-4035 (2002).
173. Pons, T. et al. Single-Molecule Colocalization Studies Shed Light on the Idea of Fully Emitting versus Dark Single Quantum Dots. *Small* **7**, 2101-2108 (2011).
174. Oldfield, C.J. & Dunker, A.K. Intrinsically disordered proteins and intrinsically disordered protein regions. *Annual Review of Biochemistry* **83**, 553-584 (2014).
175. Chae, S., Lee, S., Kim, K., Jang, S.W. & Sohn, B.-H. Fluorescent supracolloidal polymer chains with quantum dots. *Chemical Communications* **52**, 6475-6478 (2016).
176. Bui, H. et al. Programmable Periodicity of Quantum Dot Arrays with DNA Origami Nanotubes. *Nano Letters* **10**, 3367-3372 (2010).
177. Dopf, K. et al. Superresolution optical fluctuation imaging (SOFI) aided nanomanipulation of quantum dots using AFM for novel artificial arrangements of chemically functionalized colloidal quantum dots and plasmonic structures. *Proc. SPIE, Nanophotonics V,* **9126**, 91260N (2014).
178. Bendor, Jacob T., Logan, Todd P. & Edwards, Robert H. The Function of α-Synuclein. *Neuron* **79**, 1044-1066 (2013).
179. Fauvet, B. et al. α-Synuclein in central nervous system and from erythrocytes, mammalian cells, and Escherichia coli exists predominantly as disordered monomer. *Journal of Biological Chemistry* **287**, 15345-15364 (2012).
180. Pattison, D.I., Rahmanto, A.S. & Davies, M.J. Photo-oxidation of proteins. *Photochemical & Photobiological Sciences* **11**, 38-53 (2012).
181. Goedert, M. Alpha-synuclein and neurodegenerative diseases. *Nature Reviews Neuroscience* **2**, 492 (2001).
182. Burré, J., Sharma, M. & Südhof, T.C. Cell biology and pathophysiology of α-synuclein. *Cold Spring Harbor Perspectives in Medicine* **8**, a024091 (2018).
183. Peelaerts, W., Bousset, L., Baekelandt, V. & Melki, R. α-Synuclein strains and seeding in Parkinson's disease, incidental Lewy body disease, dementia with Lewy bodies and multiple system atrophy: similarities and differences. *Cell and Tissue Research* **373**, 195-212 (2018).
184. Sot, B. et al. The chaperonin CCT inhibits assembly of α-synuclein amyloid fibrils by a specific, conformation-dependent interaction. *Scientific Reports* **7**, 40859 (2017).
185. Ullman, O., Fisher, C.K. & Stultz, C.M. Explaining the structural plasticity of α-synuclein. *Journal of the American Chemical Society* **133**, 19536-19546 (2011).
186. Terada, M. et al. The effect of truncation on prion-like properties of α-synuclein. *Journal of Biological Chemistry* **293**, 13910-13920 (2018).
187. Kessler, J.C., Rochet, J.-C. & Lansbury, P.T. The N-terminal repeat domain of α-synuclein inhibits β-sheet and amyloid fibril formation. *Biochemistry* **42**, 672-678 (2003).
188. Nalivaeva, N.N. & Turner, A.J. The amyloid precursor protein: a biochemical enigma in brain development, function and disease. *FEBS letters* **587**, 2046-2054 (2013).
189. Puzzo, D. & Arancio, O. Amyloid-β peptide: Dr. Jekyll or Mr. Hyde? *Journal of Alzheimer's Disease* **33**, S111-S120 (2013).
190. Cheignon, C. et al. Oxidative stress and the amyloid beta peptide in Alzheimer's disease. *Redox Biology* **14**, 450-464 (2018).
191. Sadigh-Eteghad, S. et al. Amyloid-beta: a crucial factor in Alzheimer's disease. *Medical Principles and Practice* **24**, 1-10 (2015).
192. Selkoe, D.J. Soluble oligomers of the amyloid β-protein impair synaptic plasticity and behavior. *Behavioural Brain Research* **192**, 106-113 (2008).
193. Lindberg, D.J., Wranne, M.S., Gatty, M.G., Westerlund, F. & Esbjörner, E.K. Steady-state and time-resolved Thioflavin-T fluorescence can report on morphological differences in amyloid fibrils formed by Aβ (1-40) and Aβ (1-42). *Biochemical and Biophysical Research Communications* **458**, 418-423 (2015).

194. Sciarretta, K.L., Gordon, D.J., Petkova, A.T., Tycko, R. & Meredith, S.C. Aβ40-Lactam (D23/K28) models a conformation highly favorable for nucleation of amyloid. *Biochemistry* **44**, 6003-6014 (2005).
195. Butterfield, D.A., Reed, T., Newman, S.F. & Sultana, R. Roles of amyloid β-peptide-associated oxidative stress and brain protein modifications in the pathogenesis of Alzheimer's disease and mild cognitive impairment. *Free Radical Biology and Medicine* **43**, 658-677 (2007).
196. Dong, J. et al. Metal binding and oxidation of amyloid-β within isolated senile plaque cores: Raman microscopic evidence. *Biochemistry* **42**, 2768-2773 (2003).
197. Holt, C. et al. Apparent chemical composition of nine commercial or semi-commercial whey protein concentrates, isolates and fractions. *International Journal of Food Science & Technology* **34**, 543-556 (1999).
198. Guyomarc'h, F. et al. Current ways to modify the structure of whey proteins for specific functionalities—a review. *Dairy Science & Technology* **95**, 795-814 (2015).
199. Zappone, B., De Santo, M.P., Labate, C., Rizzuti, B. & Guzzi, R. Catalytic activity of copper ions in the amyloid fibrillation of β-lactoglobulin. *Soft Matter* **9**, 2412-2419 (2013).
200. Lara, C., Adamcik, J., Jordens, S. & Mezzenga, R. General self-assembly mechanism converting hydrolyzed globular proteins into giant multistranded amyloid ribbons. *Biomacromolecules* **12**, 1868-1875 (2011).
201. Krebs, M.R., Bromley, E.H. & Donald, A.M. The binding of thioflavin-T to amyloid fibrils: localisation and implications. *Journal of Structural Biology* **149**, 30-37 (2005).
202. Schmitt, C. et al. Multiscale Characterization of Individualized β-Lactoglobulin Microgels Formed upon Heat Treatment under Narrow pH Range Conditions. *Langmuir* **25**, 7899-7909 (2009).
203. Akkermans, C. et al. Peptides are building blocks of heat-induced fibrillar protein aggregates of β-lactoglobulin formed at pH 2. *Biomacromolecules* **9**, 1474-1479 (2008).
204. Hamada, D. et al. Competition between folding, native-state dimerisation and amyloid aggregation in β-lactoglobulin. *Journal of Molecular Biology* **386**, 878-890 (2009).
205. Keppler, J.K., Heyn, T.R., Meissner, P.M., Schrader, K. & Schwarz, K. Protein oxidation during temperature-induced amyloid aggregation of beta-lactoglobulin. *Food Chemistry* **15**, 223-231 (2019).
206. Hoyer, W. et al. Dependence of α-synuclein aggregate morphology on solution conditions. *Journal of Molecular Biology* **322**, 383-393 (2002).
207. Sohma, Y. & Kiso, Y. Synthesis of O-Acyl Isopeptides. *The Chemical Record* **13**, 218-223 (2013).
208. Sohma, Y. Medicinal Chemistry Focusing on Aggregation of Amyloid-β. *Chemical and Pharmaceutical Bulletin* **64**, 1-7 (2016).
209. Yamamoto, M., Shinoda, K., Sasaki, D., Kanai, M. & Sohma, Y. Design and properties of [Met35 (O)] Aβ42-lactam (Asp23/Lys28) possessing a lactam tether as a salt-bridge surrogate. *Bioorganic & Medicinal Chemistry* **27**, 888-893 (2019).
210. Jung, J.-M., Savin, G., Pouzot, M., Schmitt, C. & Mezzenga, R. Structure of heat-induced β-lactoglobulin aggregates and their complexes with sodium-dodecyl sulfate. *Biomacromolecules* **9**, 2477-2486 (2008).
211. Adamcik, J. & Mezzenga, R. Adjustable twisting periodic pitch of amyloid fibrils. *Soft Matter* **7**, 5437-5443 (2011).
212. Uversky, V.N. et al. Methionine oxidation inhibits fibrillation of human alpha-synuclein in vitro. *FEBS Lett* **517**, 239-244 (2002).
213. Taniguchi, A. et al. Attenuation of the Aggregation and Neurotoxicity of Amyloid-β Peptides by Catalytic Photooxygenation. *Angewandte Chemie International Edition* **53**, 1382-1385 (2014).

214. Butterfield, D.A. & Boyd-Kimball, D. The critical role of methionine 35 in Alzheimer's amyloid β-peptide (1–42)-induced oxidative stress and neurotoxicity. *Biochimica et Biophysica Acta (BBA) - Proteins and Proteomics* **1703**, 149-156 (2005).
215. Breydo, L. et al. Methionine oxidation interferes with conversion of the prion protein into the fibrillar proteinase K-resistant conformation. *Biochemistry* **44**, 15534-15543 (2005).
216. Maleknia, S.D., Reixach, N. & Buxbaum, J.N. Oxidation inhibits amyloid fibril formation of transthyretin. *The FEBS journal* **273**, 5400-5406 (2006).
217. Binger, K.J., Griffin, M.D. & Howlett, G.J. Methionine oxidation inhibits assembly and promotes disassembly of apolipoprotein C-II amyloid fibrils. *Biochemistry* **47**, 10208-10217 (2008).
218. Chimon, S. et al. Evidence of fibril-like β-sheet structures in a neurotoxic amyloid intermediate of Alzheimer's β-amyloid. *Nature Structural & Molecular Biology* **14**, 1157-1164 (2007).
219. Groenning, M. Binding mode of Thioflavin T and other molecular probes in the context of amyloid fibrils—current status. *Journal of Chemical Biology* **3**, 1-18 (2010).
220. Gade Malmos, K. et al. ThT 101: a primer on the use of thioflavin T to investigate amyloid formation. *Amyloid* **24**, 1-16 (2017).
221. Biancalana, M. & Koide, S. Molecular mechanism of Thioflavin-T binding to amyloid fibrils. *Biochimica et Biophysica Acta (BBA)-Proteins and Proteomics* **1804**, 1405-1412 (2010).
222. Bondia, P. et al. A nanoscale view of amyloid photodynamic damage. (in preparation)
223. Singh, P.K., Mora, A.K. & Nath, S. Ultrafast fluorescence spectroscopy reveals a dominant weakly-emissive population of fibril bound thioflavin-T. *Chem Commun (Camb)* **51**, 14042-14045 (2015).
224. Freire, S., de Araujo, M.H., Al-Soufi, W. & Novo, M. Photophysical study of Thioflavin T as fluorescence marker of amyloid fibrils. *Dyes and Pigments* **110**, 97-105 (2014).
225. Groenning, M. et al. Binding mode of Thioflavin T in insulin amyloid fibrils. *Journal of Structural Biology* **159**, 483-497 (2007).
226. Kitts, C.C. & Vanden Bout, D.A. Near-field scanning optical microscopy measurements of fluorescent molecular probes binding to insulin amyloid fibrils. *J Phys Chem B* **113**, 12090-12095 (2009).
227. Dalal, V., Bhattacharya, M., Narang, D., Sharma, P.K. & Mukhopadhyay, S. Nanoscale fluorescence imaging of single amyloid fibrils. *The Journal of Physical Chemistry Letters* **3**, 1783-1787 (2012).
228. Peccati, F. et al. Binding of Thioflavin T and Related Probes to Polymorphic Models of Amyloid-beta Fibrils. *J Phys Chem B* **121**, 8926-8934 (2017).
229. Ahn, M. et al. Chemical and mechanistic analysis of photodynamic inhibition of Alzheimer's beta-amyloid aggregation. *Chem Commun (Camb)* **55**, 1152-1155 (2019).
230. Ogilby, P.R. Singlet oxygen: there is indeed something new under the sun. *Chem Soc Rev* **39**, 3181-3209 (2010).
231. Davies, M.J. Singlet oxygen-mediated damage to proteins and its consequences. *Biochemical and Biophysical Research Communications* **305**, 761-770 (2003).
232. Razzokov, J., Yusupov, M. & Bogaerts, A. Oxidation destabilizes toxic amyloid beta peptide aggregation. *Scientific Reports* **9**, 5476 (2019).
233. Davies, M.J. Protein oxidation and peroxidation. *Biochem J* **473**, 805-825 (2016).
234. Adamcik, J. et al. Measurement of intrinsic properties of amyloid fibrils by the peak force QNM method. *Nanoscale* **4**, 4426-4429 (2012).
235. Ruggeri, F.S. et al. Infrared nanospectroscopy characterization of oligomeric and fibrillar aggregates during amyloid formation. *Nature Communications* **6**, 7831 (2015).
236. Ruggeri, F.S. et al. Nanoscale studies link amyloid maturity with polyglutamine diseases onset. *Scientific Reports* **6**, 31155 (2016).

237. Ma, Q., Wei, G. & Yang, X. Influence of Au nanoparticles on the aggregation of amyloid-β-(25–35) peptides. *Nanoscale* **5**, 10397-10403 (2013).
238. Zhong, G. et al. Deterministic, reversible, and nonvolatile low-voltage writing of magnetic domains in epitaxial BaTiO3/Fe3O4 heterostructure. *ACS Nano* **12**, 9558-9567 (2018).
239. Spehar, K. et al. Super-resolution imaging of amyloid structures over extended times by using transient binding of single thioflavin T molecules. *ChemBioChem* **19**, 1944-1948 (2018).
240. Shaban, H.A., Valades-Cruz, C.A., Savatier, J. & Brasselet, S. Polarized super-resolution structural imaging inside amyloid fibrils using Thioflavine T. *Scientific Reports* **7**, 12482 (2017).
241. Lee, G. et al. Mapping the surface charge distribution of amyloid fibril. *Applied Physics Letters* **101**, 043703 (2012).
242. VandenAkker, C.C. et al. Multimodal spectroscopic study of amyloid fibril polymorphism. *The Journal of Physical Chemistry B* **120**, 8809-8817 (2016).
243. Whelan, D.R. & Bell, T.D. Correlative synchrotron fourier transform infrared spectroscopy and single molecule super resolution microscopy for the detection of composition and ultrastructure alterations in single cells. *ACS Chemical Biology* **10**, 2874-2883 (2015).
244. Saka, S.K. et al. Correlated optical and isotopic nanoscopy. *Nature Communications* **5**, 3664 (2014).
245. Vollnhals, F. et al. Correlative microscopy combining secondary ion mass spectrometry and electron microscopy: comparison of intensity–hue–saturation and Laplacian pyramid methods for image fusion. *Analytical Chemistry* **89**, 10702-10710 (2017).
246. Kumar, P. et al. Direct imaging of dopant distributions across the Si-metallization interfaces in solar cells: Correlative nano-analytics by electron microscopy and NanoSIMS. *Solar Energy Materials and Solar Cells* **160**, 398-409 (2017).
247. Ovchinnikova, O.S. et al. Co-registered topographical, band excitation nanomechanical, and mass spectral imaging using a combined atomic force microscopy/mass spectrometry platform. *ACS Nano* **9**, 4260-4269 (2015).
248. Eswara, S. et al. A correlative methodology based on SIMS for advanced materials characterization. *In European Microscopy Congress 2016: Proceedings, (Ed.). Doi:10.1002/9783527808465.EMC2016.6003* (2016).
249. Yang, J., Hatcherian, J., Hackley, P.C. & Pomerantz, A.E. Nanoscale geochemical and geomechanical characterization of organic matter in shale. *Nature Communications* **8**, 2179 (2017).
250. Schmidt, R. et al. The Combination of Electron Microscopy, Raman Microscopy and Energy Dispersive X-Ray Spectroscopy for the Investigation of Polymeric Materials. *Macromolecular symposia* **384**, 1800237 (2019).
251. Hervás, R. et al. Common features at the start of the neurodegeneration cascade. *PLoS Biology* **10**, e1001335 (2012).
252. Fränzl, M. et al. Thermophoretic trap for single amyloid fibril and protein aggregation studies. *Nature Methods* **16**, 611–614 (2019).
253. Michaels, T.C. et al. Chemical kinetics for bridging molecular mechanisms and macroscopic measurements of amyloid fibril formation. *Annual Review of Physical Chemistry* **69**, 273-298 (2018).
254. Meier, B.H., Riek, R. & Böckmann, A. Emerging structural understanding of amyloid fibrils by solid-state NMR. *Trends in Biochemical Sciences* **42**, 777-787 (2017).
255. Kelkar, S.S. & Reineke, T.M. Theranostics: combining imaging and therapy. *Bioconjugate Chemistry* **22**, 1879-1903 (2011).
256. Kim, T.-i. et al. Injectable, cellular-scale optoelectronics with applications for wireless optogenetics. *Science* **340**, 211-216 (2013).

257. Xiang, Y. et al. Physiological amyloid-beta clearance in the periphery and its therapeutic potential for Alzheimer's disease. *Acta Neuropathologica* **130**, 487-499 (2015).
258. Wu, N., Rao, X., Gao, Y., Wang, J. & Xu, F. Amyloid-β deposition and olfactory dysfunction in an Alzheimer's disease model. *Journal of Alzheimer's Disease* **37**, 699-712 (2013).
259. Peelaerts, W. et al. α-Synuclein strains cause distinct synucleinopathies after local and systemic administration. *Nature* **522**, 340 (2015).
260. Wang, J., Gu, B.J., Masters, C.L. & Wang, Y.-J. A systemic view of Alzheimer disease—insights from amyloid-β metabolism beyond the brain. *Nature Reviews Neurology* **13**, 612 (2017).